UNIVERSITY OF THESSALY

SCHOOL OF ENGINEERING

DEPARTMENT OF MECHANICAL ENGINEERING

Finite Element Modeling of Collapse and Buckle Propagation in Deep Subsea Pipelines

by

ARISTEIDIS-GEORGIOS STAMOU

Mechanical Engineer, University of Thessaly, 2019

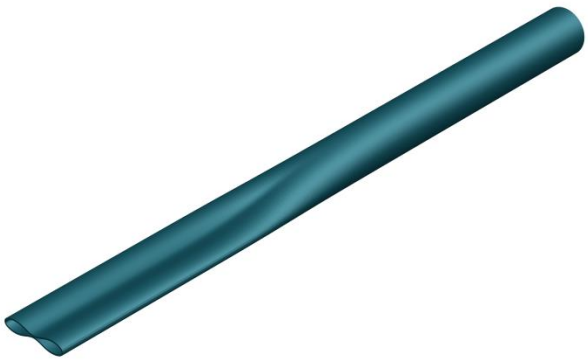

Submitted in partial fulfillment of the requirements for the degree of Master of Science in Mechanical Engineering at the University of Thessaly

Volos, 2021

Approved by the Committee on Final Examination:

Advisor	Dr. Spyros A. Karamanos
	Professor, Department of Mechanical Engineering, University of Thessaly
Member	Dr. Costas Papadimitriou
	Professor, Department of Mechanical Engineering, University of Thessaly
Member	Dr. Nikos Pelekasis
	Professor, Department of Mechanical Engineering, University of Thessaly

Acknowledgements

I wish to express my thanks and appreciation to my supervisor Dr. Spyros A. Karamanos for his guidance and direction during the completion of this thesis and the opportunity to contribute to an interesting field of study. I also acknowledge and thank the other members of the examination committee. I would like to specially thank Konstantinos Antoniou for his help and collaboration. Moreover, i would like to thank my girlfriend Catherine, my friends and my family members for their continuing support and encouragement all these years.

Aristeidis-Georgios Stamou

Finite Element Modeling of Collapse and Buckle Propagation in Deep Subsea Pipelines

ARISTEIDIS-GEORGIOS STAMOU

Department of Mechanical Engineering, University of Thessaly

Supervisor: Spyros A. Karamanos
Professor of Numerical Methods-Finite Element Methods of Structures

Keywords: Collapse, buckle propagation, buckle arrestor, finite elements, imperfections, material anisotropy, residual stresses, elastic-inelastic material.

Abstract- Offshore pipelines are vulnerable to local collapse and buckling propagation upon application of external pressure. Local imperfections, such as ovalization, wall thickness variation around the pipe-wall, material anisotropy, and residual stresses fields are some of the main parameters that reduce the strength of the pipeline under high external pressures. The pipeline may locally collapse due to local imperfections, resulting in the formation of a propagating buckle. The buckle starts to propagate at a high velocity along the pipe length, leaving flattened pipe sections behind. The minimum pressure that allows the buckle to propagate is referred to as "buckle propagation pressure". In this thesis, the collapse responses of different diameter-to-thickness ratio pipe cross-sections with imperfections, upon application of external pressure, are studied numerically using a non-linear finite element simulation. The collapse response is investigated with the two-dimension modeling of rings, which correspond to the pipe cross-sections. Also, the collapse capacity of rings is examined in three dimensions. Furthermore, the influence of initial imperfections, ring geometry, material properties and residual stresses on the collapse pressure, is investigated through parameter analyses. The collapse responses of the rings are examined for elastic and inelastic material cases and the results are compared with analytical solutions. Also, the quasi-static buckle propagation phenomenon under steady state conditions is examined through three-dimensional analyses of pipes with different cross-sectional geometries. The propagation pressure is estimated through the corresponding pressure- volume response. The results are compared with those calculated by analytical equations proposed by publications and standards. In addition, the dependence of the propagation pressure on the element type is examined through parametric analyses. Furthermore, it is demonstrated that the pipe length must be long enough for obtaining steady-state propagation conditions. Moreover, the characteristics of integral buckle arrestor devices are introduced in the end of this thesis. The capability of this device to limit a propagating buckle is studied with the three-dimension finite

element modeling of an integral arrestor device which connects two adjacent pipe sections. A buckle arrestor stiffens the structure locally, and its resistance to collapse rises. Under these circumstances, it is more difficult for the buckle to continue its propagation and thus, it is «arrested» by the device. The pressure of quasi-static crossing of buckle arrestor is referred to as «crossover pressure» and it is associated with the efficiency of the device to arrest the propagating buckle. Also, the dependence of the calculated crossover pressure on the finite element type is examined though parametric analyses.

ΠΡΟΣΟΜΟΙΩΣΗ ΠΕΠΕΡΑΣΜΕΝΩΝ ΣΤΟΙΧΕΙΩΝ ΤΗΣ ΚΑΤΑΡΡΕΥΣΗΣ ΚΑΙ ΤΗΣ ΔΙΑΔΙΔΟΜΕΝΗΣ ΥΒΩΣΗΣ ΣΕ ΥΠΟΘΑΛΑΣΣΙΟΥΣ ΑΓΩΓΟΥΣ

ΑΡΙΣΤΕΙΔΗΣ-ΓΕΩΡΓΙΟΣ ΣΤΑΜΟΥ

Τμήμα Μηχανολόγων Μηχανικών, Πανεπιστήμιο Θεσσαλίας, 2021

Επιβλέπων Καθηγητής: Δρ. Σπυρίδων Α. Καραμάνος
Καθηγητής Υπολογιστικών Μεθόδων-Πεπερασμένων Στοιχείων των Κατασκευών

Λέξεις-κλειδιά: Κατάρρευση, διάδοση ύβωσης, αναστολέας ύβωσης, πεπερασμένα στοιχεία, ατέλειες, ανισοτροπία υλικού, παραμένουσες τάσεις, ελαστικό-ανελαστικό υλικό.

Περίληψη- Οι υποθαλάσσιοι αγωγοί είναι επιρρεπής στην εμφάνιση τοπικού λυγισμού και διαδιδόμενης ύβωσης. Τοπικές ατέλειες όπως η οβαλότητα, η μεταβολή του πάχους κατά τη περιφέρεια του αγωγού, η ανισοτροπία υλικού και τα πεδία παραμενουσών τάσεων, είναι παράγοντες οι οποίοι επηρεάζουν την δομική ευστάθεια των υποθαλάσσιων αγωγών σε περιπτώσεις αυξημένης εξωτερικής πίεσης. Οι τοπικές ατέλειες αποτελούν κάποιους από τους βασικότερους παράγοντες που επιφέρουν τη τοπική αστοχία του αγωγού και τον επακόλουθο σχηματισμό διαδιδόμενης ύβωσης. Η ύβωση διαδίδεται σε υψηλή ταχύτητα κατά μήκος του αγωγού αφήνοντας πεπλατυσμένα τμήματα αγωγού στα μετόπισθεν. Η διάδοση της ύβωσης πραγματοποιείται υπό σταθερή πίεση, η ελάχιστη δυνατή τιμή της οποίας ορίζεται ως η πίεση διάδοσης της ύβωσης. Στη παρούσα εργασία, η εφαρμογή της εξωτερικής πίεσης μελετάται αριθμητικά, διαμέσου προγράμματος πεπερασμένων στοιχείων, σε διατομές αγωγού διαφορετικού λόγου διαμέτρου προς πάχος, οι οποίες φέρουν αρχικές ατέλειες. Η μελέτη για τη μεταβολή της εξωτερικής πίεσης πραγματοποιείται μέσω διδιάστατων αναλύσεων δακτυλίων, οι οποίοι αντιστοιχούν στις διατομές του αγωγού. Επίσης, η αντίσταση των δακτυλίων στη κατάρρευση μελετάται σε τρεις διαστάσεις. Επιπλέον, μελετάται μέσω παραμετρικών αναλύσεων, η επιρροή των αρχικών ατελειών, της γεωμετρίας των δακτυλίων, των ιδιοτήτων υλικού και των παραμενουσών τάσεων στη τιμή της πίεσης κατάρρευσης. Η εφαρμογή της εξωτερικής πίεσης μελετάται για τις περιπτώσεις δακτυλίων ελαστικού και ανελαστικού υλικού και τα αποτελέσματα συγκρίνονται με αναλυτικές λύσεις. Επίσης, το φαινόμενο της οριακά στατικής διάδοσης της ύβωσης υπό την ελάχιστη δυνατή πίεση (πίεση διάδοσης), μελετάται μέσω τριδιάστατων αναλύσεων αγωγών με ίδιο μήκος και διαφορετικές διαστάσεις διατομών. Η πίεση διάδοσης υπολογίζεται μέσω των διαγραμμάτων πίεσης- μεταβολή όγκου. Τα αποτελέσματα συγκρίνονται με τα αντίστοιχα που προκύπτουν από αναλυτικές μεθόδους και από ακριβείς αναλυτικές εξισώσεις που προτείνονται από τη βιβλιογραφία και τους αντίστοιχους κανονισμούς. Επιπρόσθετα, η εξάρτηση της πίεσης διάδοσης από αλλαγές στον τύπο του στοιχείου, εξετάζεται μέσω παραμετρικών

αναλύσεων . Επιπλέον, μέσω παραμετρικών αναλύσεων συμπεραίνεται ότι το μήκος του αγωγού πρέπει να είναι αρκετά μεγάλο έτσι ώστε να επιτευχθούν οι αμετάβλητες συνθήκες πίεσης διάδοσης. Επιπρόσθετα, στο τέλος της παρούσας διπλωματικής εργασίας γίνεται εισαγωγή στα χαρακτηριστικά των integral αναστολέων ύβωσης. Η ικανότητα της συγκεκριμένης συσκευής να περιορίσει μία διαδιδόμενη ύβωση μελετάται μέσω της τριδιάστατης μοντελοποίησης πεπερασμένων στοιχείων, ενός integral αναστολέα ύβωσης ο οποίος συνδέει δύο γειτνιάζοντα τμήματα αγωγού. Ένας αναστολέας ύβωσης τοπικά αυξάνει τη δυσκαμψία της κατασκευής με αποτέλεσμα η αντίσταση της στη κατάρρευση να αυξάνει. Υπό αυτές τις συνθήκες, είναι δύσκολο η ύβωση να συνεχίσει τη διάδοσή της, με αποτέλεσμα να περιορίζεται από τη συσκευή. Η πίεση στην οποία οριακά στατικά διαπερνά η ύβωση τον αναστολέα ύβωσης αναφέρεται ως "πίεση ανάσχεσης" και συνδέεται με την αποδοτικότητα αυτής της συσκευής να περιορίσει τη διαδιδόμενη ύβωση. Ακόμα, η εξάρτηση της υπολογιζόμενης πίεσης ανάσχεσης από τον τύπο του πεπερασμένου στοιχείου, μελετάται μέσω παραμετρικών αναλύσεων.

Table of Contents

List of Figures

List of Tables

Chapter 1 – Introduction

1.1 Introduction

The progression in pipeline technology makes feasible the installation and safe operation of long pipelines in onshore and offshore regions. Therefore, pipelines constitute one of the basic methods for transportation of hydrocarbons. Pipelines are expensive projects due to their high costs of manufacturing. However, the maintenance costs of these projects are low, and their life expectancy is up to 40 years. One example of an offshore pipeline project is the Blue Stream pipeline, which connects Russia and Turkey through the Black Sea. The pipeline has a length of 430 km and is established at a sea depth of 2150 m. This project was completed in 2003 and it was considered as the deepest subsea pipeline at time of construction. Another deepwater pipeline project is the Medgaz pipeline between Algeria and Spain. The subsea pipeline is established at depths of 2150 km and the pipeline started to operate in 2009. Other examples of offshore pipeline projects are the Green Stream pipeline (2004) between Libya and Sicily and the Nord Stream pipeline between Russia and Germany (2011). These are some typical examples of pipeline projects which are currently operating.

Many challenges are posed during the design stage of offshore pipelines. More specifically, the pipeline must be capable to sustain the applied loads during installation and must be able to operate safely under external and internal pressure loading. The ambient external pressure rises proportionally with the sea depth and thus it poses a significant challenge for the offshore pipeline design. Also, the high temperature and pressure of the flowing hydrocarbon must be considered during offshore pipeline design [1]. The installation methods of subsea pipelines pose major challenges for the design of offshore pipelines. During installation the pipeline is empty, and the basic methods of pipeline installations are the **S-lay method**, the **J-lay method**, the **Reeling method** and the **Tow methods**. The S-lay and J-lay methods are schematically represented in **Fig. 1.1** and **Fig. 1.2** respectively. As it can be seen from both figures, a combination of loads is applied on the empty pipeline. At stinger, a combination of bending and tension intensities are applied (**Fig. 1.1**), whereas at the "sagbend" region a combined loading of external pressure, bending and tension exists (**Fig. 1.1**, **Fig. 1.2**). The combined loading conditions at the "sagbend" region close to the seafloor, may lead to local buckling of the pipeline. This local buckling reduces the pipeline stiffness and results in the local collapse of the pipeline region. This configuration is in the form of a "dogbone" shape due to the contact between two opposite regions of the most deformed interior surface of the pipeline. While the deformation proceeds, the contact is further stabilized, and the local region takes a flatten shape. This local damage can initiate further instabilities, which under the appropriate conditions will "propagate" along the

pipeline length resulting in further flattening of the pipeline. The propagation of instabilities along the pipe length is referred to as «buckle propagation phenomenon». This propagation performs under a low pressure, which is known as the «propagation pressure» and the propagation pattern refers to the global flattening of the pipeline. **Fig. 1.3** depicts the numerical simulation of the formation and the subsequent propagation of a local collapse, at a region of a steel pipeline. This local instability will start to propagate in two directions along the pipeline length under the propagation pressure and the catastrophic consequences are presented in **Fig. 1.4**. Unless an obstacle or a field of higher pressure is reached, buckle propagation will be continued, and more pipeline sections will be destroyed. The propagation pressure is approximately 15-25% of the pipe's collapse pressure [1].

The buckling propagation phenomenon is aborted by using buckle arrestors. These devices are welded between two adjacent pipe sections, and they are periodically installed along the line to limit the propagation of collapse. **Fig. 1.5** shows a length of a pipeline section, where two integral buckle arrestors are installed. In the same figure, the initiation of collapse and its propagation in two opposite directions along the pipeline is shown as well. The damage induced by the propagating buckle along the line will be limited in the presence of buckle arrestor devices. When the buckle approaches the arrestor, the buckle propagation phenomenon diminishes, because a higher pressure than the propagation pressure is needed for the buckle to pass over the device. While the buckle is «crossing» the arrestor, the pressure starts rising until a maximum pressure value, which is defined as the «crossover pressure». The magnitude of crossover pressure shows the capability of the arrestor device to stop the damaging effects of buckle propagation. Buckles cross the arrestors at different deformation modes, which are dependent on the geometric characteristics of the device. Arrestor devices of high efficiency, exhibit a mode of deformation which is flipped by 90°. This reversed ovalization configuration is called the «flipping mode of crossover», and a characteristic example of that mode of deformation is shown in **Fig. 1.6**.

The above loading conditions should be considered during the offshore pipeline design. The modern design concept for the safe mechanical behavior of subsea pipelines, is based on the limit state design criteria. The considered limit states for an offshore pipeline are many. Two typical examples of limit states are the design against buckling under external pressure and the design against burst under internal pressure. Therefore, many standards have been developed for all possible failure modes. The standards of API R. P. 1111 [2] and DNVGL-ST-F101 [3] will be used in this thesis. In the following section, the analysis of the mechanical response of a long cylindrical shell under external pressure will be presented in the form of buckling theory [1], [4]-[6].

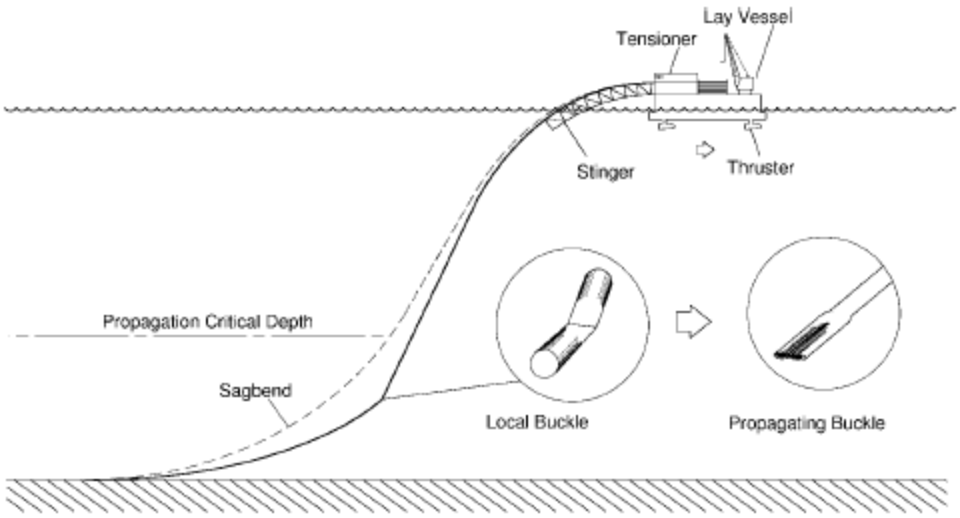

Fig. 1.1 Schematic representation of the "S-lay" pipeline installation method (Source:[1]).

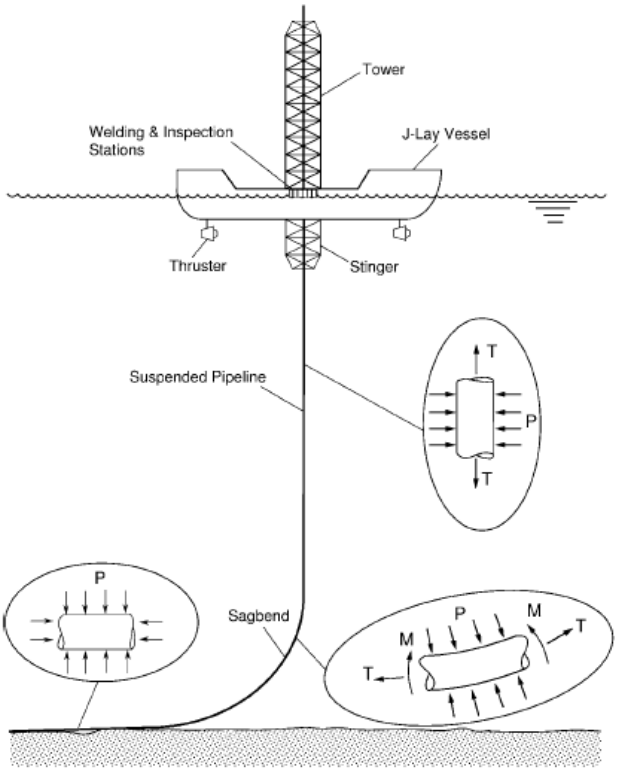

Fig. 1.2 Schematic representation of the "J-lay" pipeline installation method and the corresponding installation loads (Source:[1]).

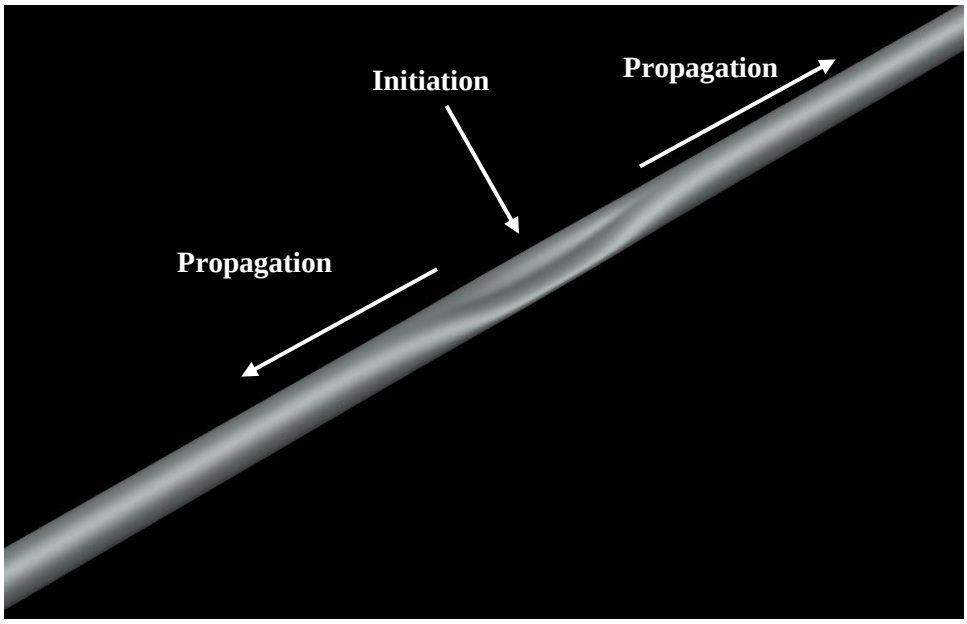

Fig. 1.3 Numerical simulation of the formation and propagation of local instabilities at a pipeline section.

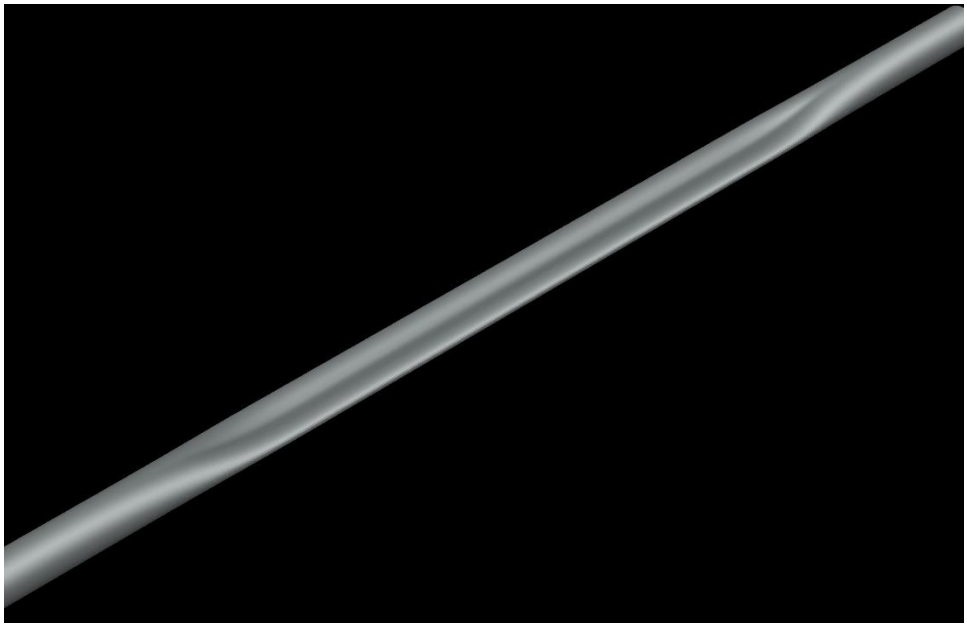

Fig. 1.4 Numerical simulation of buckle propagation phenomenon along the pipeline.

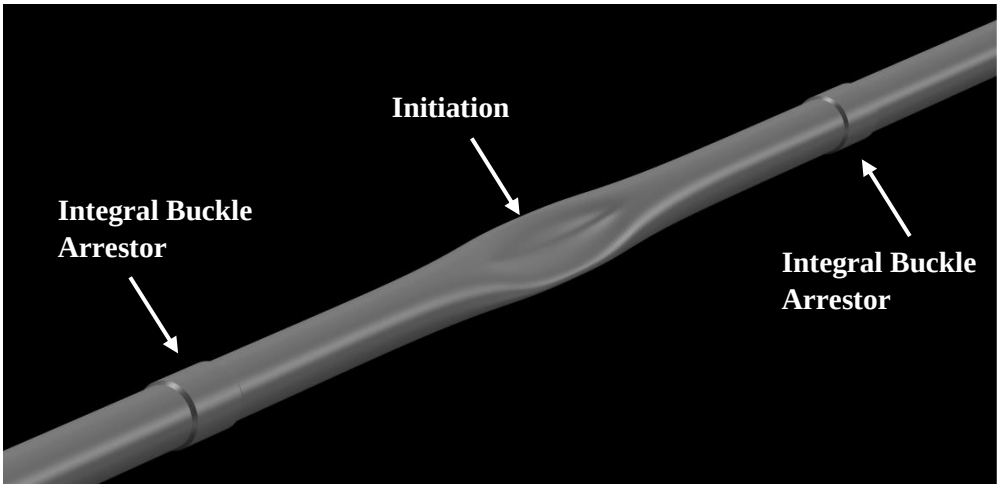

Fig. 1.5 Numerical simulation of the initiation of a local buckle in a pipeline section which is surrounded by integral buckle arrestors.

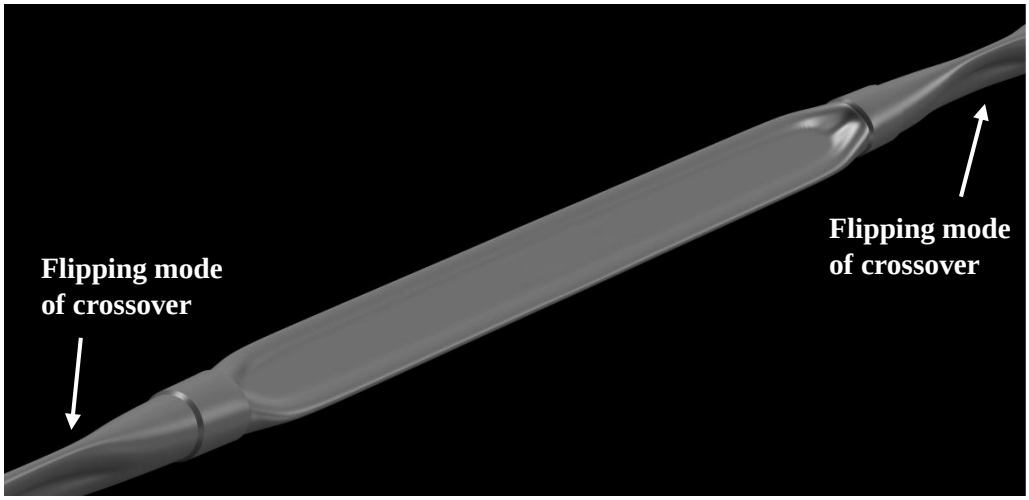

Fig. 1.6 Numerical simulation of the flipping mode of crossover for the installed arrestors along the line.

1.2 Buckling of Elastic Rings

The elastic buckling of thin rings will be analyzed in this section. This two-dimensional problem is a simplified consideration of long cylindrical shell with perfect geometry, which is subjected to uniform external pressure. A rectangular ring wall cross-section of a long cylinder is assumed. For the determination of the kinematic relations that describe the cross-sectional deformation, an arbitrary point «A» of the cross-section is considered at the mean circumference or «Reference Line», as shown in **Fig. 1.7** [1], [4], [5], [7]. The ring cross-section of mean radius R_m and thickness t is shown in the same figure. It is assumed that the cross-section follows a **Bernoulli-type in-plane deformation**, which means that the plane sections remain **plane** and **normal** to the deformed mean line after deformation. The position of point A of the small cross-sectional element can be seen before and after deformation, where it is denoted as «A′». The notations w(θ) and υ(θ) denote the components of the displacement vector in radial and tangential direction respectively. The position of point A before (x, y) and after deformation (x^*, y^*) are derived from **Fig. 1.7** as follows

$$x = r\cos(\theta) \tag{1.1}$$

$$y = r\sin(\theta) \tag{1.2}$$

$$x^* = (R_m + w)\cos(\theta) - \upsilon\sin(\theta) \tag{1.3}$$

$$y^* = (R_m + w)\sin(\theta) + \upsilon\cos(\theta) \tag{1.4}$$

The kinematic relations for the thin circular ring have been postulated from the kinematic analysis of **Fig. 1.7**. By using the notation $(*)' = {d(*)}/{d\theta}$ to describe the derivative of a variable, the circumferential strain of the deformed cross section is postulated as follows [1], [4], [5], [7]

$$\varepsilon = \varepsilon_o + zk \tag{1.5}$$

where

$$\varepsilon_o = \left(\frac{\upsilon' + w}{R_m}\right) + \frac{1}{2}\left(\frac{\upsilon - w'}{R_m}\right)^2 \tag{1.6}$$

and

$$k = \frac{\upsilon' - w''}{{R_m}^2} \tag{1.7}$$

The first term of (1.6) is the axial strain, ε, in the tangential direction and is presented by the following form

$$\varepsilon_a = \frac{\upsilon' + w}{R_m} \tag{1.8}$$

Equation (1.7) expresses the curvature change of the examined reference line element. The cross-sectional rotation β, which is shown in **Fig. 1.7**, is expressed as

$$\beta = \frac{\upsilon - w'}{R_m}$$

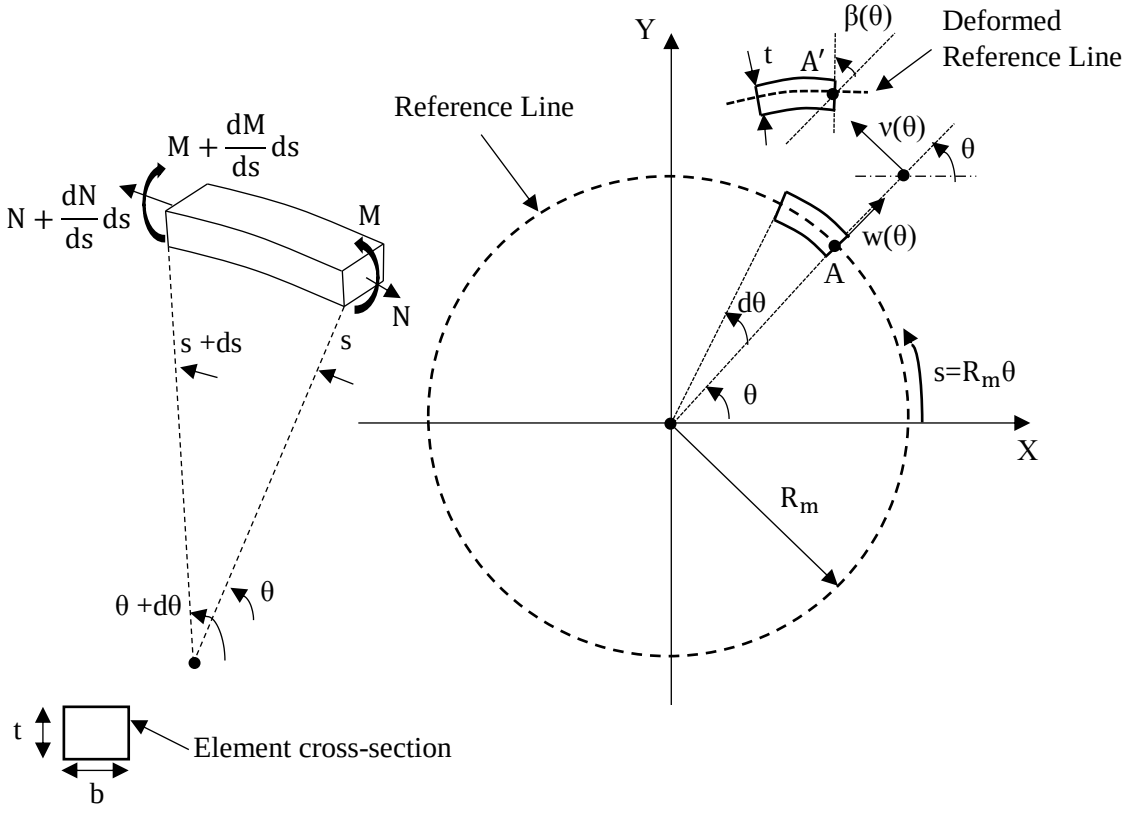

Fig. 1.7 Cross-sectional elements of the ring mean circumference before and after deformation. The force and moment intensities acting on the circumferential element are shown on the left side [4].

The force N and moment M intensities are acting on the small element of reference line, as shown in **Fig. 1.7**. These intensities can be obtained by integrating over the element cross-section of area $A = b\,t$. The resulting formulas are presented below

$$N = E^* A\,\varepsilon_o$$

$$M = E^* I\,k$$

where $I = {bt^3}/{12}$ and, $E^* = {E}/{(1-\nu^2)}$ is the elastic modulus under plain strain conditions.

The potential energy will be used to derive the ring equilibrium equations. The potential energy Π is the sum of strain energy U and potential energy V of external loads acting on the element. The strain energy is calculated as

$$U = \frac{1}{2}\int_0^{2\pi} (N\varepsilon_o + Mk)R_m d\theta = \frac{E^* A R_m}{2}\int_0^{2\pi} {\varepsilon_o}^2 d\theta + \frac{E^* I R_m}{2}\int_0^{2\pi} k^2 d\theta \tag{1.9}$$

The load in this case is the external pressure P and it has been proved that the potential energy of this load type is $V = -P\,\Delta A$, where ΔA is the reduction of the enclosed area. The initial area is $A_o = \pi {R_m}^2$ and the deformed area A^* can be calculated as follows [4]

$$A^* = \int_{A^*} dA^* = \frac{1}{2}\int_0^{2\pi} \left(\frac{dx^*}{dx^*} + \frac{dy^*}{dy^*}\right) dA^* = \frac{1}{2}\int_0^{2\pi} \mathrm{div}\mathbf{x}^* dA^*$$

The substitution of (1.3) and (1.4) to the last equation results in

$$A^* = \frac{1}{2}\int_0^{2\pi} (2R_m w + \upsilon^2 - \upsilon w' + \upsilon' w + w^2)d\theta + \pi {R_m}^2$$

Given that $\Delta A = A_o - A^*$, the reduction of the enclosed area is

$$\Delta A = \frac{1}{2}\int_0^{2\pi} (2R_m w + \upsilon^2 - \upsilon w' + \upsilon' w + w^2)d\theta$$

Given that W= -V, it follows

$$W = \frac{P}{2}\int_0^{2\pi}(2R_m w + \upsilon^2 - \upsilon w' + \upsilon' w + w^2)d\theta \tag{1.10}$$

The sum of (1.9) and (1.10) gives the potential energy as shown below

$$\Pi = R_m\int_0^{2\pi}\left(\frac{E^*(A\,\varepsilon_o{}^2 + I\,k^2)}{2} + P\left(w + \frac{1}{2R_m}(\upsilon^2 - \upsilon w' + \upsilon' w + w^2)\right)\right)d\theta \tag{1.11}$$

For the enforcement of equilibrium, the stationary value of Π is sought, and using variational calculus the final equations of equilibrium are derived [1], [4], [5], [7]

$$\begin{gathered} R_m\,N' + M' - RN\beta - PR_m{}^2\beta = 0 \\ M'' - R_m N - R_m(N\beta)' - PR_m(\upsilon' + w) = PR_m{}^2 \end{gathered} \tag{1.12}$$

The pre-buckling solution is $N_o = -PR_m$ and it follows that $\varepsilon_o{}^0 = {}^{w_o}/_{R_m}$. Also, the following expressions are derived

$$N_o = E^* A\frac{w_o}{R_m}$$

$$w_o = -\frac{PR_m{}^2}{E^*\,t}$$

$$\upsilon_o = 0$$

The components of displacement w_o, υ_o of the circular configuration, refer to the pre-buckling stage. When bifurcation buckling occurs, the ring will take a slightly non-circular shape and the equations of this stage are derived by perturbing the displacements of the pre-buckling stage as follows [1], [4], [5]

$$w \to w_o + w_1$$

$$\upsilon \to \upsilon_o + \upsilon_1$$

Substituting the perturbating relations into (1.12) and neglecting terms that are of order higher than two in w_1 and υ_1 , results in the equations for loss of stability as follows [1], [4], [5]

$$E^* A R_m{}^2 (\upsilon_1' + w_1)' + E^* I (\upsilon_1 - w_1')'' = 0$$

$$E^* A R_m{}^2 (\upsilon_1' + w_1) - E^* I (\upsilon_1 - w_1')''' + P R_m{}^3 (w_1'' + w_1) = 0 \quad (1.13)$$

A solution of the following form satisfies (1.13)

$$\begin{matrix} \upsilon_1 = C_1 \sin(n\theta) \\ w_1 = C_2 \cos(n\theta) \end{matrix} \quad , n = 1,2,3 \ldots \quad (1.14)$$

Substituting (1.14) into (1.13) results in the following linear system

$$\begin{pmatrix} n^2(1+a) & n\,(1+an^2) \\ n\,(1+an^2) & (1+an^4) - (n^2-1)\,\gamma \end{pmatrix} \begin{pmatrix} C_1 \\ C_2 \end{pmatrix} = 0$$

where $a = I/AR_m{}^2$ and $\gamma = P\,R_m/E^*A$.

For nontrivial solution, $C_1, C_2 \neq 0$ and the determinant of matrix must be zero and it follows

$$\begin{pmatrix} n^2(1+a) & n\,(1+an^2) \\ n\,(1+an^2) & (1+an^4) - (n^2-1)\,\gamma \end{pmatrix} = 0$$

After some algebraic steps the following sequence of eigenvalues are derived

$$P_n = \frac{2\,E^*\,(n^2-1)}{3\,(1+a)} \left(\frac{t}{D_m}\right)^3 \quad n = 2,3 \ldots \quad (1.15)$$

where $D_m = 2R_m$.

The term "a" is much smaller than unity ($a \ll 1$) for high D_m/t ratios (e.g., $D_m/t \geq 30$), and thus $1 + a \cong 1$. Minimum pressure is obtained for n=2 and the corresponding eigenvalue is the critical elastic or "elastic buckling" pressure of the ring under plain strain conditions [1], [4]-[6] (Bryan (1980))

$$P_{cr} = \frac{2\,E}{(1-\nu^2)}\left(\frac{t}{D_m}\right)^3 \tag{1.16}$$

The solution for the vector displacements is

$$w_1 = \omega\cos(2\theta)$$
$$\upsilon_1 = -\frac{\omega}{2}\sin(2\theta) \tag{1.17}$$

where $\omega = C_2 = -2C_1$

It can be seen from (1.16) that an important influencing parameter of the buckling pressure formula is the diameter-thickness-ratio (DTR or D/t). The present analysis has been proceeded in terms of the mean diameter.

Up to this point, the collapse pressure is derived for a long pipe of elastic material and in the absence of any imperfections. In deep water applications, the metal pipelines are thick walled with a D/t less than 25 [8] and it was concluded [9], [10] that these tubular structures collapse at pressure value close to the yield pressure which is given as follows

$$P_y = 2\sigma_y\,\frac{t}{D_m} \tag{1.18}$$

Therefore, the ring collapse occurs in the plastic range of the material and this mode is referred to as «plastic buckling». The basic condition for elastic buckling of a metal ring with no imperfections is given below

$$P_{cr} \le P_y$$
$$\Rightarrow \frac{2\,E}{(1-\nu^2)}\left(\frac{t}{D_m}\right)^3 \le 2\sigma_y\,\frac{t}{D_m}$$
$$\Rightarrow \frac{D_m}{t} \ge \sqrt{\frac{E}{(1-\nu^2)\sigma_y}} \tag{1.19}$$

The result of (1.19) defines the critical D/t that separates the elastic and plastic buckling mode of a perfect metal ring. Murphey *et al.* [10] recognized that an estimation of the collapse pressure, P_{co}, of a metal ring without any imperfections, can be given as follows

$$P_{co} = \frac{P_{cr} P_y}{\sqrt{(P_{cr}{}^2 + P_y{}^2)}} \tag{1.20}$$

In the following sections, the pre-buckling and post-buckling behavior of elastic-plastic and elastic rings will be examined.

1.3 Imperfect Elastic Rings

An imperfect elastic ring is considered with an initial imperfection (w_0, υ_0) defined by the buckling mode of (1.17)

$$\begin{aligned} w_0 &= \omega \cos(2\theta) \\ \upsilon_0 &= -\frac{\omega}{2} \sin(2\theta) \end{aligned} \tag{1.21}$$

This type of initial imperfection corresponds to an initial oval shape of amplitude ω (**Fig. 1.8**). Upon application of external pressure, it is expected that the initial oval shape will increase its amplitude. It can be shown (the proof is omitted) that the deformation of an initially imperfect elastic ring is expressed in terms of radial and tangential deformation as follows [4]

$$w(\theta) = \omega \left(\frac{1}{1 - P/P_{cr}} \right) \cos(2\theta) \tag{1.22}$$

$$\upsilon\,(\theta) = -\frac{\omega}{2} \left(\frac{1}{1 - P/P_{cr}} \right) \sin(2\theta) \tag{1.23}$$

The stress acting on the pipe wall is equal to

$$\sigma(\theta) = \frac{N_\Theta}{t} + \left(\frac{M(\theta)}{t^2/12}\right)\frac{t}{2} \tag{1.24}$$

where

$$M(\theta) = \frac{3E^* I}{{R_m}^2}\left(\frac{\omega}{1 - P/P_{cr}}\right)\cos(2\theta) \tag{1.25}$$

The last equation (1.25) shows that the maximum bending stresses will occur at four equally-spaced locations at the circumference of the ring ($\theta = 0,\ \pi/2\ , \pi,\ 3\pi/2$), which are denoted as A, B, C, D in **Fig. 1.8.** Therefore, the maximum stress acting at those points is

$$\sigma_{max} = \frac{-PR_m}{t} \pm \left(\frac{PR_m\omega}{1 - P/P_{cr}}\right)\frac{1}{(t^2/6)} \tag{1.26}$$

The first term in (1.26) is referred to the membrane stress (σ_m) and the second term is referred to the bending stress. First yielding occurs when the sum of these stresses equals the yield stress σ_y. The pressure of first yielding is denoted as P_f, and it can be calculated by the following equation [11]

$${P_f}^2 - \left(\frac{\sigma_y t}{R_m} + \left(1 + \frac{6R_m}{t}\left(\frac{\omega}{R_m}\right)\right)P_{cr}\right)P_f + \frac{\sigma_y t}{R_m}P_{cr} = 0 \tag{1.27}$$

The equation for the calculation of first yielding pressure is attributed to Timoshenko [11]. The last equation is expressed in terms of yield pressure P_y and P_{cr} as follows

$${P_f}^2 - \left(P_y + \zeta P_{cr}\right)P_f + P_y P_{cr} = 0 \tag{1.28}$$

where $\zeta = 1 + {}^{6R_m}/_{t}\left({}^{\omega}/_{R_m}\right)$

The solution of (1.28) is [1]

$$P_f = \frac{1}{2}\left(\left(P_y + \zeta P_{cr}\right) - \left[\left(P_y + \zeta P_{cr}\right)^2 - 4P_y P_{cr}\right]^{1/2}\right) \tag{1.29}$$

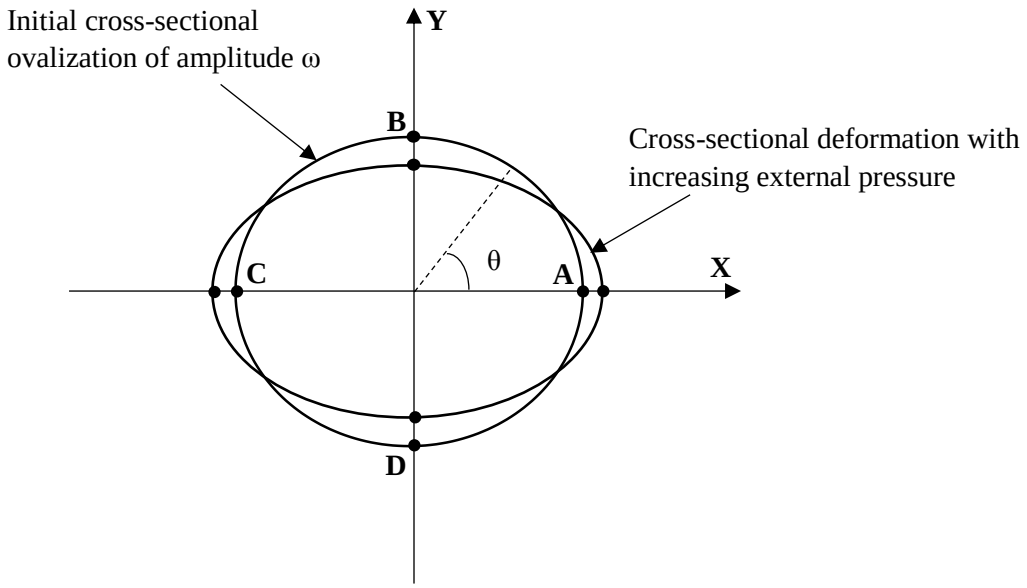

Fig. 1.8 The figure represents the cross-sectional deformation of an initially ovalized ring and the locations of maximum stress at four equally-spaced points (A, B, C, D) around the circumference.

1.4 Pre-buckling and Post-Buckling Behavior of Perfect Elastic Rings

The pre-buckling solution that satisfies the equations of equilibrium (1.12) is derived in section 1.2, and it follows that the absolute value of the membrane stress in the circumferential direction of the ring is equal to

$$|\sigma_m{}^0| = \frac{PR_m}{t} \tag{1.30}$$

From the pre-buckling solution it has been shown that the ring's deflection is uniform around the circumference $w_o(\theta) = w_o$, and thus it follows

$$\varepsilon_o{}^0 = \frac{|w_o|}{R_m} \tag{1.31}$$

where

$$|w_o| = \frac{P R_m{}^2 (1-\nu^2)}{E\,t} \tag{1.32}$$

The analysis will be focused on a quadrant of the ring due to symmetries imposed by the ring's circular shape. The area change between the undeformed and deformed configurations of the quadrant can be expressed by the following form

$$\Delta A = \frac{1}{2}\pi R_m |w_o| \tag{1.33}$$

The application of Hooke's law under plane strain conditions at the pre-buckling stage ($|\sigma_m{}^0|, \varepsilon_o{}^0$) is given by

$$|\sigma_m{}^0| = \frac{E}{1-\nu^2}\,\varepsilon_o{}^0 \tag{1.34}$$

Combining (1.31) and (1.33) results in the following expression

$$\varepsilon_o{}^0 = \frac{2\Delta A}{\pi R_m{}^2} \tag{1.35}$$

The substitution of (1.35) and (1.30) to (1.34), gives the relation of pressure P with ΔA during the pre-buckling response

$$P = \left(\frac{2Et}{(1-\nu^2)\pi R_m{}^3}\right)\Delta A \tag{1.36}$$

The critical elastic pressure of such a ring is derived in section 1.2. The initial post-buckling response of perfectly elastic rings was studied by Budiansky [12], and the analytical equations are presented below

$$P = P_{cr}\left(1 + \frac{27}{32}\,\Delta^2\right) \tag{1.37}$$

$$P = P_{cr}\left(1 + \frac{9}{16A_o}\,\Delta A\right) \tag{1.38}$$

where A_o is the initial area enclosed by the unloaded stress-free ring, and Δ is the ovality parameter which will be explained further in the following chapter. When the pressure attains P_{cr}, the ring buckles elastically. The deformed area at the buckling stage, ΔA_{cr}, is calculated from (1.36) as follows

$$\Delta A_{cr} = \frac{P_{cr}\,(1-\nu^2)\,\pi\,{R_m}^3}{2Et} \tag{1.39}$$

1.5 Plastic collapse mechanism

A ring of mean radius R_m and thickness t with elastic-plastic material is considered. The simplest kinematic model to describe the plastic deformation of that ring under external pressure loading, was first proposed by Palmer and Martin [13]. The model consists of four equally spaced plastic hinges which they are connected by four segments and thus the model has a rhombus shape (**Fig. 1.9**). A quarter of the quadrilateral's undeformed and deformed configurations, as well as the geometric relationships, are represented on the right side of **Fig. 1.9**. Let "x" and "η" define the normalized induced deflections in Y and X directions respectively. The enclosed area of the deformed quadrilateral can be expressed as a function of x. Using the geometric relationships for the triangle in the deformed configuration , the area enclosed is expressed as follows [4]

$$A^* = \frac{{R_m}^2(1-x)\sqrt{1+2x-x^2}}{2}$$

Therefore, the change in area between the two configurations is

$$\Delta A = \frac{{R_m}^2 - {R_m}^2(1-x)\sqrt{1+2x-x^2}}{2} \tag{1.40}$$

The equilibrium analysis of the deformed configuration will give the pressure- deflection relation in the post-buckling region. The equilibrium path of plastic collapse mechanism was derived in [4] and the resulting formula is [14]

$$P = 2\,\sigma_y{}^{*}\left(\frac{t}{D_m}\right)^2 \frac{1}{2x - x^2} \tag{1.41}$$

where D_m is the ring's mean diameter and $\sigma_y{}^{*}$is the yield stress under plane-strain conditions, which can be taken as $\sigma_y{}^{*} = 1.125\,\sigma_y$.

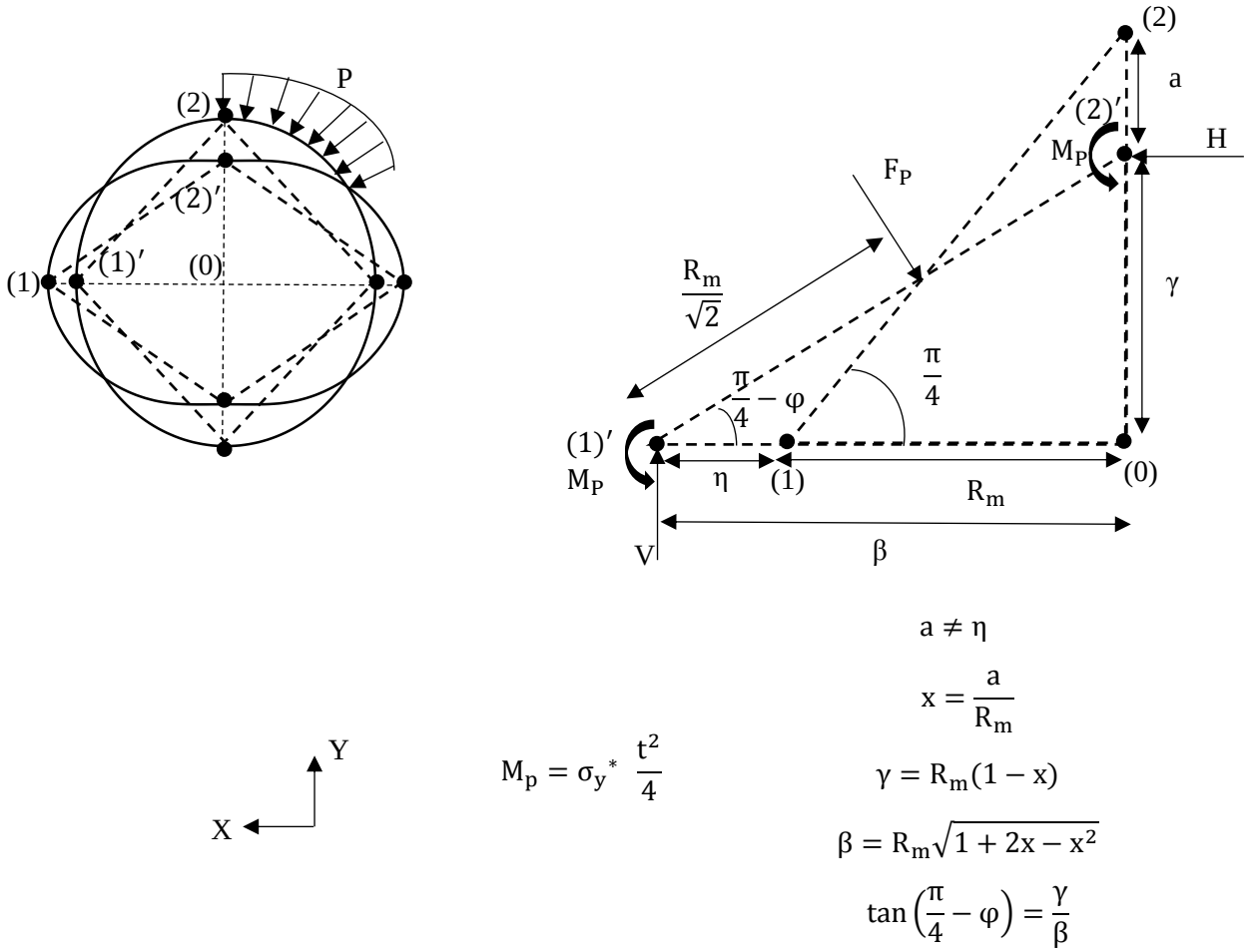

Fig. 1.9 Plastic hinge model with geometric relationships for the analysis of cross-sectional deformation [14].

1.6 Thesis Organization

The present thesis is divided into five chapters. **Chapter 1** presents shortly the ring buckling theory, and the terms of elastic and plastic buckling are properly defined. Also, analytical equations that describe the pre-buckling and post-buckling behavior of elastic-inelastic rings are included in this chapter. **Chapter 2** presents detailed model studies of the collapse of rings in two dimensions. The mechanical behavior of rings upon application of uniform external pressure is examined also by three-dimensional finite element model analyses. The effects of initial imperfections on the collapse pressure, are studied through parametric studies for rings of elastic and inelastic material. Also, the propagation pressure is calculated through two-dimensional analytical methods. **Chapter 3** presents the three-dimensional analysis of buckle propagation phenomenon. The propagation pressure is estimated from the pressure-change in volume responses for different pipe geometries. Furthermore, the main parameters that influence the propagation pressure are studied through parameter analyses. **Chapter 4** studies the performance of an integral buckle arrestor by three-dimension finite element model analysis. Furthermore, the arrestor's capability to limit a propagating buckle is studied through parametric analyses. Finally in **Chapter 5**, a summary of the most important conclusions drawn in this work are presented.

Chapter 2 - Ring Analysis of Collapse and Buckle Propagation Under External Pressure

2.1 Introduction

External pressure is one of the most important load parameters that affects the mechanical behavior of subsea pipelines because they collapse if the external pressure is larger than a critical pressure value (Chapter 1). If collapse conditions are satisfied in a segment of an offshore pipeline, a local buckle is formed which results in flattening of the pipe's section. Soon after the formation and the collapse of the local section, buckle starts to propagate at a high velocity along the pipe's length, leaving flattened pipe sections behind. The buckle propagates under a constant pressure, the «buckle propagation pressure» (Chapter 1). Unless an obstacle, like a buckle arrestor is reached, buckle propagation will be continued, and more pipeline sections will be destroyed.

This chapter deals primally with the two-dimensional analysis of collapse of a tube under external pressure and the related problem of buckle propagation is examined as well. A pipeline, which is established at the bottom of the ocean, undergoes external pressure loading and as a result the problem is a three-dimensional (3D) one. However, under plane strain conditions the same problem is considered as a two-dimensional (2D) one and thus only a cross-section of the tube is considered for analysis. More specifically, the formulation of the two-dimensional analysis is based on a «ring» of external diameter D and thickness t, where pressure is acting on the ring external circumference and it is assumed to be always normal to the surface. Furthermore, the mechanical responses of rings are examined in three dimensions as well.

Previous studies [9], [15]-[19] have shown that the collapse response of a pipe is affected by many factors such as **geometric imperfections**, **material properties**, **material anisotropy** and **residual stresses**, which are induced by manufacturing process. In the current thesis special emphasis will be given on the effect of initial geometric imperfections, such as **initial ovality** and **wall thickness variation** around the circumference of a ring, on the collapse pressure. Also, the influence of **material anisotropy** and **residual stresses fields** on the collapse capacity of a pipe will be examined in the current thesis. The effects of these factors on the structural integrity of a pipe, are analyzed numerically by creating finite element models of two-dimensional and three-dimensional rings in the general-purpose Finite Element program ABAQUS standard. The effects of these factors on the collapse pressure of rings are also examined in previous theses [20], [21].

2.2 Initial Imperfections

A description of the initial imperfections in the forms of ovality and wall thickness variation will be given in this section. Ovality as an initial imperfection of a ring, describes the magnitude of deviation from the prefect circular shape. Initial ovality is expressed by the following form (Section 1.2, equation (1.17)) [15]

$$w_o(\theta) = \omega \cos(2\theta) \tag{2.1}$$

where ω is the amplitude of initial oval shape as shown in **Fig. 2.1**.

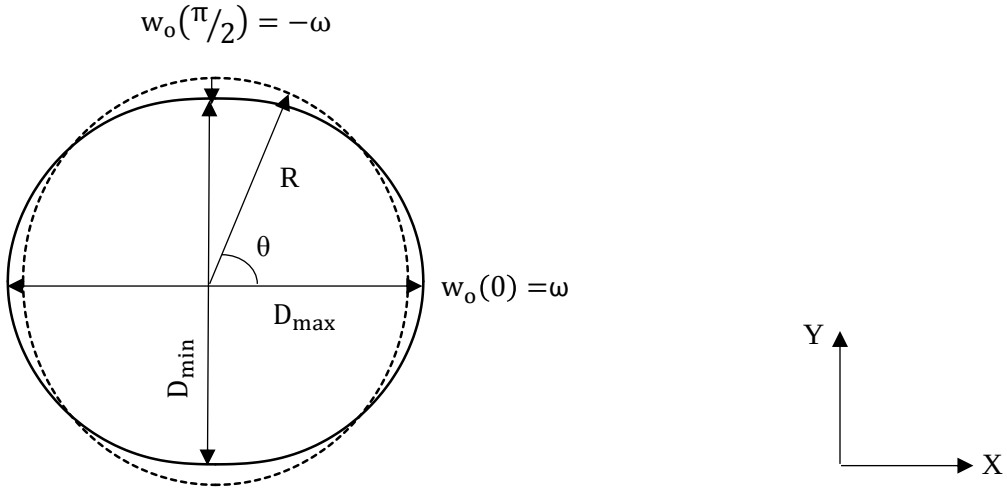

Fig. 2.1 Initially ovalized ring by a uniform radial displacement $w_o(\theta)$.

The desired initial ovality value, Δ_o , that will be implemented into the finite element models is calculated by the following form [1], [22]

$$\Delta_o = \frac{D_{max} - D_{min}}{D_{max} + D_{min}} \tag{2.2}$$

where D_{max} and D_{min} represent the maximum and minimum values of the ring's outer diameters.

The initially ovalized shape of the cross-section of the ring can be written in a more general form by means of the external diameter of ellipse D_θ at all polar angles as follows

$$D_\theta = D + 2\omega\cos(2\theta) \tag{2.3}$$

Apparently, $D_{max} = D + 2\omega$ and $D_{min} = D - 2\omega$ and substituting these two expressions to (2.2) results in the following expression

$$\Delta_o = \frac{\omega}{R} \tag{2.4}$$

where R is the external radius of the ring.

The variation of wall thickness around the circumference for a circular ring can be expressed by the following expression [9], [22]

$$\frac{t_\theta}{t} = 1 - \frac{\eta}{t}\sin(\theta) \tag{2.5}$$

where t_θ is the thickness in radial direction and η is the magnitude of eccentricity between the outer and the inner circles in Y direction (**Fig. 2.2**). Maximum and minimum values of thickness exist for angles $\theta = \frac{3\pi}{2}$ and $\theta = \frac{\pi}{2}$ respectively, and from (2.5) it follows that

$$t_{max} = t + \eta \tag{2.6}$$

$$t_{min} = t - \eta$$

The desired initial eccentricity Ξ_o that will be implemented into the finite element models, is calculated by use of the following expression [9], [22]

$$\Xi_o = \frac{t_{max} - t_{min}}{t_{max} + t_{min}} \tag{2.7}$$

Substituting (2.6) to (2.7) results in the following expression

$$\Xi_o = \frac{\eta}{t} \tag{2.8}$$

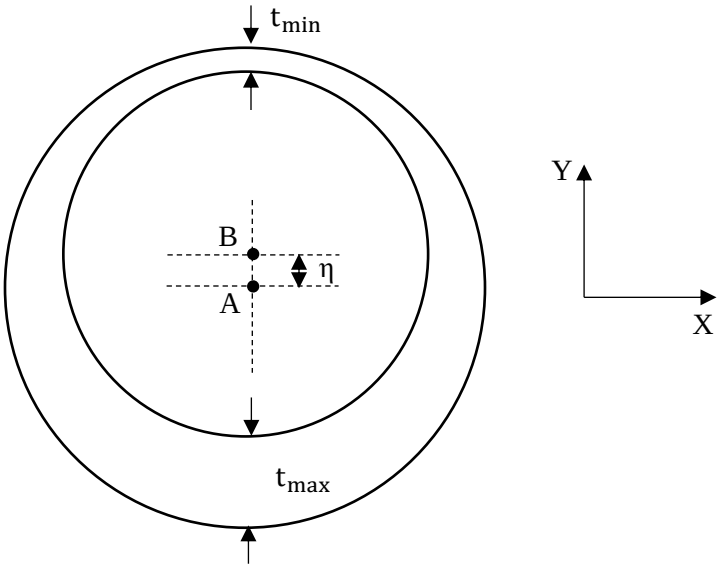

Fig. 2.2 Wall thickness variation of the ring in the form of thickness eccentricity in Y direction.

2.3 Numerical Modeling

The numerical framework of ABAQUS standard is used, for the development of finite element two-dimensional ring models with initial imperfections in the forms of ovality and wall thickness variation. The numerical analyses will be divided in two cases. In the first case, initial imperfections will be in the form of ovality and thus only a quarter of the ring is needed for analysis due to the symmetries of (2.3). The second case involves initial imperfections of both ovality and wall thickness variation. Therefore, a half of the ring is needed to be modeled in this case. The need of half ring analysis in this case, arises from the symmetries of equations (2.3), (2.5).

The material properties of steel grade X65 are used to examine the elastic-plastic behavior of the models. The material is characterized by elastic modulus E=210 GPa, poisson ratio ν=0.3 and yield stress $\sigma_y = 449.40$ MPa. The material nominal stress-strain response (**Fig. 2.3**) is produced from data pairs [20], [21] which are listed in **Table 2.1**.

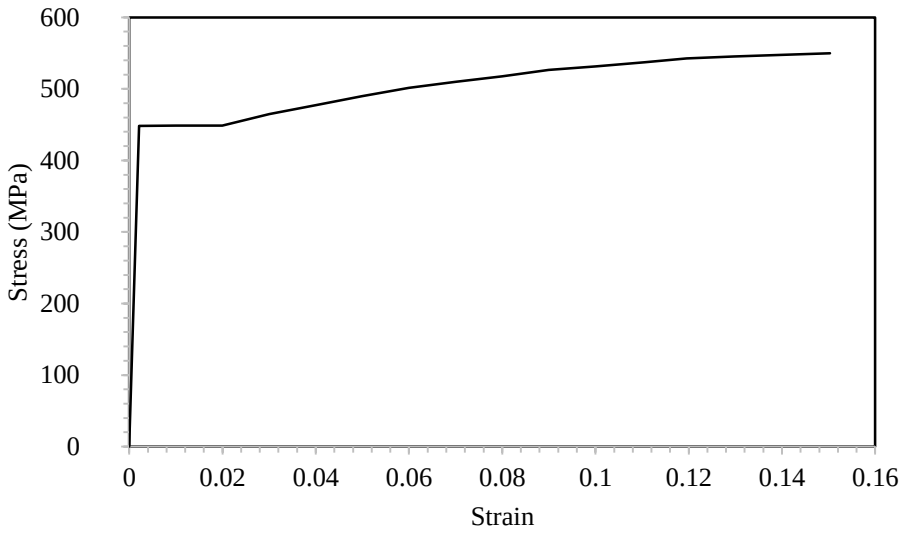

Fig. 2.3 Nominal stress-strain diagram for X65 material.

Table 2.1 Strain-stain pairs of data for X65 steel.

Stress (σ) (MPa)	Strain (e) (%)
0.00	0.00
448.44	0.21
448.50	1.00
448.51	2.00
464.99	3.00
477.48	4.00
490.02	5.00
501.32	6.00
509.98	7.00
517.50	8.00
526.32	8.99
531.31	10.00
537.24	11.05
542.74	11.95
545.16	12.97
547.53	13.99
549.86	15.03

However, the above data pairs should be transformed into true stress (σ_T)-logarithmic plastic strain ($\varepsilon^{pl}{}_{ln}$) pairs for their assignment to ABAQUS numerical framework. The equations that relate true and nominal stress-strain pairs are listed bellow

$$\sigma_T=\sigma\,(1+e)$$
$$\varepsilon^{pl}{}_{ln} = \ln(1+e) - \frac{\sigma_T}{E} \tag{2.9}$$

By applying the tabulated data of **Table 2.1** to (2.9) set of equations, σ_T- $\varepsilon^{pl}{}_{ln}$ pairs are produced, (**Table 2.2**) and thus the chart of true stress- logarithmic plastic strain is created (**Fig. 2.4**).

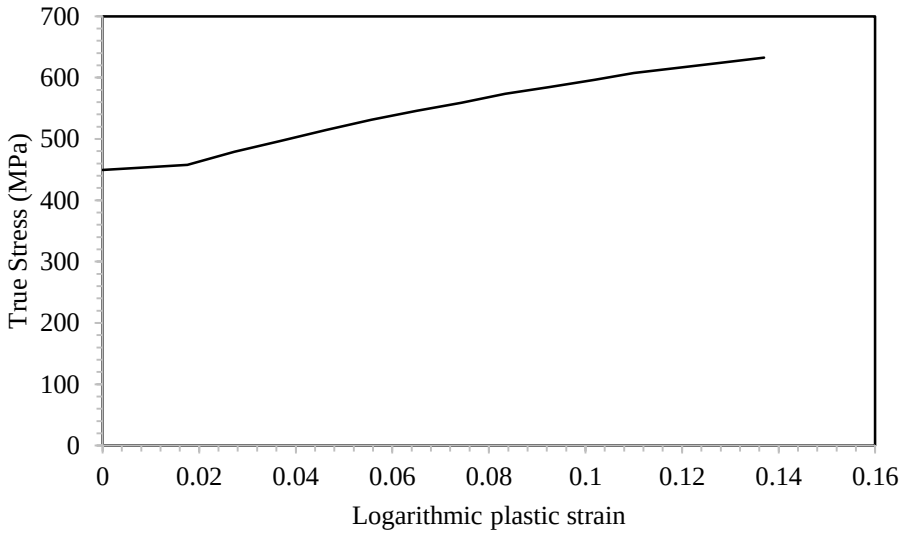

Fig. 2.4 True stress- logarithmic plastic strain diagram for X65 material.

Table 2.2 True stress- logarithmic plastic strain pairs of data for X65 steel.

True stress (σ_T) (MPa)	Logarithmic plastic strain (ε^{pl}_{ln}) (%)
449.40	0.00
452.99	0.78
457.47	1.76
478.95	2.73
496.60	3.69
514.50	4.63
531.38	5.57
545.70	6.51
558.90	7.43
573.67	8.34
584.43	9.25
596.63	10.20
607.60	11.00
615.85	11.90
624.15	12.80
632.50	13.70

2.3.1 Numerical modeling of rings with initial ovality

As it was mentioned in the beginning of section 2.3, a quarter of a ring is considered for the analysis of the mechanical response of a ring under external pressure. Rings of three different values of D/t are modeled with initial ovality imperfection of 0.01%. Their geometric characteristics are listed in **Table 2.3**. The initial ovality is assigned to the models by creating quadrant ellipse cross-sections. All the rings are discretized using four-node, reduced-integration plane-strain finite elements, which are defined as CPE4R in ABAQUS. The mesh in all cases consists of 50 elements in the circumferential direction and 8 elements in the through-thickness direction. Therefore, the model is discretized by a total number of 400 elements. Symmetry boundary conditions are applied at the bottom and top sides of the model. More specifically, «YSYMM» boundary conditions are applied at the bottom side to restrict the body's displacement in Y direction and its rotation about X and Z directions, and «XSYMM» boundary conditions are applied at the top side so that the body will not be able to translate in X direction and rotate about Y and Z directions. The finite element mesh used in the finite element models is presented in **Fig. 2.5** for the ring of D/t=40.

Table 2.3 Geometric parameters in terms of outer diameter D and thickness t for different D/t ratios.

D/t	D (mm)	t(mm)
40	600	15
30	610	20
20	410	20

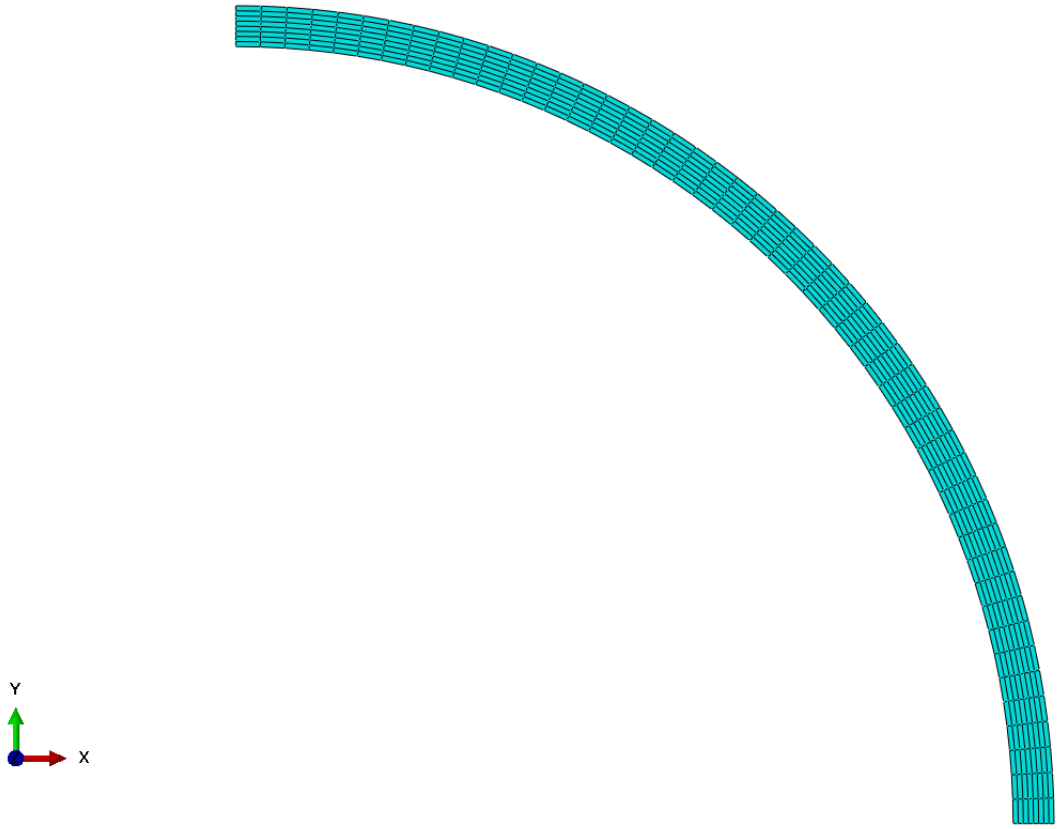

Fig. 2.5 The finite element mesh which is assembled by CPE4R elements (D/t=40).

From the ring buckling analysis of the previous chapter, it is recognized that when the pressure reaches a critical level the ring loses its stability and exhibits non-linear deformation in the post-buckling range. Therefore, the post-buckling deformations of the ring are driven by the four-equally spaced locations of maximum stress around the circumference. The collapse sequence of configurations for the ring of D/t=40 and initial ovality of 0.01%, is presented in **Fig. 2.6**. The numbers above the deformed configurations correspond to the pressure ovality response of **Fig. 2.14**, which will be discussed in section 2.4.1. After the stage of collapse (stage (1)), the top and bottom sides of the ring move towards the center of the cross-section and the left and right sides move away from that. The final collapse configuration (stage (6)) corresponds to the stage of contact between the top and bottom sides of the ring's inner surface. In the numerical models, the translation of the top side through the negative Y axis is restricted by using a two-dimensional analytical rigid surface. Therefore, the surface-to-surface contact method is used, and a contact pair is created between the rigid body and the inner surface of the model. The translation of the model's inner side through the rigid body is aborted by using the penalty method as an interaction property of the pair.

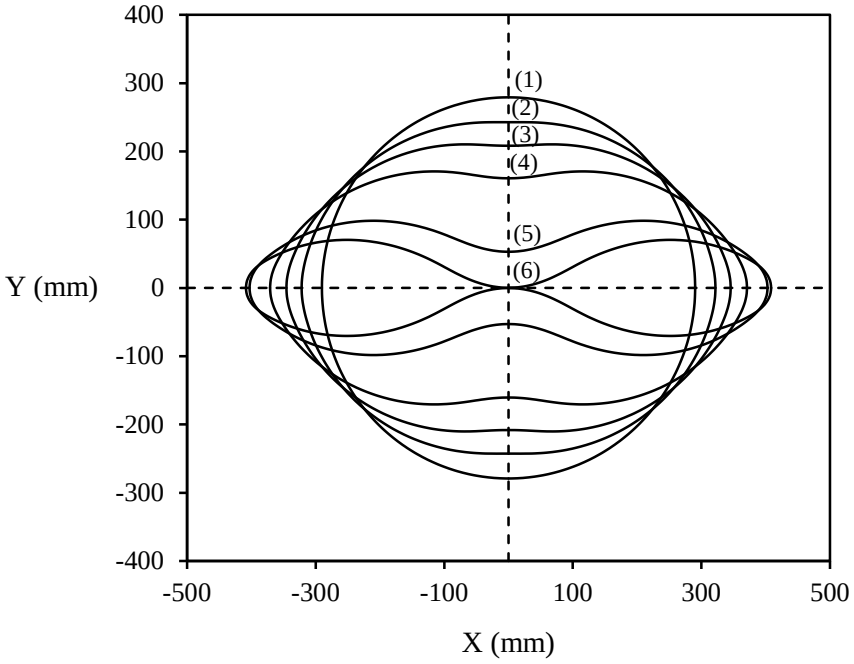

Fig. 2.6 Sequence of collapse configurations of metal ring with D/t=40 ($\Delta_o = 0.01\%$).

The analysis is developed through two steps which are consisted of increments. In the first step, which is denoted as the «initial step» in ABAQUS, the boundary conditions are assigned to the model in the way described above. Also, the displacements and rotations of the analytical rigid body are aborted. That was achieved by using the «ENCASTRE» boundary condition which aborts the displacements and rotations about X, Y, Z axes at a «Reference Point (RP)» of the rigid body. The last step of the analysis (second step) describes the application of external pressure at the outer surface of the model. In this step a nonlinear analysis is conducted using Riks' continuation method, so that the pre-buckling response, the collapse pressure, and the unstable post-buckling response are obtained.

2.3.2 Numerical modeling of rings with initial ovality and eccentricity

In the case of a ring with initial imperfections of both ovality and eccentricity, the numerical modeling differs from that followed in section 2.3.1. A half ring domain is considered for analysis here. Two possible types of eccentricity exist [22], [18]. The first type involves an eccentricity value, which is imposed in Y direction, where the minor-axis of the ellipse exists. In the second type, the eccentricity exists in the X direction and thus, the maximum and minimum values of thickness correspond to the major axis of the ellipse. The ring geometries examined here, are developed with

eccentricity in Y direction (**Fig. 2.2**). Rings of D/t=20 and 30 (**Table 2.3**) are modeled with both ovality and eccentricity in the form of half ellipse cross-sections with imposed thickness eccentricity in Y direction. The models are discretized using four-node, reduced-integration plane-strain finite elements, denoted as CPE4R in ABAQUS. For both D/t values, the mesh consists of 100 elements in the circumferential direction and 8 elements in the through-thickness direction. Therefore, the model is discretized by a total number of 800 elements. The two opposite vertically quarter sides of the model are constrained with the «XSYMM» boundary condition which prescribes zero node displacements in X direction and zero node rotations about the Y and Z axes. Also, «YSYMM» boundary conditions are applied on a node of the outer surface (Y=0 and θ=0) to abort the body's displacement in Y direction and its rotations about the X and Z axes. The finite element mesh used in the numerical modeling, is presented in **Fig. 2.7** for the ring with D/t=20.

The wall thickness variation is assigned to the models using equation (2.7), and thus the inner and the outer ellipse are eccentric by a distance "η" in Y direction. The top side moves inward until it reaches the bottom side. Unless a contact pair restriction is considered between the two sides, the top inner surface will finally pass through the bottom inner surface. In the finite element models, such a translation was aborted by the establishment of self-contact method for the inner surface and the penalty method is used as the interaction property of contact. The steps that develop the analysis of these imperfection models are alike with those described in section 2.3.1. The boundary conditions described above, are stated in the initial step and the uniform external pressure is applied in step 1 using Riks' continuation method.

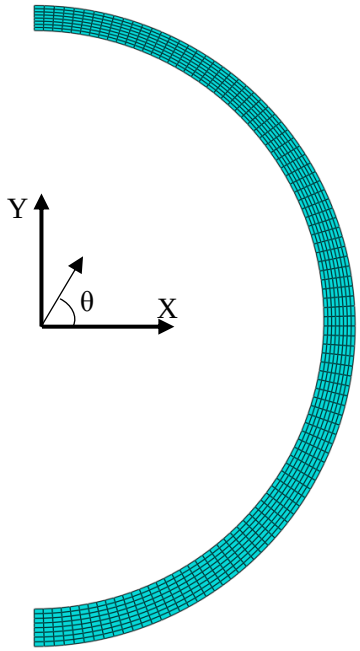

Fig. 2.7 Finite element mesh of half ring model (D/t=20**)**, which is assembled by CPE4R elements.

2.4 Numerical Results

In this section the numerical results will be presented for the initially ovalized models and for the models with imperfection combinations of ovality and eccentricity. Firstly, the initial ovality of 0.01% will be implemented in the models for the examination of the corresponding mechanical response upon external pressure application. Furthermore, the effect of imperfection combinations on the collapse pressure as well as the collapse configurations, will be examined for different pairs of ovality and eccentricity.

2.4.1 Initially ovalized rings

A small initial ovality value of $\Delta_o = 0.01\%$ is considered for the cases of D/t =20, 30 and 40 (**Table 2.3**). The collapse configurations of the imperfect rings are expected to be in the form of **Fig. 2.6**, due to the formation of four equally spaced plastic hinges around the circumference of the ring. This type of collapse mode is present for all of the different D/t ‘s examined. The contours of collapse configurations are presented in the following figures (**Fig. 2.8**-**Fig. 2.11**) for the case of D/t=40.

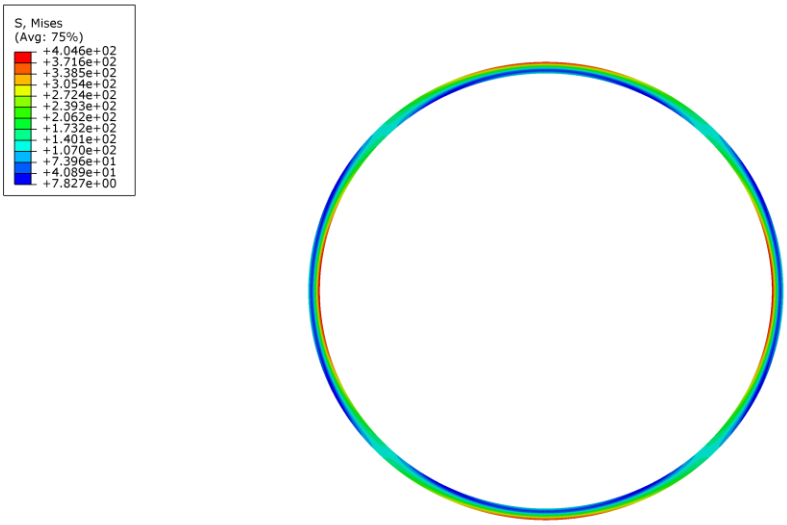

Fig. 2.8 Stage of collapse **(**$D/t = 40,\ \Delta_o = 0.01\%$).

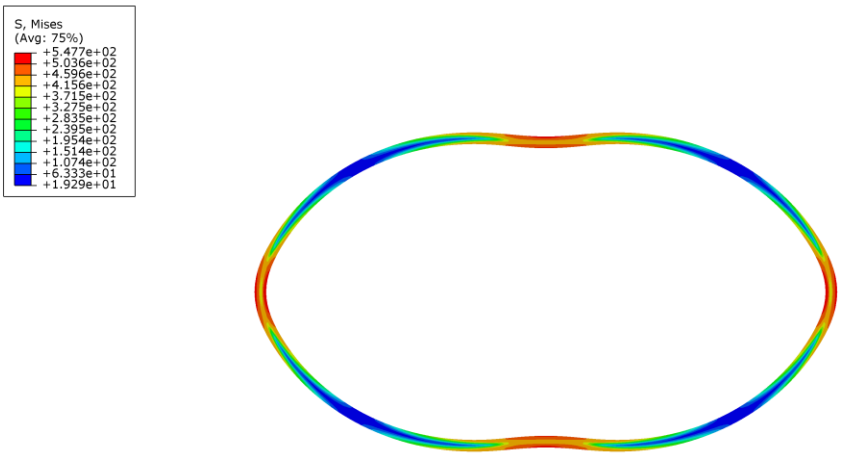

Fig. 2.9 Intermediate stage of the collapse sequence ($D/t = 40,\ \Delta_o = 0.01\%$**)**.

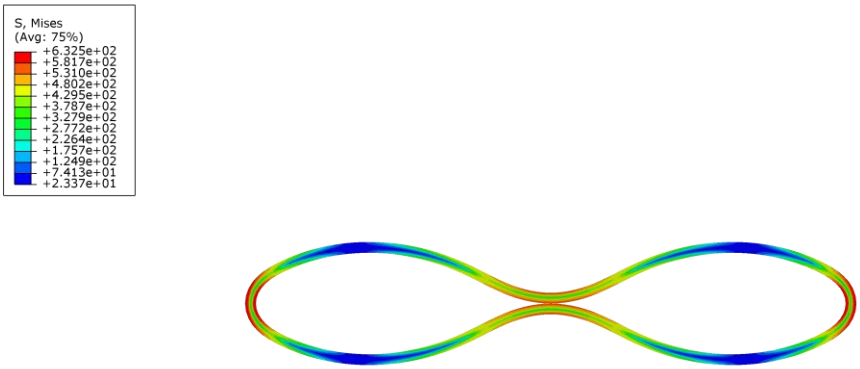

Fig. 2.10 Stage of the first contact between the two opposite quarter sides of the ring's inner circumference ($D/t = 40,\ \Delta_o = 0.01\%$).

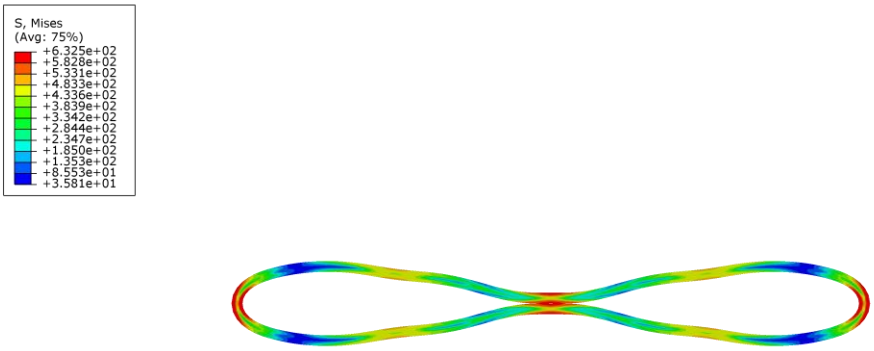

Fig. 2.11 Final stage of the sequence of collapse configurations ($D/t = 40,\ \Delta_o = 0.01\%$).

From (1.19) it is expected that a ring of D/t=40 (here D is the outer diameter) will buckle in the elastic range. At the stage of collapse (**Fig. 2.8**) the ring's maximum stress (404.6 MPa) has not exceeded the material's yield stress, which is 449.4 MPa (**Table 2.2**). Because the imperfection here is

small, one can say that the mechanical behavior of this ring approaches that of the perfect case. Thus, the numerical results show that collapse occurs at a stress which is lower than the yield stress. Equivalent plastic strain contours (**Fig. 2.12**- **Fig. 2.13**) were captured from ABAQUS, and the formation of the four plastic hinges around the circumference is clearly shown, for the previous stages of collapse sequence.

The collapse response of the elastic-plastic rings upon uniform external pressure loading, is expected to develop a limit load which is sensitive to imperfection amplitudes changes [4], [9]. After the collapse stage, the cross-sectional ovalization will be increased, and the pressure carrying capacity of the ring will fall significantly. The pressure-ovality response for the ring of D/t=40 is presented in **Fig. 2.14**. The numbers on the response correspond to the deformed configurations of **Fig. 2.6** and **Fig. 2.8**- **Fig. 2.11**.

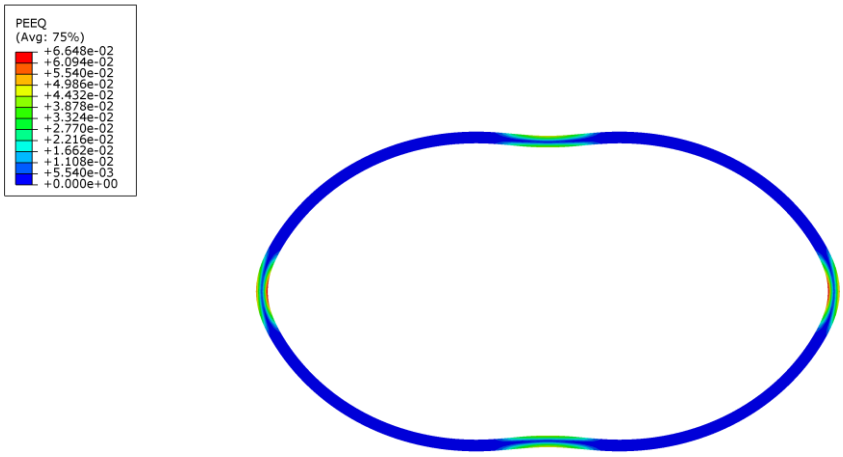

Fig. 2.12 Equivalent plastic strain at an intermediate stage of collapse sequence ($D/t = 40$, $\Delta_o = 0.01\%$).

Fig. 2.13 Equivalent plastic strain at the stage of first contact between the two opposite quarter sides of the ring's inner circumference ($D/t = 40,\ \Delta_o = 0.01\%$**).**

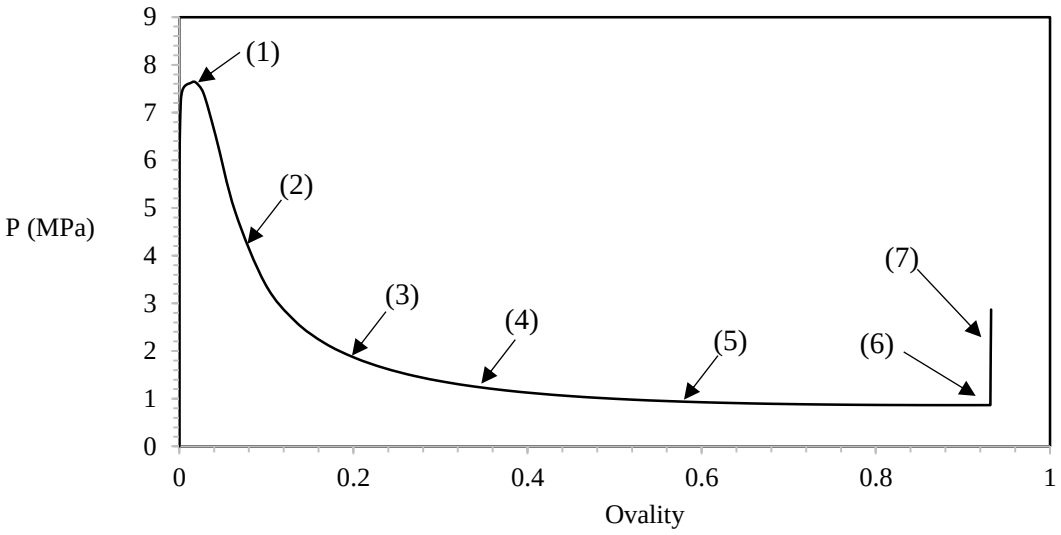

Fig. 2.14 Pressure-ovality response of the initially ovalized ring with D/t=40 ($\Delta_o = 0.01\%$).

The above figure indicate that a limit load is developed in the response, which is the collapse pressure (P_{co}). The maximum collapse capacity of this ring is $P_{co} = 7.64$ MPa, and it is shown at stage (1). After the limit load point, the pressure drops, and the system becomes unstable due to the formation of the plastic hinges [4]. An arbitrary intermediate stage of collapse sequence was presented

in **Fig. 2.9** and it was denoted as stage (3) in **Fig. 2.6** and **Fig. 2.14**. First contact between the bottom and the top side of the ring occurs at stage (6). After first contact, the structure seems reaching stability and a corresponding rising in pressure is observed. Stage (7) corresponds to the deformed configuration of **Fig. 2.11** and is referred to as the final stage of collapse configurations. The critical elastic pressure (1.16) and the yield pressure (1.18) are calculated for the ring of D/t=40 and the results are listed in **Table 2.4**. It can be seen that P_{co} is lower than P_{cr}, indicating that the collapse occurs in the elastic range of the material.

The pressure-ovality response for the ring of D/t=30 is shown in **Fig. 2.15** and the corresponding sequence of collapse configurations is presented in **Fig. 2.16**. The post-buckling deformation becomes restricted to four-equally spaced points around the circumference of the ring. **Fig. 2.17**-**Fig. 2.18** show the equivalent plastic strain contours for an arbitrary intermediate stage of collapse sequence and for the stage of first contact between the bottom and the top side of the inner surface of the ring. It can be seen from **Table 2.4** that the ring of D/t=30 collapses in the elastic range of the material, because the collapse pressure is lower than the critical elastic pressure.

Table 2.4 Collapse pressure (P_{co}), critical elastic pressure (P_{cr}) and yield pressure (P_y) for the rings of D/t=20, 30 and 40. The collapse pressures correspond to an initial ovality value of 0.01%.

D/t	P_{co}	P_{cr}	P_y
20	47.01	62.24	46.09
30	17.53	17.98	30.47
40	7.64	7.78	23.05

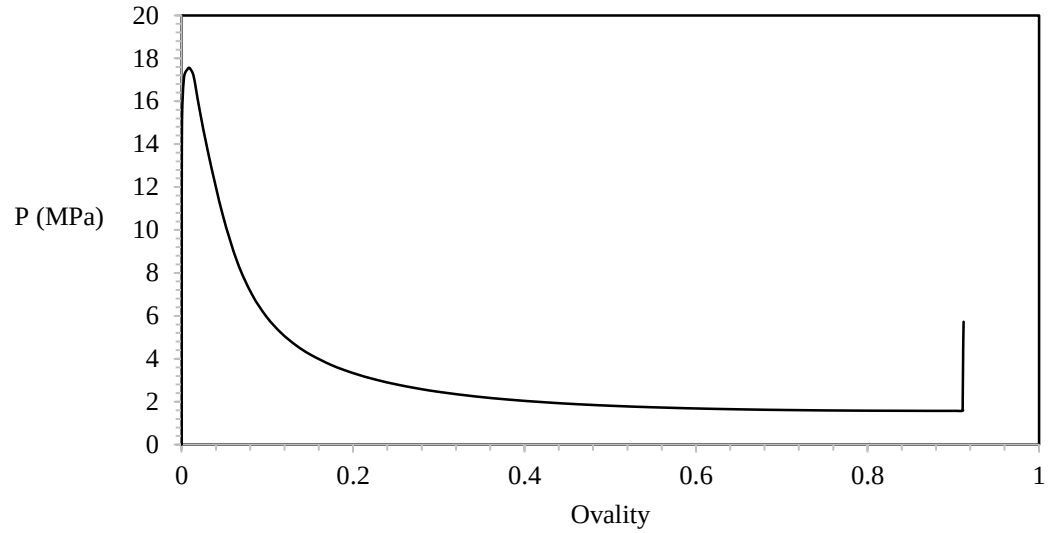

Fig. 2.15 Pressure-ovality response of the initially ovalized ring with D/t=30 ($\Delta_o = 0.01\%$).

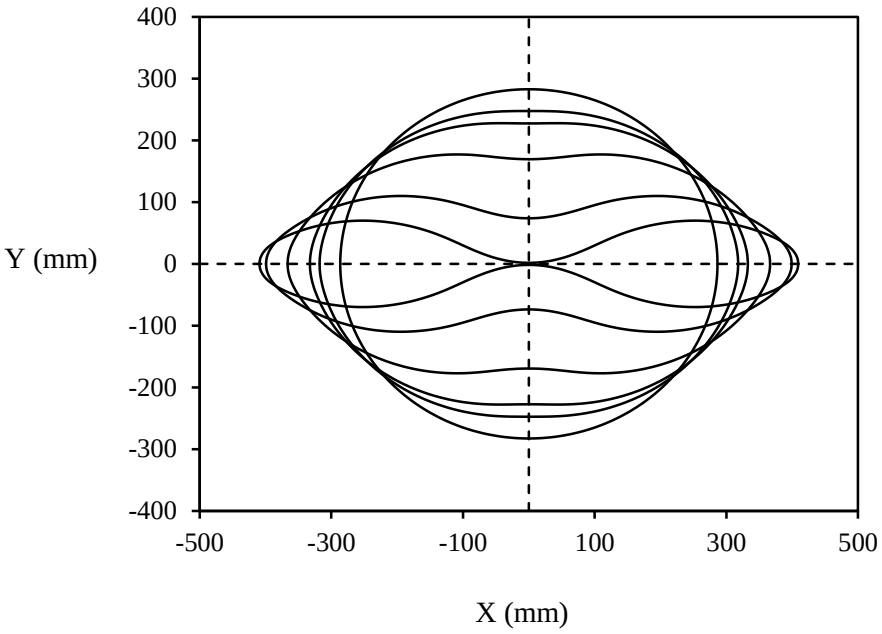

Fig. 2.16 Sequence of collapse configurations of metal ring with D/t=30 ($\Delta_o = 0.01\%$).

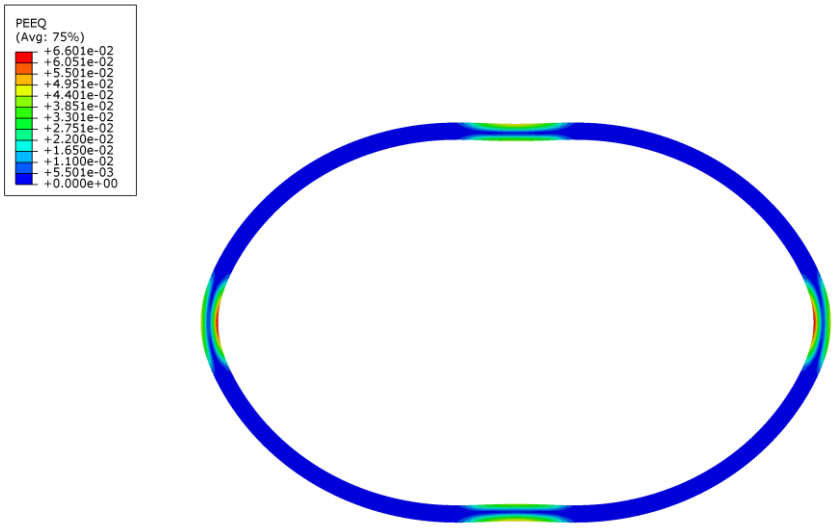

Fig. 2.17 Equivalent plastic strain at an intermediate stage of collapse sequence (D/t=30 , $\Delta_o = 0.01\%$).

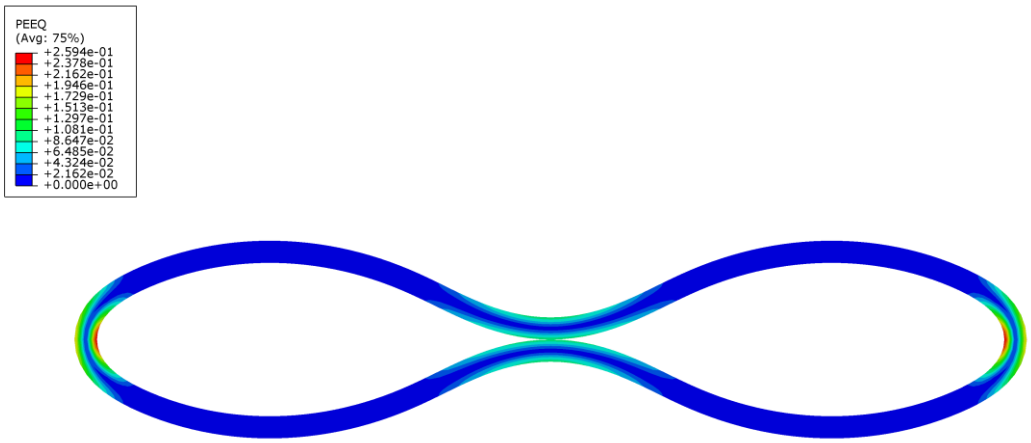

Fig. 2.18 Equivalent plastic strain at the stage of first contact between the two opposite quarter sides of the ring's inner circumference (D/t=30, $\Delta_o = 0.01\%$).

The pressure-ovality response and the corresponding sequence of collapse configurations, are presented for the ring of D/t=20 in **Fig. 2.19** and **Fig. 2.20** respectively. The post-buckling behavior is like that observed in the previous ring cases. The formation of four plasticized locations at the quarter points of the ring is shown by the equivalent plastic strain contours for the ring of D/t=20 (**Fig. 2.21**-**Fig. 2.22**). The results of **Table 2.4** show that the ring of D/t=20 follow the plastic buckling mode of collapse because the collapse pressure has exceeded the yield pressure.

The three rings have a common value of initial imperfection and different geometries. The results show that the collapse pressure varies with the D/t ratio. Therefore, the D/t and generally the geometric characteristics of the rings, significantly influence the collapse capacity of these structures. The influence of geometric parameters on the collapse pressure will be examined through parametric studies in section 2.5.3.

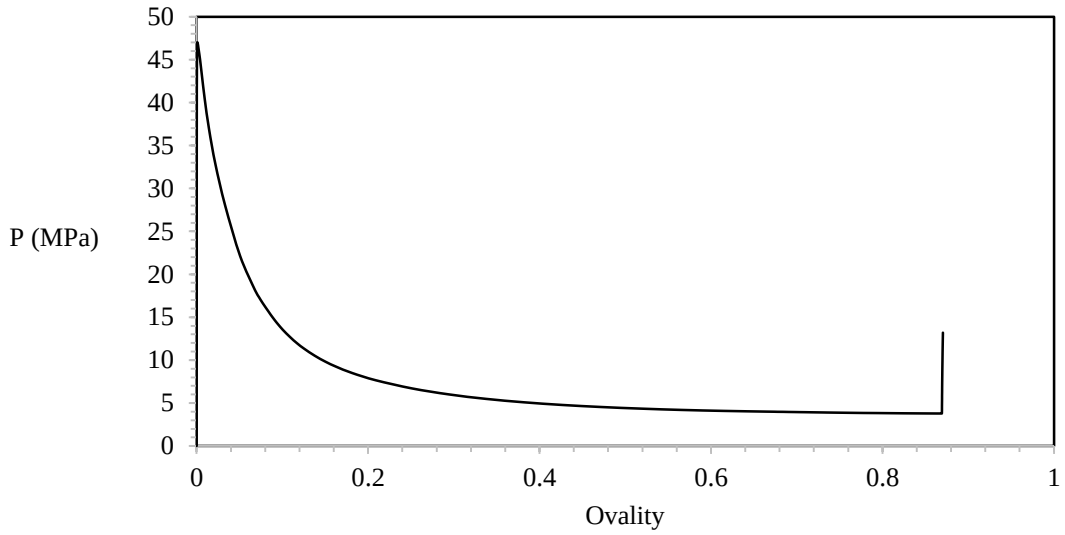

Fig. 2.19 Pressure-ovality response of the initially ovalized ring with D/t=20 ($\Delta_o = 0.01\%$).

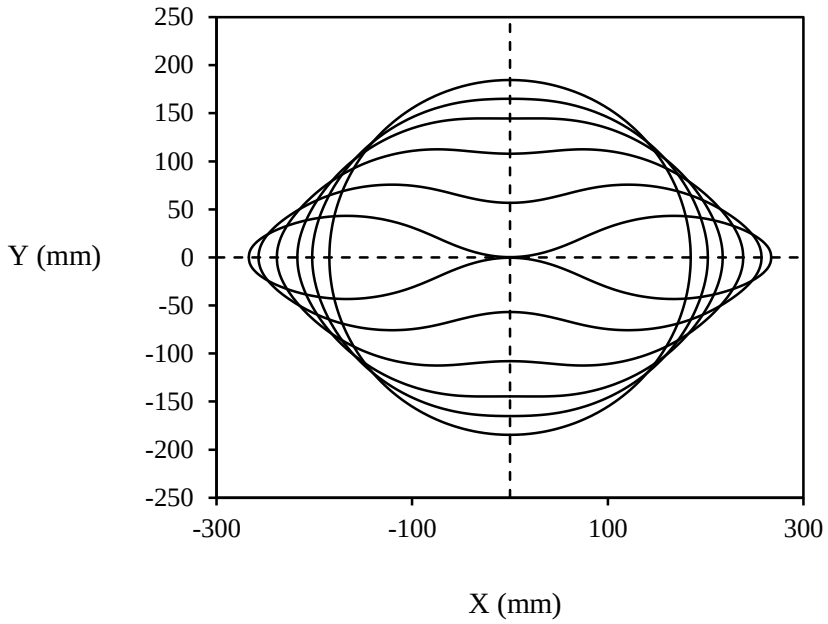

Fig. 2.20 Sequence of collapse configurations of metal ring with D/t=20 ($\Delta_o = 0.01\%$).

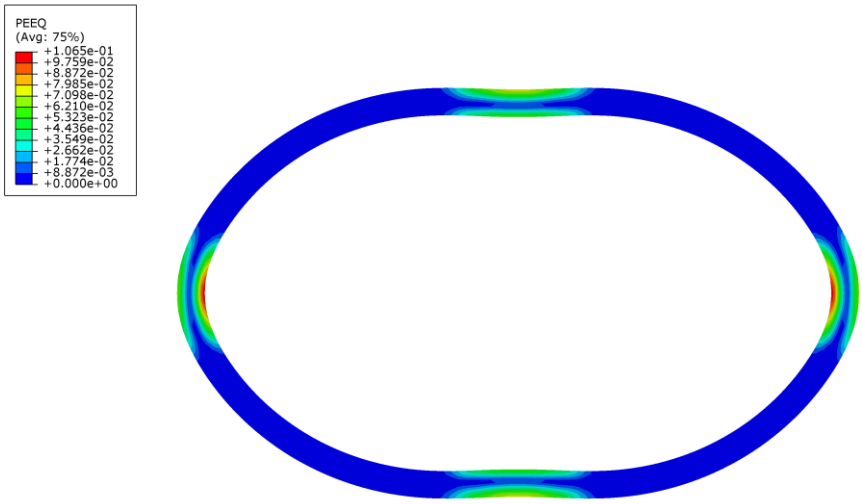

Fig. 2.21 Equivalent plastic strain at an intermediate stage of collapse sequence (D/t=20, $\Delta_o = 0.01\%$).

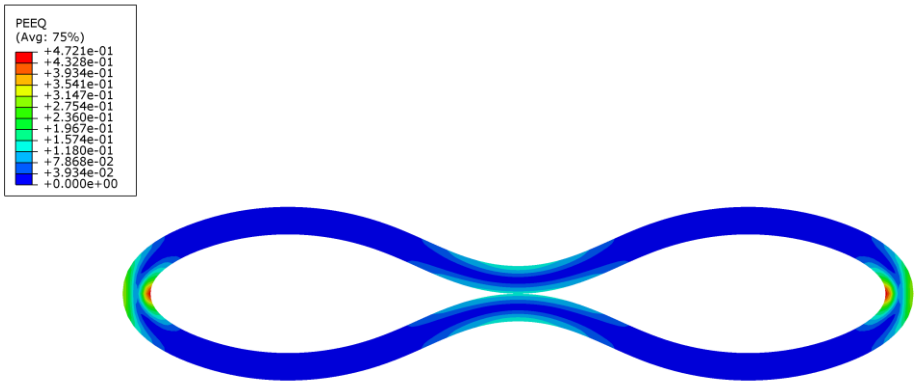

Fig. 2.22 Equivalent plastic strain at the stage of first contact between the two opposite quarter sides of the ring's inner circumference (D/t=20, $\Delta_o = 0.01\%$).

2.4.2 Initially ovalized rings with thickness eccentricity

Different pairs of imperfection amplitudes were implemented in the ring models of D/t =20, 30 (**Table 2.3**) for the examination of their combined effects on both the collapse mode and the collapse capacity of the rings. For the ring of D/t=20, a pair of small ovality and large eccentricity is considered to pronounce the effect of eccentricity on the collapse response of the structure. Therefore, the ring is modeled with a combined imperfection of $\Delta_o = 0.05\%$ and $\Xi_o = 20\%$, and their collapse configurations are presented in **Fig. 2.23**-**Fig. 2.25**. The concentration of high stresses in the areas of the "crown", and the "shoulder" (**Fig. 2.24**) make these locations perform like plastic hinges and the structure behaves like a plastic mechanism. Apparently, the collapse response in this numerical simulation differs significantly from the collapse response observed in the initially ovalized rings without eccentricity (Section 2.4.1). The reason can be attributed to the cumulative plastic deformation at the locations of "crown" and "shoulder" as it is presented in **Fig. 2.26**. The final configuration is non-symmetrical about the X axis (**Fig. 2.25**) and thus the ring follows a mode "U" sequence of collapse [18].

For the ring of the same geometric characteristics, a pair of strong initial ovality and weak initial eccentricity imperfection is considered. For this case, the ring modeling constitutes of imperfection amplitudes $\Delta_o = 1.6\%$ and $\Xi_o = 5\%$ (**Fig. 2.27**-**Fig. 2.29**). Unlike the previous case, the ovality effect is quite distinguishable here. The ring plasticizes at four locations around the circumference (**Fig. 2.28** and **Fig. 2.30**), and thus the structure performs like a plastic mechanism. The collapse mode here is a reminiscent of that observed in the initially ovalized rings without eccentricity (Section 2.4.1). The main difference is observed at the final stage of collapse (**Fig. 2.29**) because the top moves a larger displacement than the bottom. This collapse behavior can be attributed to eccentricity effects, which result in the nonsymmetrical about the X axis response at the final stage of collapse.

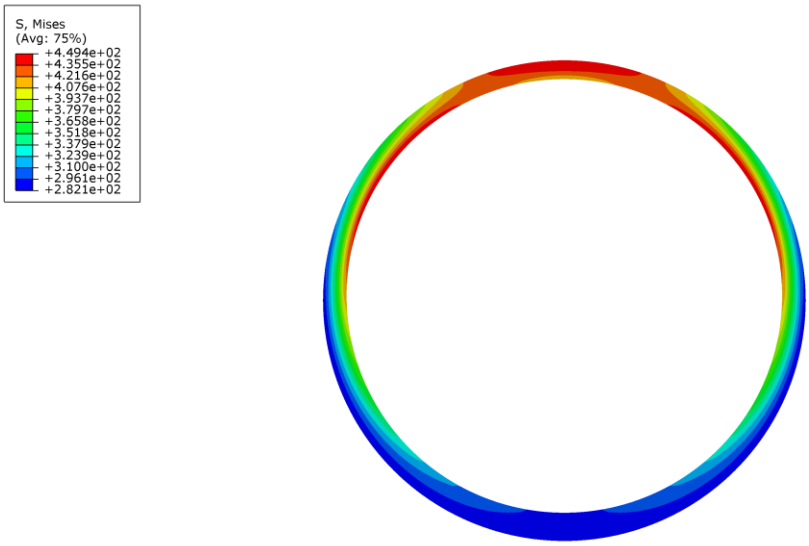

Fig. 2.23 Ring configuration at the stage of collapse (D/t=20, $\Delta_o = 0.05\%$ and $\Xi_o = 20\%$).

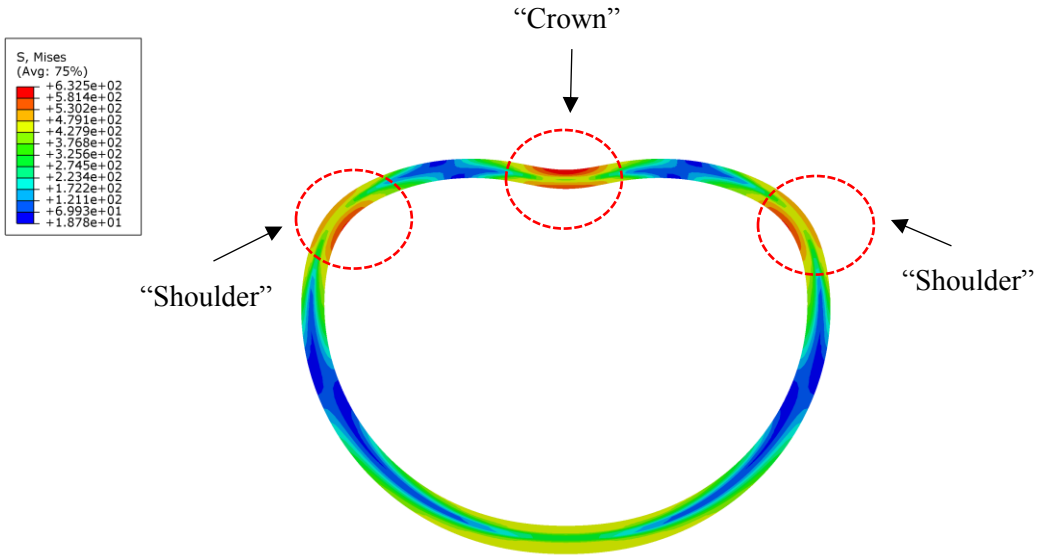

Fig. 2.24 Numerical simulation of ring deformation at an intermediate stage of the collapse sequence (D/t=20, $\Delta_o = 0.05\%$ and $\Xi_o = 20\%$).

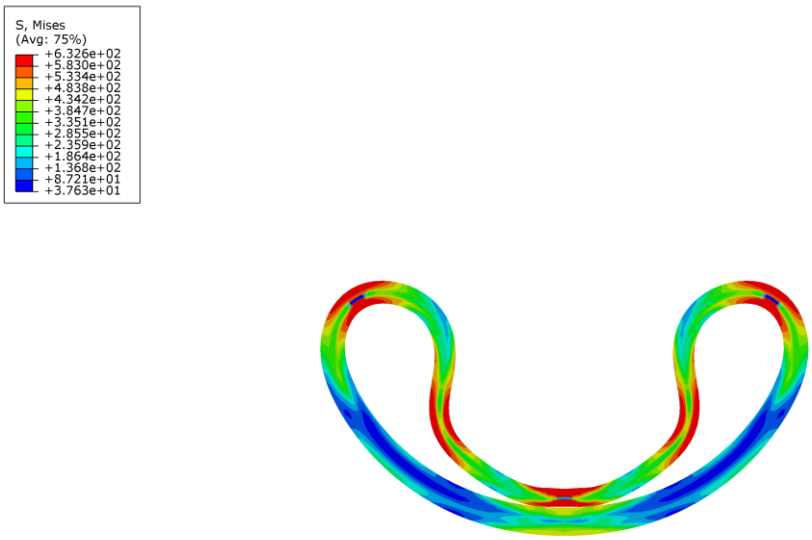

Fig. 2.25 Numerical simulation of ring deformation at the final stage of collapse (D/t=20, $\Delta_o = 0.05\%$ and $\Xi_o = 20\%$).

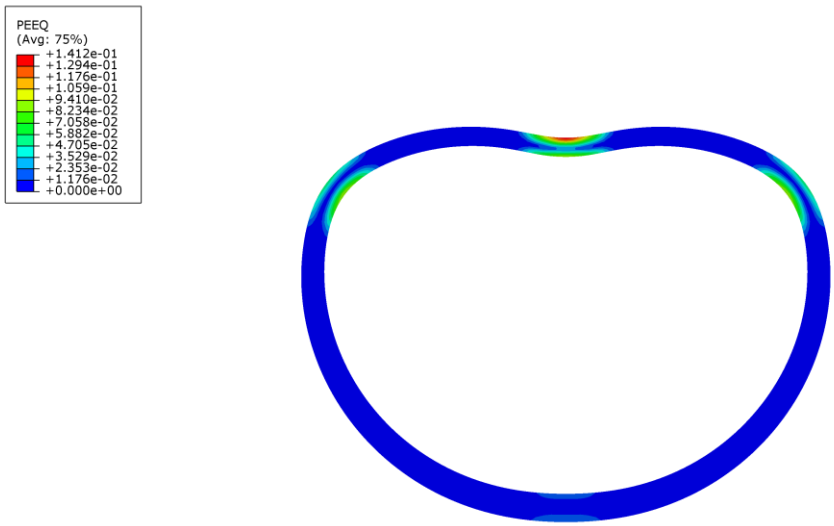

Fig. 2.26 Equivalent plastic strain at an intermediate stage of the collapse sequence (D/t=20, $\Delta_o = 0.05\%$ and $\Xi_o = 20\%$).

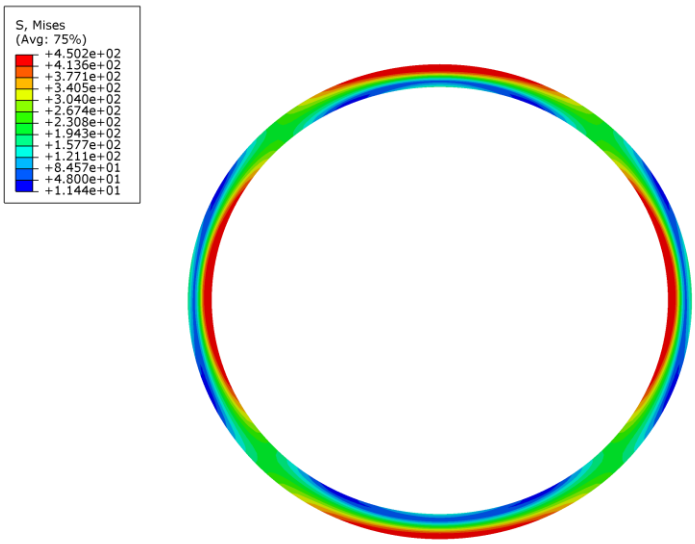

Fig. 2.27 Ring configuration at the stage of collapse (D/t=20, $\Delta_o = 1.6\%$ and $\Xi_o = 5\%$).

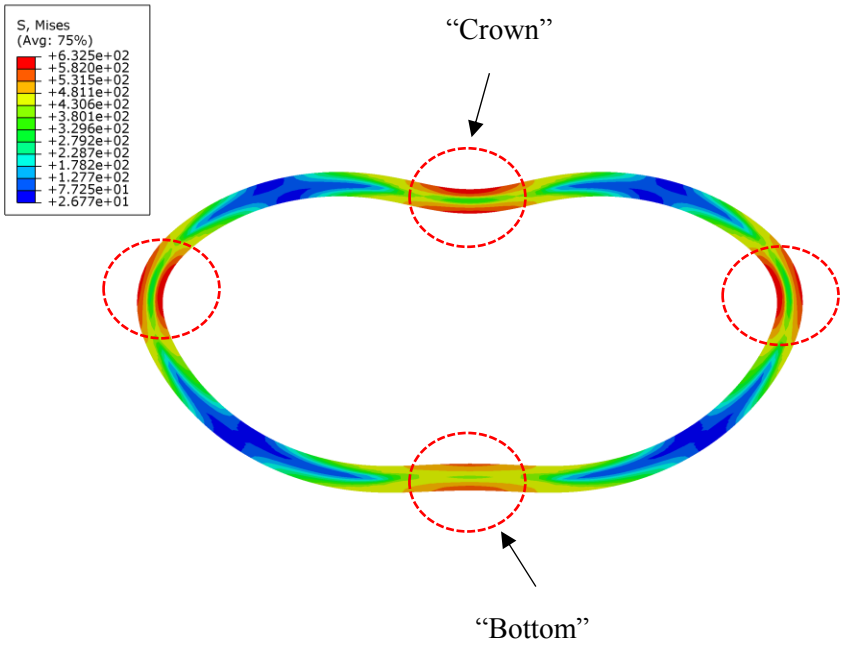

Fig. 2.28 Numerical simulation of ring deformation at an intermediate stage of the collapse sequence (D/t=20, $\Delta_o = 1.6\%$ and $\Xi_o = 5\%$).

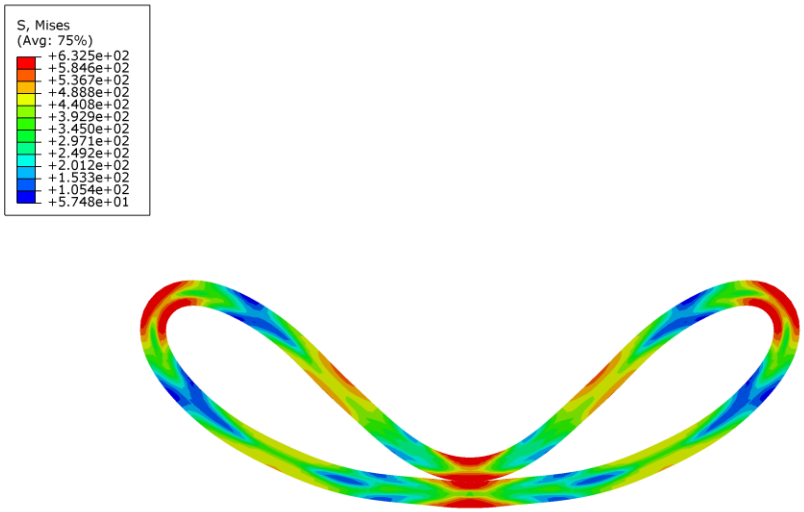

Fig. 2.29 Numerical simulation of ring deformation at the final stage of collapse (D/t=20, $\Delta_o = 1.6\%$ and $\Xi_o = 5\%$).

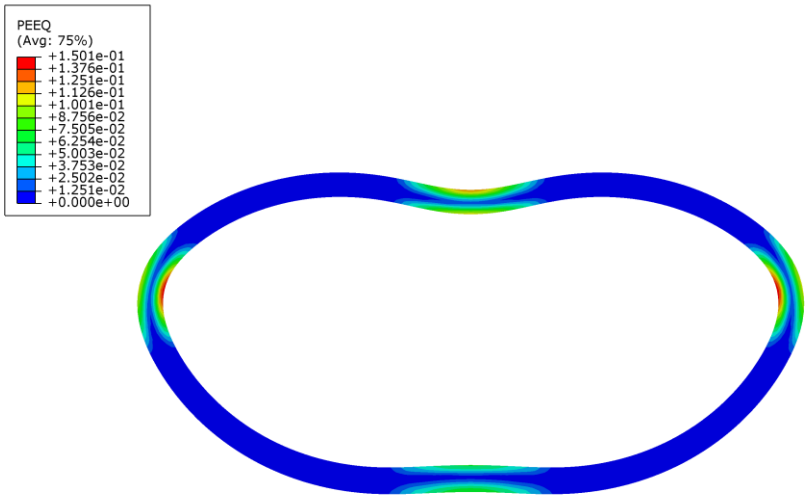

Fig. 2.30 Equivalent plastic strain at an intermediate stage of the collapse sequence (D/t=20, $\Delta_o = 1.6\%$ and $\Xi_o = 5\%$).

The variation of pressure with the deformed cross-sectional ring area is examined for every case of imperfection combination. For the ring considered above with imperfections of pronounced eccentricity ($\Delta_o = 0.05\%$ and $\Xi_o = 20\%$), the pressure versus change in area response is shown in **Fig. 2.31**. The response of zero initial eccentricity and initial ovality of 0.05%, for the examined ring geometry, is included in the same figure for comparison. As the wall thickness variation rises, the drop in the collapse pressure rises as well. Moreover, the influence of eccentricity is strong in the post-buckling regions and weak in the pre-buckling regions of the responses. For the same ring geometry (D/t=20) with imperfections of pronounced ovality ($\Delta_o = 1.6\%$ and $\Xi_o = 5\%$), the variation of pressure with the change in the enclosed ring area is demonstrated in **Fig. 2.32**. The response of zero eccentricity and 1.6% initial ovality is included in the graph as well. The small increasement in the wall thickness variation from $\Xi_o = 0\%$ to $\Xi_o = 5\%$, under a constant ovality of $\Delta_o = 1.6\%$, corresponds to minor changes in the collapse capacity of the ring. Also, the pre-buckling and the post-buckling behaviors are not affected by the increase in wall thickness variation imperfection.

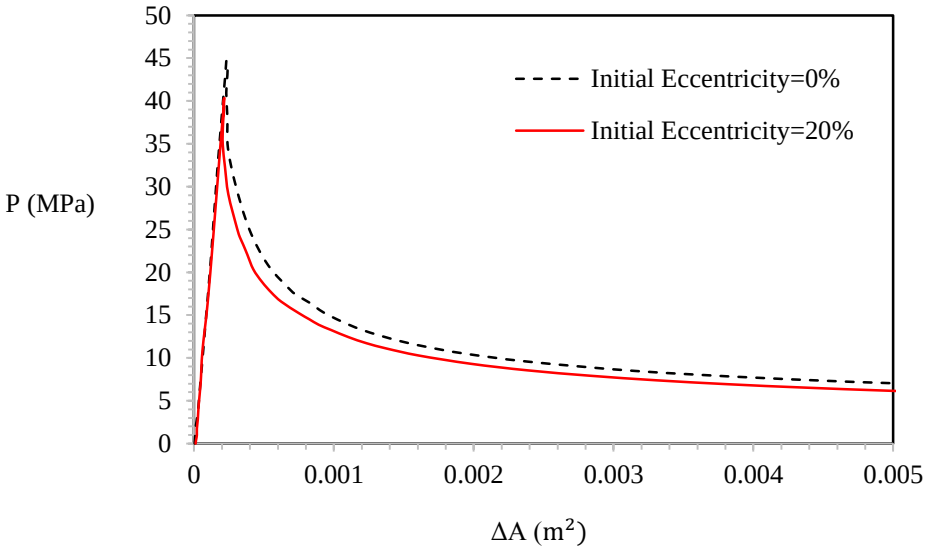

Fig. 2.31 Pressure versus change in area responses of constant ovality $\Delta_o = 0.05\%$ and varied initial eccentricity (D/t=20).

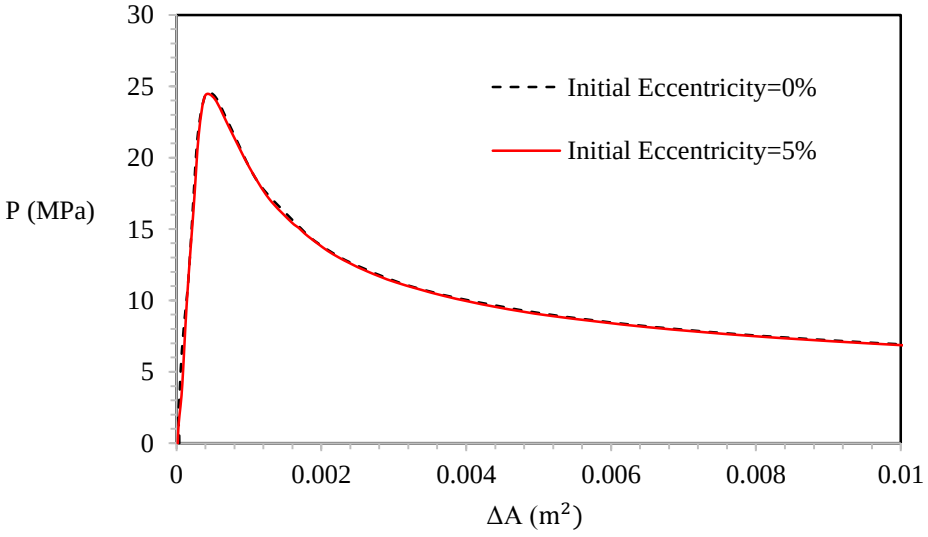

Fig. 2.32 Pressure versus change in area responses of constant ovality $\Delta_o = 1.6\%$ and varied initial eccentricity (D/t=20).

The combined effect of ovality and eccentricity is examined also for the ring with D/t=30, and the analysis proceeds with the same pairs of imperfections used for D/t=20. The ring with $\Delta_o = 0.05\%$ and $\Xi_o = 20\%$ exhibits the "U" collapse mode, due to the pronounced eccentricity effects, and the corresponding collapse mode of the ring with $\Delta_o = 1.6\%$ and $\Xi_o = 5\%$ is like those presented in **Fig. 2.27-Fig. 2.29**. Therefore, the contours of collapse modes for D/t=30 are not included, due to the similarities with the previous ring. The pressure versus change in area responses are shown in **Fig. 2.33** and **Fig. 2.34** for the cases of strong ($\Delta_o = 0.05\%$ and $\Xi_o = 20\%$,) and weak eccentricity ($\Delta_o = 1.6\%$ and $\Xi_o = 5\%$) respectively. The responses of zero eccentricity are included in both figures. It is observed that the effects of wall thickness variation are pronounced for high changes in the initial eccentricity value, whereas minor differences between the responses are observed for small changes in the initial eccentricity value. The influence of initial eccentricity on the collapse pressure will be examined through parametric studies in section 2.5.2.

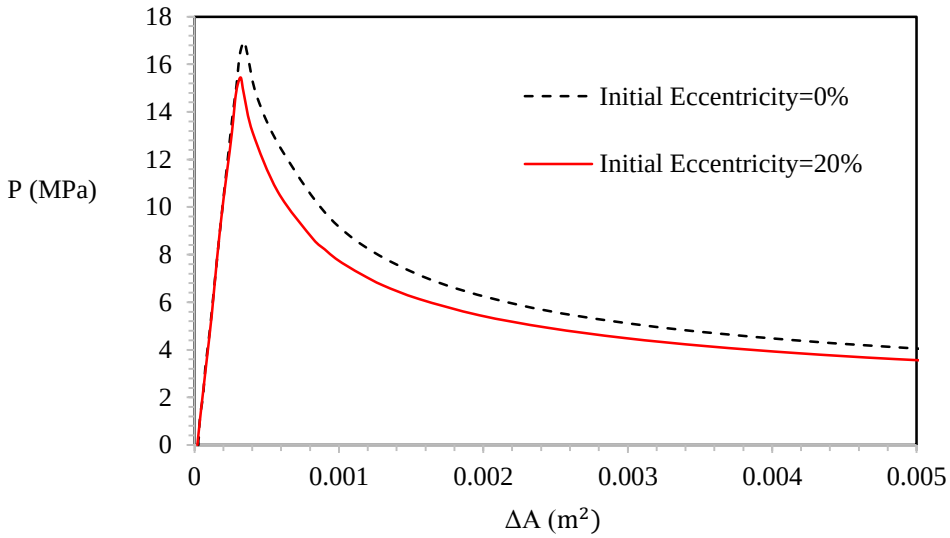

Fig. 2.33 Pressure versus change in area responses of constant ovality $\Delta_o = 0.05\%$ and varied initial eccentricity (D/t=30).

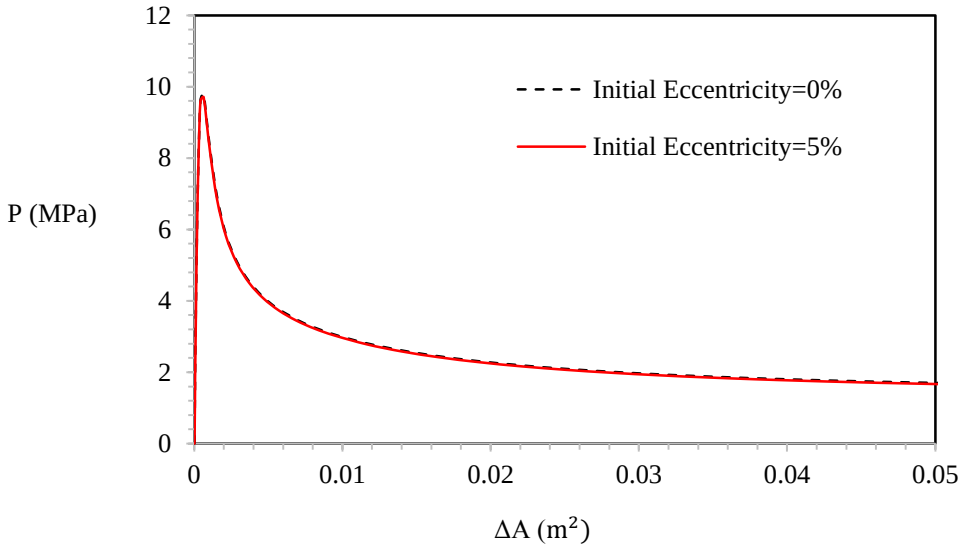

Fig. 2.34 Pressure versus change in area responses of constant ovality $\Delta_o = 1.6\%$ and varied initial eccentricity (D/t=30).

2.5 Parameter Study on Factors affecting Collapse Pressure

The parametric dependence of the collapse pressure will be examined in this section. Up to this point, it has been demonstrated that the collapse pressure is sensitive to initial ovality imperfection and depends on the geometrical parameters of the ring. Therefore, it can be concluded that the collapse pressure is a function of Δ_o and D/t. Furthermore, it has been demonstrated that when wall thickness variation is assigned to the models, the collapse pressure is affected and varies with D/t. However, pipes are usual to exhibit anisotropic yielding and they always consist of residual stresses (RS), which are induced from the manufacturing process. As it was discussed in the introductory section 2.1, these parameters affect the collapse capacity of pipes, and thus they will be examined in the following parametric studies of rings. Therefore, the collapse pressure is expressed as a function of the influencing parameters as follows

$$P_{co} = f\left(\Delta_o, \Xi_o, \frac{D}{t}, \sigma_y, RS\right)$$

2.5.1 Initial Ovality

A set of four different initial ovality values will be inserted into the models of different D/t's, discussed in section 2.4.1. The initial ovality value of $\Delta_o = 0.01\%$ has already been considered and thus, models of $\Delta_o = 0.05\%, 0.1\%, 0.5\%$ and 1% have been created for the three D/t rings. Therefore, twelve additional models were developed in ABAQUS numerical framework. The following pressure-ovality responses (**Fig. 2.35- Fig. 2.37**), represent the detrimental effect of initial ovality on the collapse pressure of the three D/t ring cases. The collapse pressures of the initially ovalized rings are listed in **Table 2.5**. From the figures and the table, it is obvious that the higher the initial ovality value, the lower the corresponding collapse pressure.

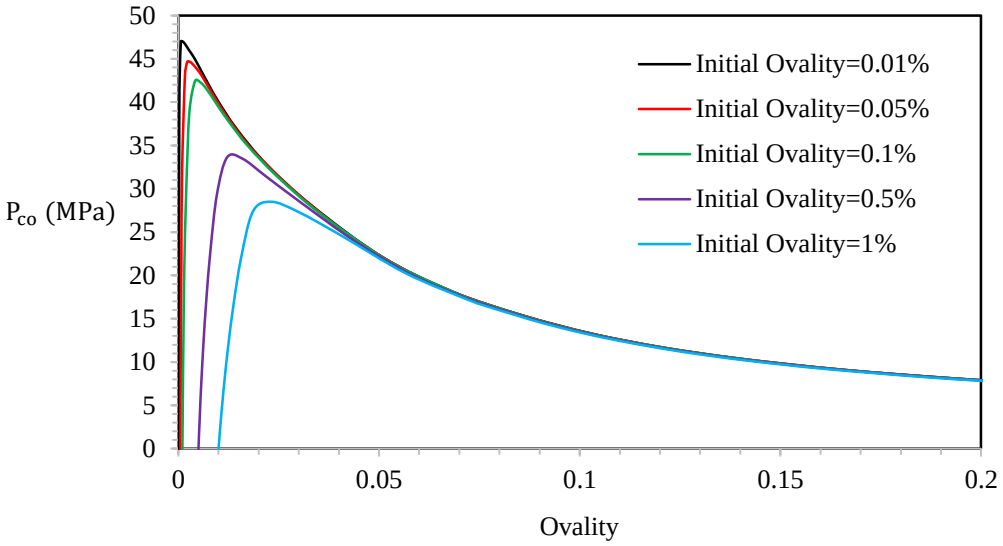

Fig. 2.35 Pressure-ovality responses for different magnitudes of initial ovality (D/t=20).

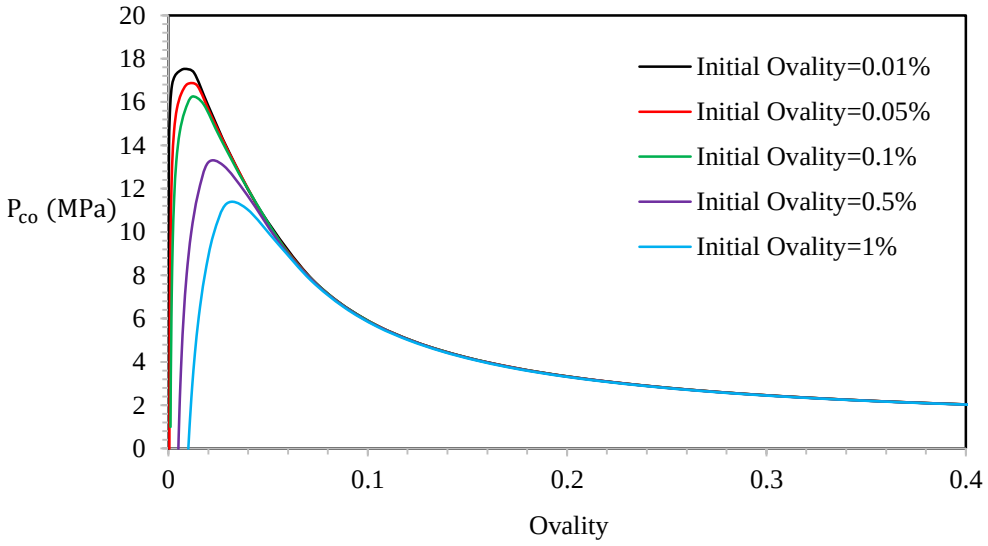

Fig. 2.36 Pressure-ovality responses for different magnitudes of initial ovality (D/t=30).

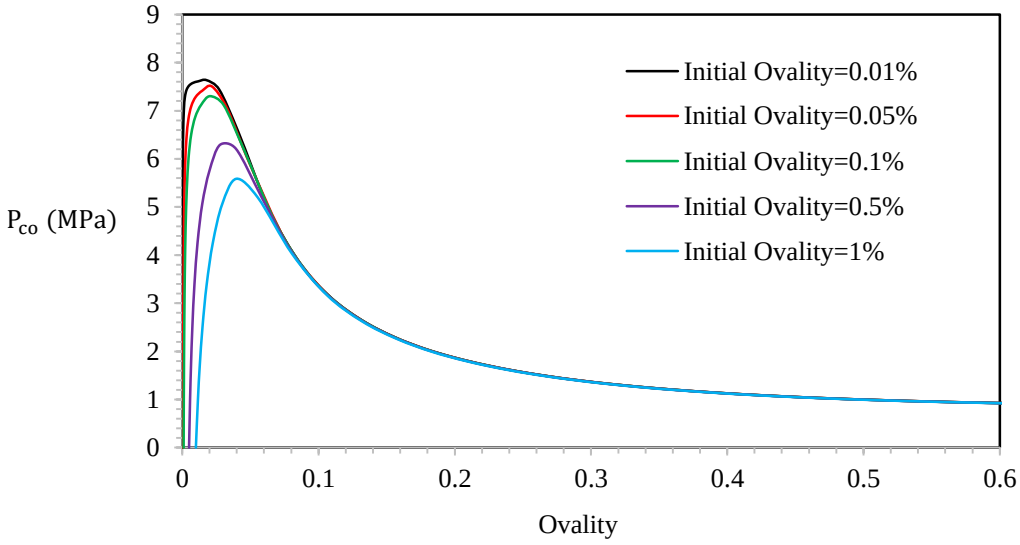

Fig. 2.37 Pressure-ovality responses for different magnitudes of initial ovality (D/t=40).

Table 2.5 Collapse pressure (MPa) for initially ovalized rings of D/t=20, 30 and 40.

D/t	$\Delta_o = 0.01\%$	$\Delta_o = 0.05\%$	$\Delta_o = 0.1\%$	$\Delta_o = 0.5\%$	$\Delta_o = 1\%$
20	47.01	44.63	42.46	33.63	28.50
30	17.53	16.83	16.25	13.20	11.31
40	7.64	7.50	7.30	6.29	5.59

Apparently, it can be concluded that the collapse pressures of the ring cases, examined above, are imperfection sensitive. The collapse pressure and the normalized collapse pressure by P_y (1.18), are plotted against initial ovality, for every ring geometry (D/t=20, 30 and 40) and the results are demonstrated in **Fig. 2.38**. The collapse pressure decreases as the magnitude of imperfection (initial ovality) rises. However, as the D/t is getting smaller the collapse pressure drop rises significantly. For instance, the collapse pressure drop is 18.51 MPa and 2.05 MPa in the cases of D/t =20 and D/t=40 respectively. Therefore, the impact of initial ovality on the collapse pressure is being diminished as the D/t is getting higher.

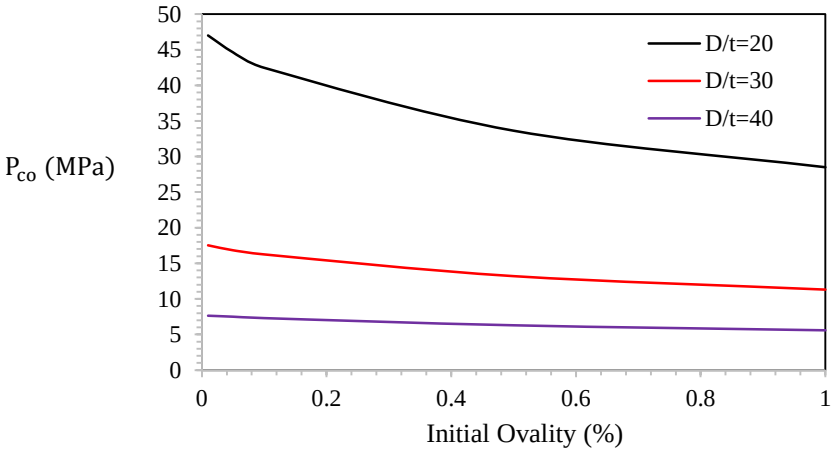

(a)

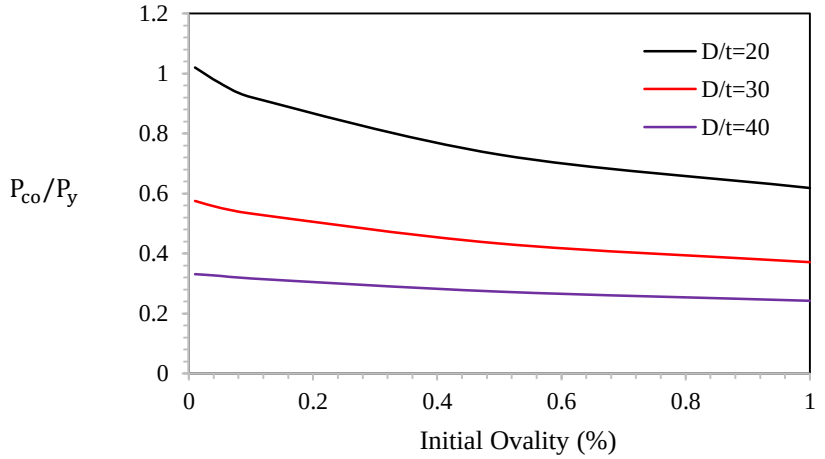

(b)

Fig. 2.38 The variation of the collapse and normalized pressure by P_y with initial ovality for various ring geometries.

2.5.2 Initial Eccentricity

The effect of wall thickness variation on the collapse pressure of rings, discussed in section 2.4.2, will be further investigated here for various values of initial eccentricity. The cases of $\Xi_o = 0\%, 5\%, 10\%, 15\%$ and 20%, will be examined for the initially ovalized rings of section 2.4.2. Therefore, twenty models have been created in ABAQUS standard. The collapse pressures of the rings are tabulated in **Table 2.6**. From the table it can be interpreted that the collapse pressure decreases with increasement of the imperfection amplitudes. The influence of wall thickness variation on the pressure versus change in area responses, is shown in **Fig. 2.39** for all the induced values of initial eccentricities for the ring of D/t=20 with 0.05% initial ovality value. As it can been seen from the plot, the effects of eccentricity are pronounced in the post buckling region. The higher the value of eccentricity the lower the corresponding collapse pressure. On the contrary, minor changes are observed in the pre buckling regions of the responses. The same conclusions are reached when it comes to the case of D/t=30 with 1.6 % initial ovality value (**Fig. 2.40**). Pressure-change in area responses have also been created for the cases of D/t=20 with $\Delta_o = 1.6\%$ and D/t=30 with $\Delta_o = 0.05\%$ and they are not included here because they are of the same type as those of **Fig. 2.39**- **Fig. 2.40**.

Table 2.6 Collapse pressure (MPa) for rings of D/t=20 and D/t=30.

	D/t=20		D/t=30	
Ξ_o (%)	$\Delta_o = 0.05\%$	$\Delta_o = 1.6\%$	$\Delta_o = 0.05\%$	$\Delta_o = 1.6\%$
0	44.63	24.43	16.95	9.78
5	44.44	24.33	16.75	9.70
10	43.74	23.97	16.50	9.50
15	42.46	23.40	16.08	9.24
20	40.34	22.61	15.44	8.96

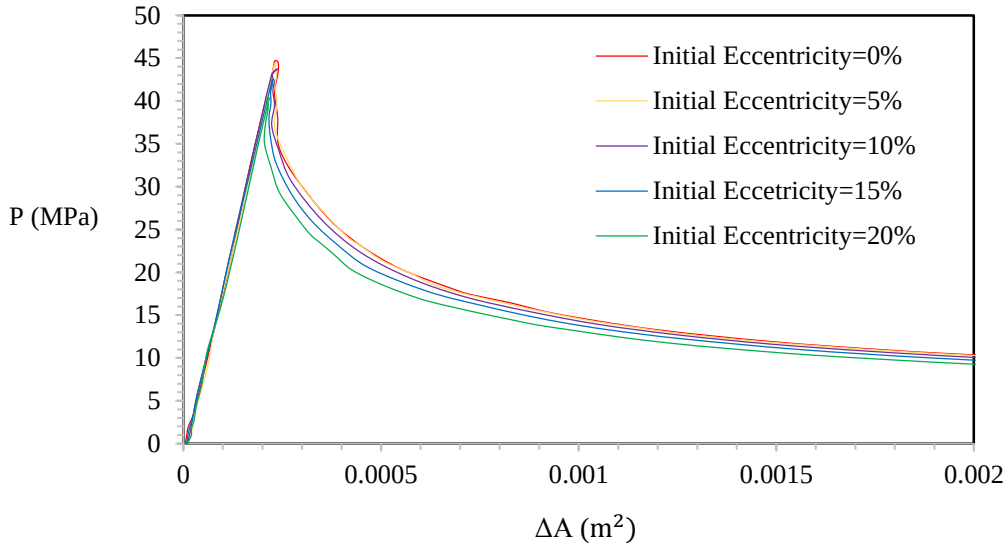

Fig. 2.39 Pressure versus change in area responses of initially ovalized rings for different values of initial eccentricity in Y direction (D/t=20, $\Delta_o = 0.05\%$).

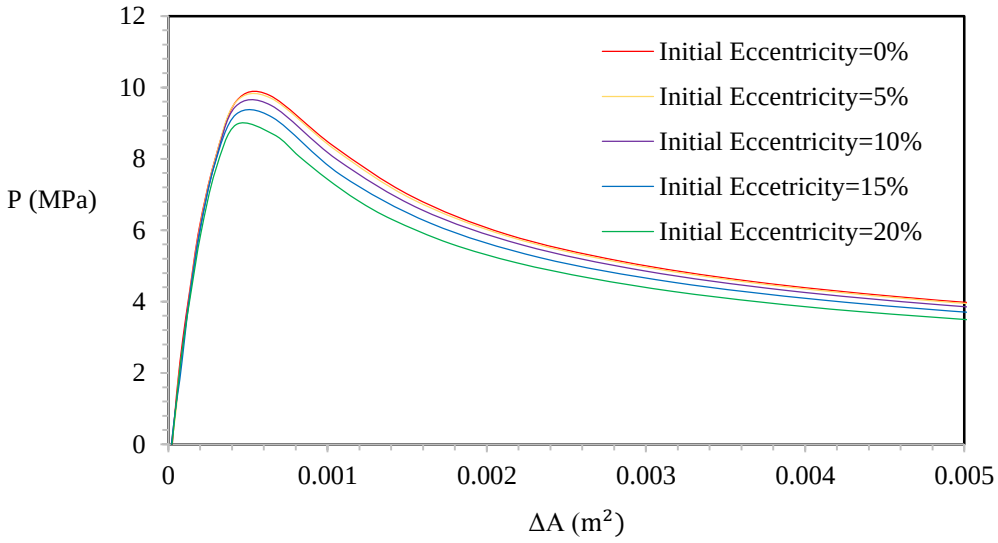

Fig. 2.40 Pressure versus change in area responses of initially ovalized rings for different values of initial eccentricity in Y direction (D/t=30, $\Delta_o = 1.6\%$).

The calculated collapse pressure for every imperfection pair of **Table 2.6** is plotted against initial ovality to obtain the corresponding curves of different initial eccentricities. Also, the normalized collapse pressure by the yield pressure is plotted against initial ovality, and the responses are presented in **Fig. 2.41** and **Fig. 2.42** for D/t=20 and D/t=30 respectively. It can be seen for both geometries that with the increasement of initial ovality imperfection, the collapse pressure drops significantly for all the cases of initial eccentricity. Furthermore, it can be observed from both figures that as the initial eccentricity is getting smaller, the curves become a little steeper, and thus it can be interpreted that the pressure drop rises too. In the case of D/t=20 (**Fig. 2.41**), it can be calculated from **Table 2.6** that the pressure drop is 20.11 MPa for $\Xi_o = 5\%$ and 17.73 MPa for $\Xi_o = 20\%$. Also, in the case of D/t=30 (**Fig. 2.42**), it can be calculated from **Table 2.6** that the pressure drop is 7.05 MPa for $\Xi_o = 5\%$ and 6.48 MPa for $\Xi_o = 20\%$. The calculated pressure drops show that the ovality effects are pronounced when eccentricity imperfections are weak. This conclusion agrees with the corresponding collapse modes of section 2.4.2. Also, it is worth mentioning that the observations made here are in fair agreement with those mentioned in [18].

Using the tabulated results of **Table 2.6**, the collapse pressure for every imperfection combination is plotted against initial eccentricity and the corresponding plots are presented in **Fig. 2.43** and **Fig. 2.44** for D/t=20 and D/t=30 respectively. The collapse pressure is normalized by the yield pressure and is plotted against initial eccentricity, as is shown in **Fig. 2.43** and **Fig. 2.44**. As the thickness eccentricity rises, a significant drop in the collapse pressure is observed for both cases of induced initial ovality. It can be observed that the drop in pressure rises when it comes to the case of small ovality and thus the pressure drop is high. This will be verified through **Table 2.6**. In the case of D/t=20 (**Fig. 2.43**), the pressure drop is 4.29 MPa for $\Delta_o = 0.05\%$ and 1.82 MPa for $\Delta_o = 1.6\%$. Also, in the case of D/t=30 (**Fig. 2.44**) the pressure drop is 1.51 MPa for $\Delta_o = 0.05\%$ and 0.82 MPa for $\Delta_o = 1.6\%$. The results imply that the influence of eccentricity is stronger in the cases of small ovality, which is a conclusion that agrees with the obtained collapse modes of section 2.4.2 and the observations of [18].

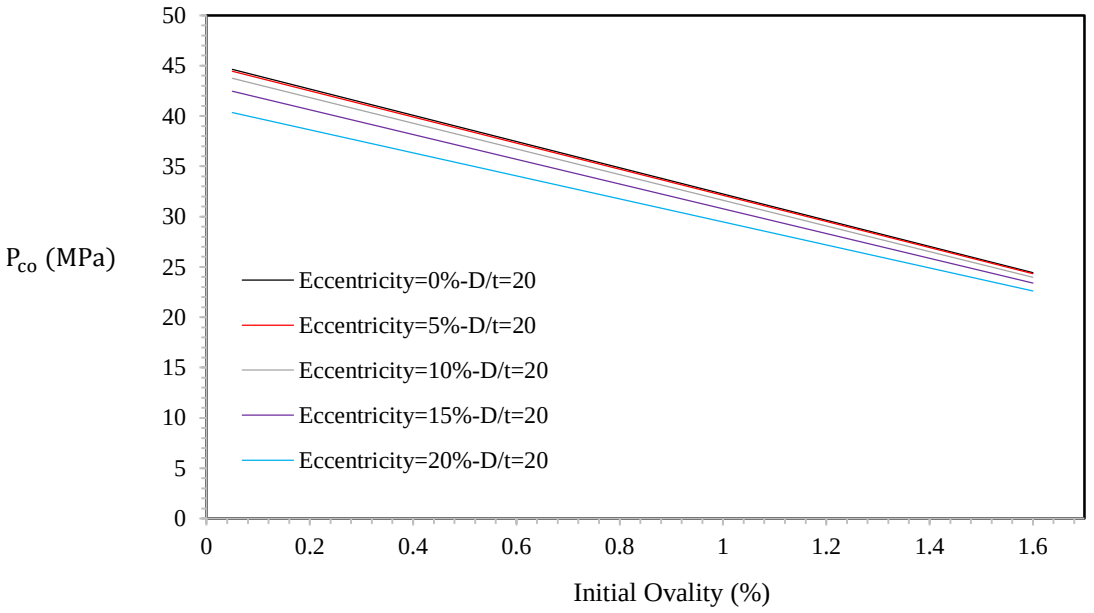

(a)

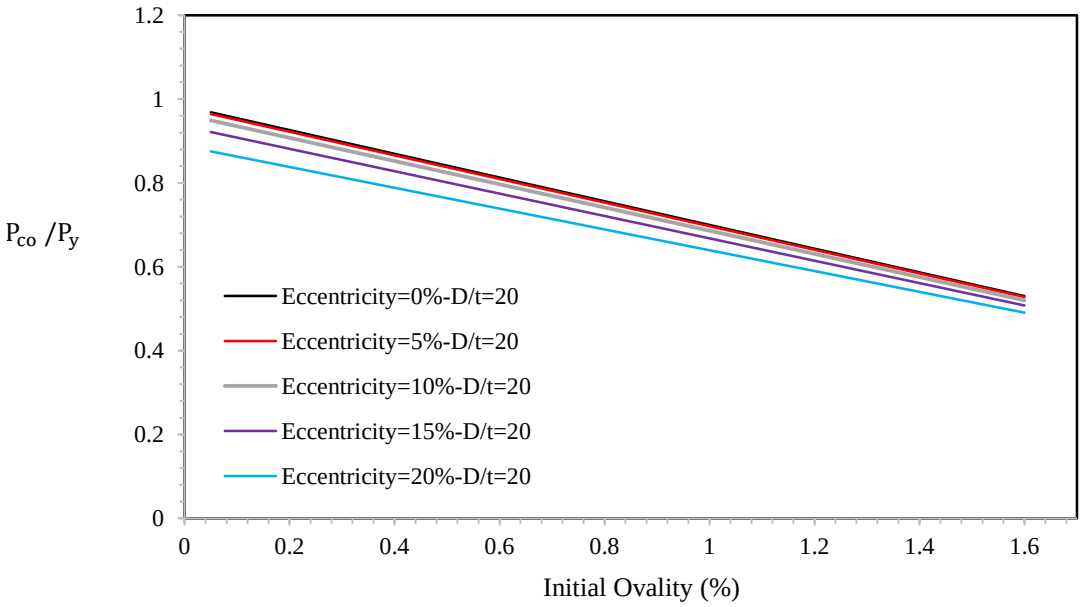

(b)

Fig. 2.41 The variation of collapse and normalized pressure with initial ovality for the ring of D/t=20.

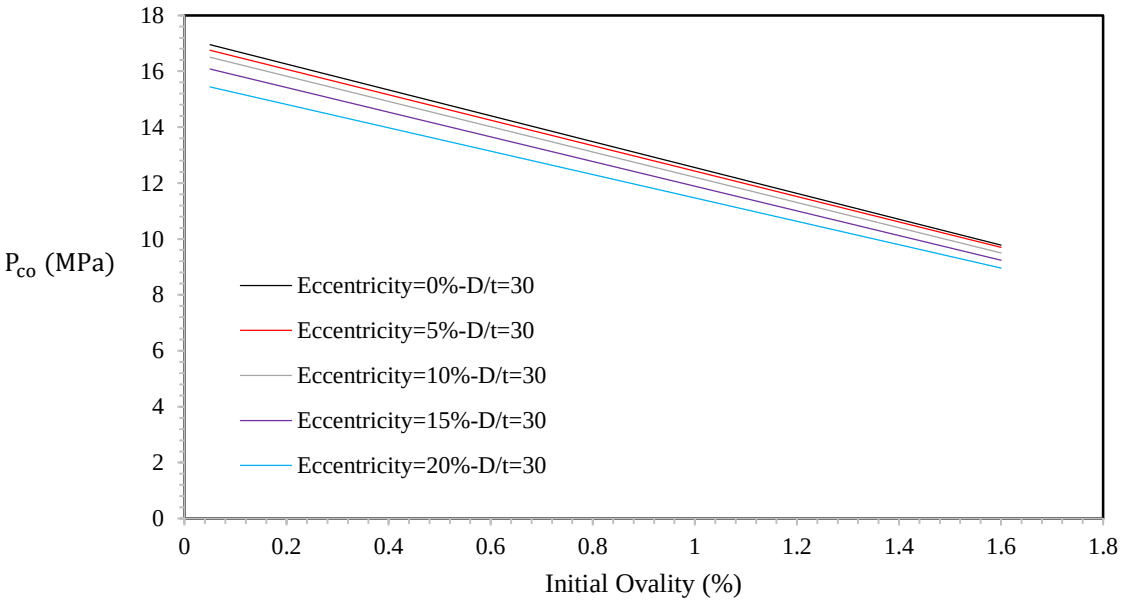

(a)

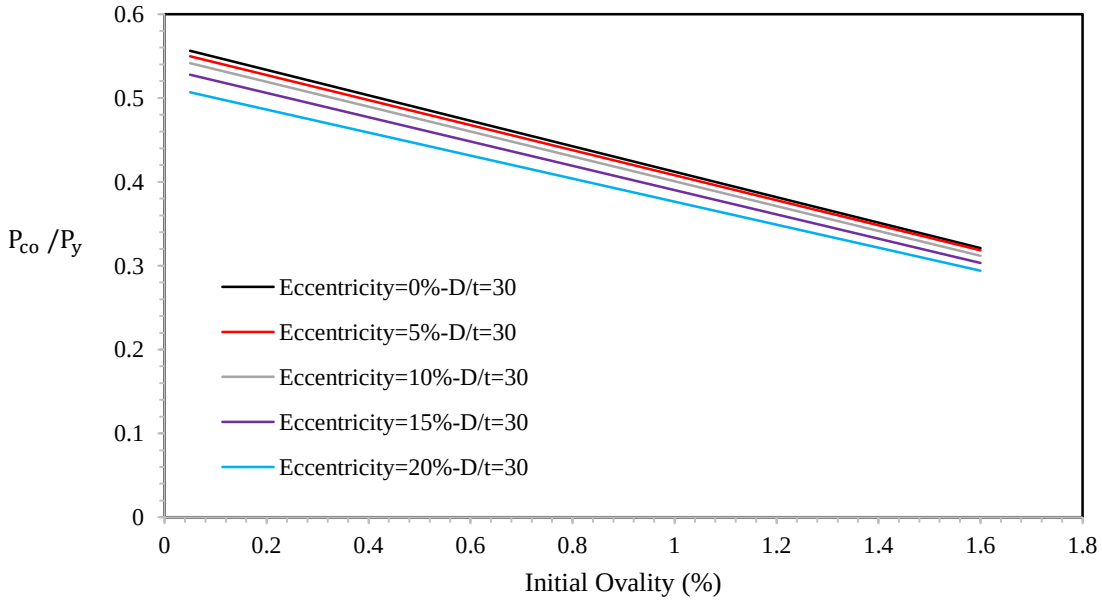

(b)

Fig. 2.42 The variation of collapse and normalized pressure with initial ovality for the ring of D/t=30.

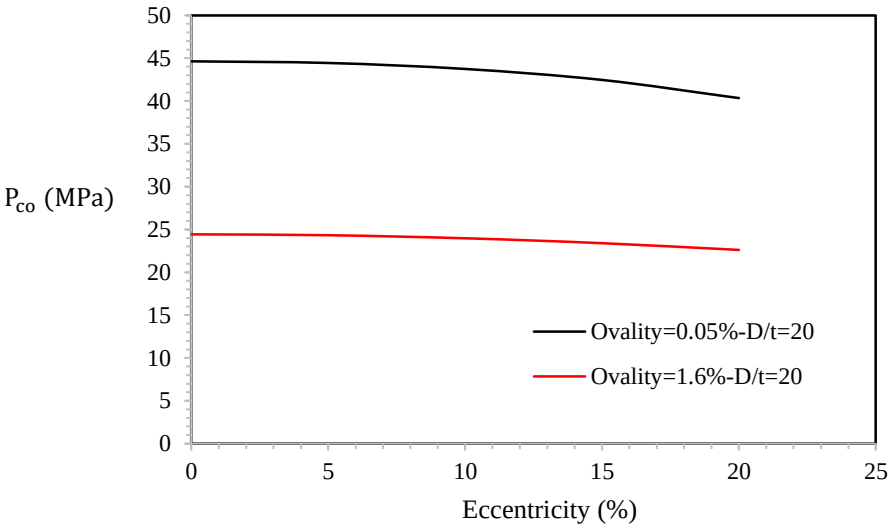

(a)

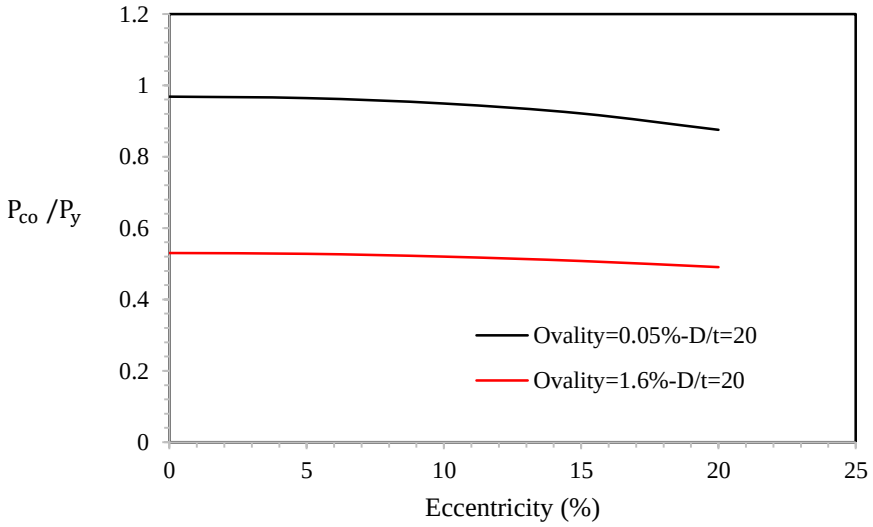

(b)

Fig. 2.43 The variation of collapse and normalized pressure with initial eccentricity for the ring of D/t=20.

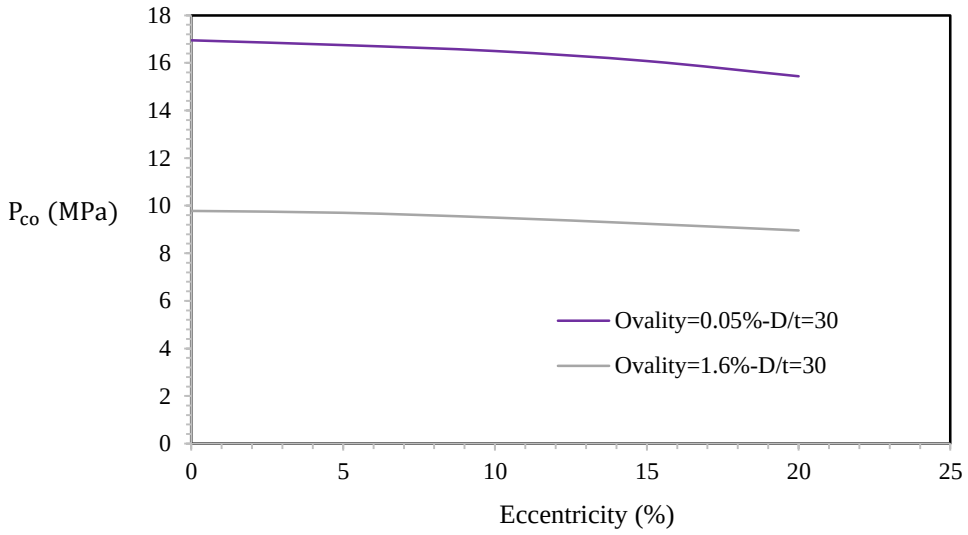

(a)

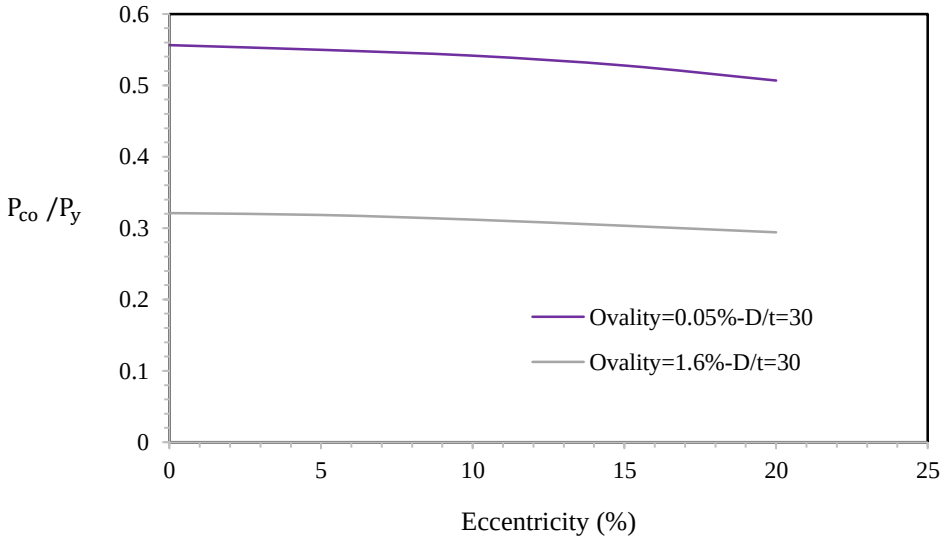

(b)

Fig. 2.44 The variation of collapse and normalized pressure with initial eccentricity for the ring of D/t=30.

2.5.3 Diameter-to-thickness ratio (D/t)

Diameter-to-thickness ratio is a parameter that affects the collapse pressure of a ring. The influence of this parameter was mentioned in **Fig. 2.38**, where it was observed that for higher values of D/t the collapse pressure was less sensitive to initial imperfections in the form of ovality. The collapse pressure values of **Table 2.5** are plotted against D/t to obtain the corresponding curves of various initial ovalities (**Fig. 2.45**). The significant drop in pressure can be observed for all the constant ovality curves. More specifically, the pressure drop is more pronounced as the D/t is getting lower. The influence of D/t parameter will also be investigated for the cases of initially ovalized rings with thickness eccentricity in Y direction (Section 2.5.2). The collapse pressure values of **Table 2.6** are plotted against D/t, and the corresponding curves of various eccentricities are presented in **Fig. 2.46** and **Fig. 2.47** for the rings with $\Delta_o = 0.05\%$ and $\Delta_o = 1.6\,\%$ respectively. From the figures and the tabulated results of **Table 2.6** it can be interpreted that the influence of initial eccentricity is getting weaker as the D/t rises. Similar observations were made in a plot of [22] for a variety of thickness eccentricity values and zero ovality.

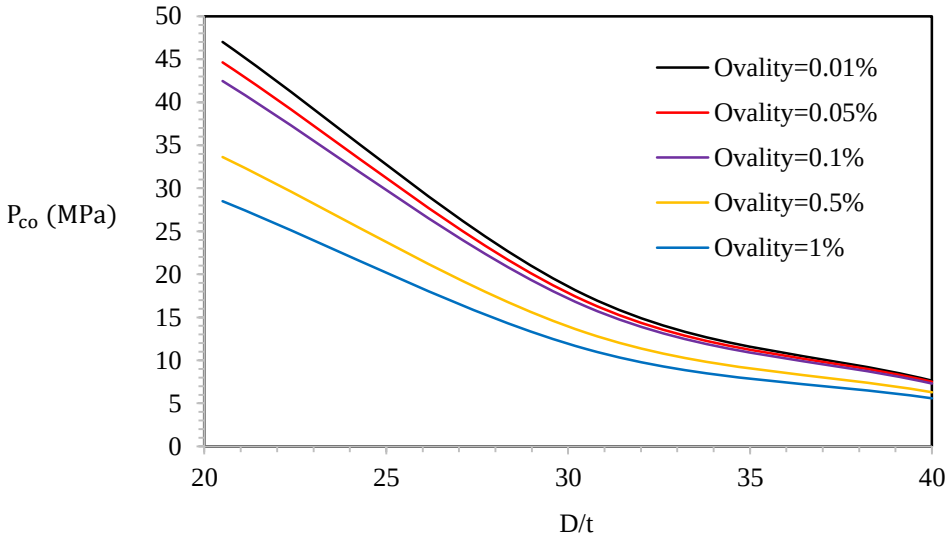

Fig. 2.45 Collapse pressure versus D/t for various values of initial ovality.

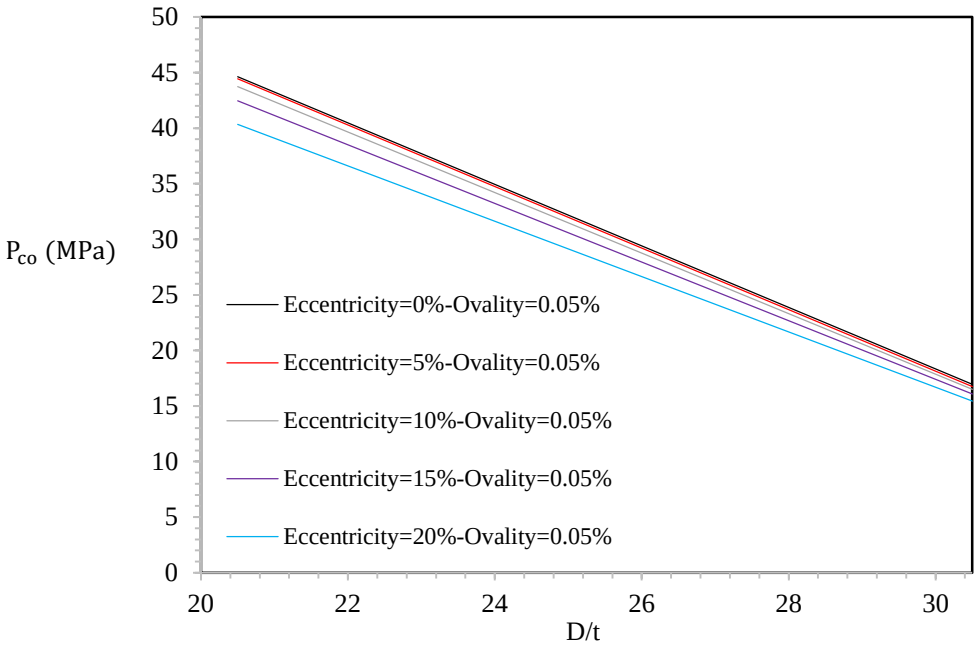

Fig. 2.46 Collapse pressure versus D/t for various values of initial eccentricity ($\Delta_o = 0.05\%$).

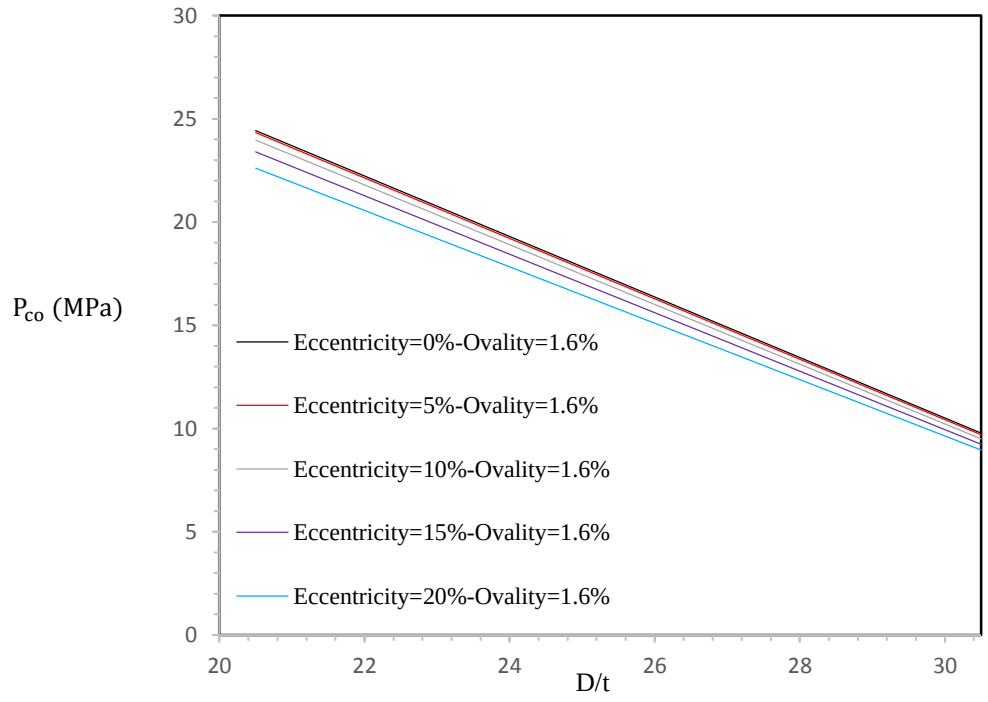

Fig. 2.47 Collapse pressure versus D/t for various values of initial eccentricity ($\Delta_o = 1.6\ \%$).

2.5.4 Material Anisotropy

The fabrication process of tubes and pipes induce anisotropic properties in the manufactured material, and they remain present in the finished product. A common type of anisotropic material properties of the finished pipe product is in the form of anisotropic yielding. For instance, in seamless pipes a difference between the yield stress in the circumferential ($\sigma_{y,T}$) and axial ($\sigma_{y,Z}$) directions always exists. The examination of anisotropy in seamless pipes will be examined under the Hill criterion of anisotropy [23]. Hill-type anisotropy is described by a yield function *f*, which can be expressed in a cylindrical coordinate system (R, T, Z) as follows [1]

$$f = \sqrt{\sigma_Z{}^2 - \left(1 + \frac{1}{S_T{}^2} - \frac{1}{S_R{}^2}\right)\sigma_Z\sigma_T + \frac{1}{S_T{}^2}\sigma_T{}^2 + \frac{1}{S_{ZT}{}^2}\sigma_{ZT}{}^2} \tag{2.10}$$

where $S_T = {}^{\sigma_{y,T}}/_{\sigma_{y,Z}}$, $S_R = {}^{\sigma_{y,R}}/_{\sigma_{y,Z}}$, $S_{ZT} = {}^{\sigma_{y,ZT}}/_{\sigma_{y,Z}}$. The notations $\sigma_{y,R}$, $\sigma_{y,T}$ and $\sigma_{y,Z}$ stand for the yield stresses in radial (R), transverse (T) and longitudinal (Z), whereas $\sigma_{y,ZT}$ denotes the yield stress under pure shear loading conditions. The S_T, S_R, S_{ZT} parameters express the variation of yield stress in the corresponding directions where they are referred to. Apparently, these variations are diminished when the parameters are equal to unity. The effect of anisotropy on the collapse pressure of pipes is examined by creating three-dimensional rings in the ABAQUS standard numerical framework. The models are created under the assumption that $S_R = S_T = S$ and $S_{ZT} = 1$, and thus (2.10) is rearranged as follows

$$f = \sqrt{\sigma_Z{}^2 - \sigma_Z\sigma_T + \frac{1}{S^2}\sigma_T{}^2} \tag{2.11}$$

2.5.4.1 Numerical modeling

Three-dimensional rings of six different D/t values are considered for the examination of anisotropic yielding in pipes. The cross-sectional geometric characteristics of rings are presented in **Table 2.7**. Three-dimensional rings are created with a longitudinal length of L=10mm. An initial ovality value of 0.2% is assigned to the models by following the procedure described in section 2.3.1 for two dimensional ovalized rings. Here, the initially ovalized cross-section of each ring is considered to be located at the axes origin (Z=0), whereas the cross-section of Z=10 mm is made to be circular. Due to the symmetries of the problem (Section 2.3), three-dimensional quadrant ring models are considered for the analyses. The Cartesian coordinate system (X, Y, Z) is chosen for the application of

boundary conditions. All the rings are discretized by 20-node quadratic brick elements of reduced integration (C3D20R). The circumferential direction of the models consists of 50 elements, the through-thickness direction consists of 8 elements and the longitudinal direction consists of one element. Therefore, the model is discretized by a total number of 400 elements as shown in **Fig. 2.48**. The boundary nodes at the cross sections of planes Z=0 and Z=10 mm, are constrained with the «ZSYMM» boundary condition option, and thus their nodes are prescribed to have zero displacements in Z direction and zero rotations about the X and Y axes. Furthermore, «XSYMM» boundary conditions are applied at the top side of the model along Z direction to constrain the node displacements X direction, and node rotations about the Y and Z axes. Also, the «YSYMM» boundary condition is assigned to the boundary nodes of the bottom side to constrain the node displacements in Y direction, and node rotations about the X and Z axes.

The elastic-plastic material properties of steel grade X65 (**Table 2.2**) are used in the numerical analyses of rings. The anisotropy is assigned following the Hill criterion as described by (2.11). A polar cylindrical coordinate system is defined in ABAQUS numerical framework for the application of anisotropic material properties, and material orientation is considered in the numerical modeling as well. The analysis is developed through two incremental steps in a similar way as described in section 2.3. The Riks' continuation algorithm that is implemented in ABAQUS software is used for the incremental calculation of the collapse pressure.

Table 2.7 Geometric parameters in terms of outer diameter D and thickness t for different D/t ratios.

D/t	D (mm)	t (mm)
40	600	15
35	600	17.14
30	610	20
25	410	16.4
20	410	20
15	410	27.3

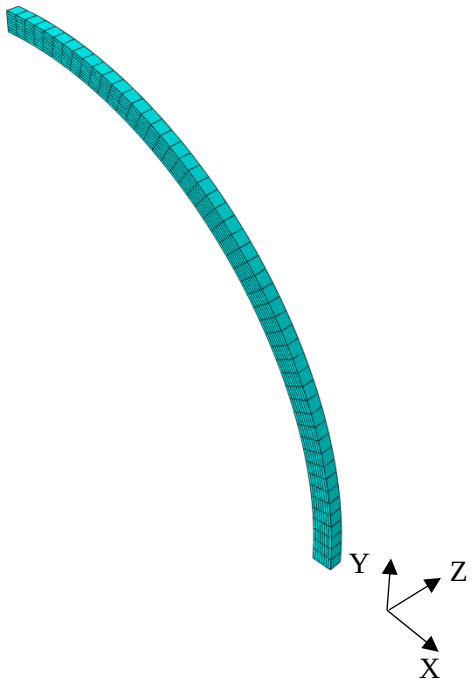

Fig. 2.48 Finite element mesh of the three-dimensional ring of D/t=40 and L=10mm. The depicted mesh is assembled by quadratic elements of reduced integration C3D20R.

2.5.4.2 Numerical results

Following the numerical modeling of the previous section, six different values of the parameter S ($S = {}^{\sigma_{y,T}}/_{\sigma_{y,Z}}$) are assigned to every D/t ring to study the anisotropic yielding of rings. More specifically, the variable S is selected to vary between the range of 0.85 to 1.1, by six prescribed values: S=0.85, 0.90, 0.95, 1, 1.05, 1.1. The calculated collapse pressures of D/t's for every value of S, are normalized by the corresponding value of collapse pressure in the absence of anisotropy (S=1), and the results are plotted against the considered values of variable S and D/t's, as shown in **Fig. 2.49** and **Fig. 2.50** respectively. Clearly, the results show that the effect of anisotropy on the collapse pressure, diminishes for higher D/t rings. On the other hand, the anisotropic yielding detrimental effects are pronounced for lower D/t rings. The presented results here are in fair agreement with those presented in previous works [1], [20], [22], [24] but a straight comparison of the results is not possible due to the differences in material and numerical modeling.

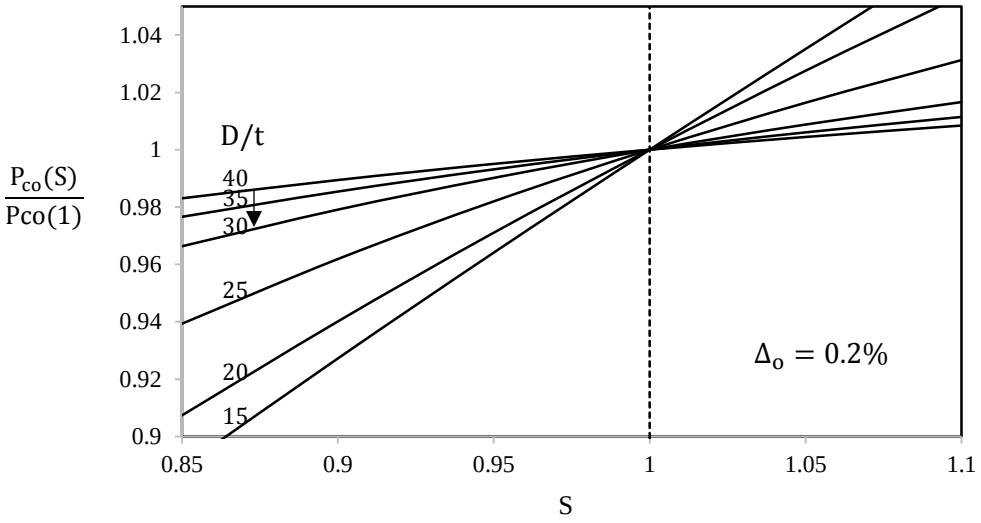

Fig. 2.49 The variation of collapse pressure in the presence of anisotropy with parameter S for a variety of D/t rings.

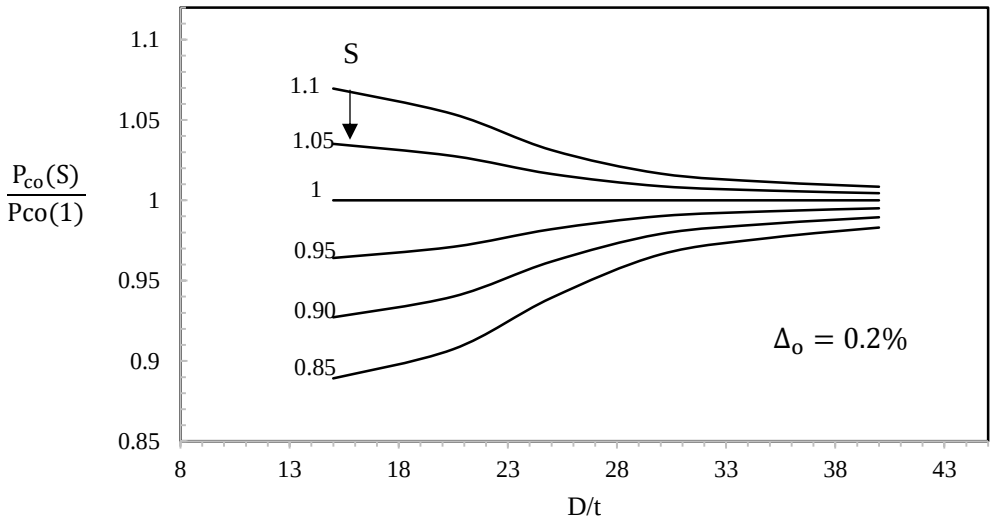

Fig. 2.50 The variation of collapse pressure in the presence of anisotropy with D/t for different values of parameter S in the range of 0.85 to 1.1.

2.5.5 Residual Stresses

The fabrication process of tubes and pipes induce residual stress fields in the finished product of a cold forming process. The residual stress fields affect the mechanical properties of the formed products, and they subsequently affect the collapse performance of a tube under uniform external pressure loading conditions. For the determination of the residual stress field amplitudes in the formed products, pipe ring splitting tests are conducted as presented in [1]. In this section, the effect of residual stresses on the collapse pressure of rings will be examined numerically within the ABAQUS numerical framework.

The three-dimensional ring of D/t=30 (**Table 2.7**) is selected to examine the effects of residual stresses on the collapse pressure. The numerical modeling procedure, included the amplitude of initial ovality and the application of boundary conditions, is the same as that followed in section 2.5.4.1. The only difference here exists in the number of finite elements used in the through-thickness direction; 9 elements used in Y direction. Therefore, the ring totally consists of 450 quadratic elements of reduced integration (C3D20R). The residual stresses are assigned in the finite element model as a linear stress distribution through the pipe wall thickness. This procedure is also adopted in previous works [20], [25] . **Fig. 2.51** represents schematically the circumferential residual stress distribution through the ring wall thickness, where the residual stress value is σ_R on the outer ring surface and $-\sigma_R$ on the inner ring surface. A parameter $R = {}^{\sigma_R}/_{\sigma_y}$ is introduced, and it is decided to vary in the range of 0.1 to 0.9; R=0.1, 0.2, 0.3, 0.4, 0.5, 0.6, 0.7, 0.8, 0.9. The different values of R are induced into the finite element model. The calculated collapse pressures for every value of R, are normalized by the corresponding value of collapse pressure for $\sigma_R = 0$,and the results are plotted against the examined values of variable R, as shown in **Fig. 2.52**. As it was expected, the collapse pressure of the same ring is getting lower as long as the residual stress parameter R increases. The results here, are in agreement with the results of previous works [1], [20], [22], [25] on the same subject for a variety of D/t values.

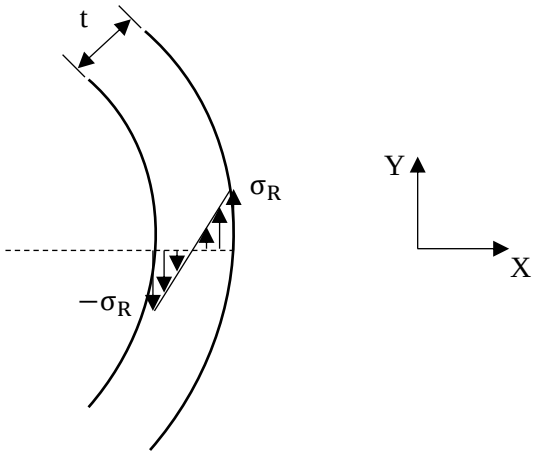

Fig. 2.51 Schematic representation of the circumferential residual stress distribution for the finite element model of D/t=30.

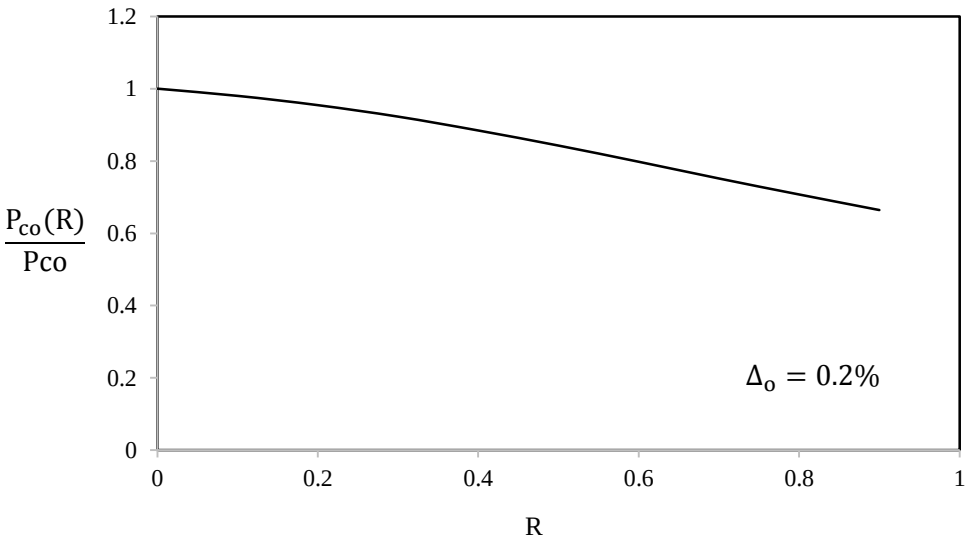

Fig. 2.52 The variation of collapse pressure in the presence of residual stress field with parameter R for the ring of D/t=30.

2.6 Elastic-Inelastic ring mechanical behavior

The collapse responses of the rings examined in section 2.5.1, where expressed by the pressure-ovality and the pressure-change in area variations. These numerical responses will be compared with analytical solutions of pre-buckling and post-buckling analysis of chapter 1. Firstly, P in (1.41) will be expressed in terms of an arbitrary variable ξ as follows

$$P = 2\,\sigma_y{}^*(\frac{t}{D_m})^2\frac{1}{\xi} \tag{2.12}$$

The lengths γ and β of the deformed configuration of **Fig. 1.9** can also be expressed as a function of variable ξ, and the formulas are presented below

$$\begin{aligned}\gamma &= R_m\sqrt{1-\xi}\\ \beta &= R_m\sqrt{1+\xi}\end{aligned} \tag{2.13}$$

Therefore, the change in area between the two configurations is

$$\Delta A = \frac{R_m{}^2 - R_m{}^2\sqrt{1-\xi^2}}{2} \tag{2.14}$$

The ovality of the ring's cross section is expressed by (2.2), and using the above simplified plastic model it is obvious that $D_{min} = 2R_{in}\sqrt{1-\xi}$ and $D_{max} = 2R_{in}\sqrt{1+\xi}$. The substitution of D_{min} and D_{max} in (2.2) gives the relation of ξ with ovality, Δ, as follows

$$\xi = \frac{2\Delta}{1+\Delta^2} \tag{2.15}$$

The substitution of (2.15) to (2.12) will give the expression of P in terms of ovality, and the result is presented below

$$P = 2\,\sigma_y{}^*(\frac{t}{D_m})^2\,\frac{1+\Delta^2}{2\Delta} \tag{2.16}$$

Solving (2.14) for ξ and substituting to (2.12) results in

$$P = 2\,\sigma_y{}^*(\frac{t}{D_m})^2\frac{1}{\sqrt{1-\left(1-\frac{2\Delta A}{R_m{}^2}\right)^2}} \tag{2.17}$$

The analytical expression (2.17) describes the post-buckling area reduction upon application of external pressure. The initial shape of the cross-sectional area is assumed to be circular in (2.17). Prior to buckling, the change in area enclosed by the ring upon application of external pressure is described by (1.36), and thus the corresponding area at the buckling stage, ΔA_{cr}, can be calculated by (1.39). Therefore, ΔA_{cr} can be considered in (2.17) as follows

$$P = 2\,\sigma_y{}^*\left(\frac{t}{D_m}\right)^2 \frac{1}{\sqrt{1-\left(1-\frac{2(\Delta A-\Delta A_{cr})}{{R_m}^2}\right)^2}} \tag{2.18}$$

Material changes will be made for the 2D ring of D/t=40 (**Table 2.3**), which has initial imperfections in the form of ovality. Therefore, the initial ovality values of $\Delta_o = 0.01\%, 0.05\%, 0.1\%, 0.5\%$ and 1% will be induced in the ring of such geometry. Thus, five elastic models are created in ABAQUS standard by following the numerical modeling procedure of section 2.3.1. The elastic material properties are E=210000 MPa and ν=0.3. The numerical results will be compared with the analytical solutions of chapter 1. **Fig. 2.53** shows the influence of initial ovality on the pre-buckling and post-buckling responses. The analytical post-buckling curve (1.37) of the perfect ring case is included in the same plot. While the initial imperfection value rises, the deviation of collapse pressure from that of the perfect case rises too and thus, the ring "softens" and collapses at lower pressures. The same observations can be made from **Fig. 2.54**, where the variation of pressure with the reduction in the enclosed area is presented. In this figure both the pre-buckling (1.36) and post-buckling (1.38) responses are included for comparison with the curves of the numerical results. Minor changes are observed in the pre-buckling region. The post-buckling responses are like those of **Fig. 2.53** and thus, similar observations are made. Prior to buckling, the cross-sectional deformation of imperfect rings is described by (1.22). Equation (1.22) can be expressed in terms of maximum displacement, w_{max} and initial ovality Δ_o for a ring of mean radius R_m as follows

$$P/P_{cr} = 1 - \frac{\Delta_o}{\left(w_{max}/R_m\right)} \tag{2.19}$$

The responses of pressure versus maximum displacement are shown in **Fig. 2.55** for the initial ovality values of $\Delta_o = 0.01\%, 0.05\%, 0.1\%, 0.5\%$ and 1% that were assigned into the ring of D/t=40. As mentioned in section 2.2, the variable of initial ovality is calculated from (2.4). The marked dots on the plot represent the results for the pressure of first yielding (P_f), which are calculated from (1.29) for the five values of initial ovality. Clearly, the results show that P_f is imperfection sensitive.

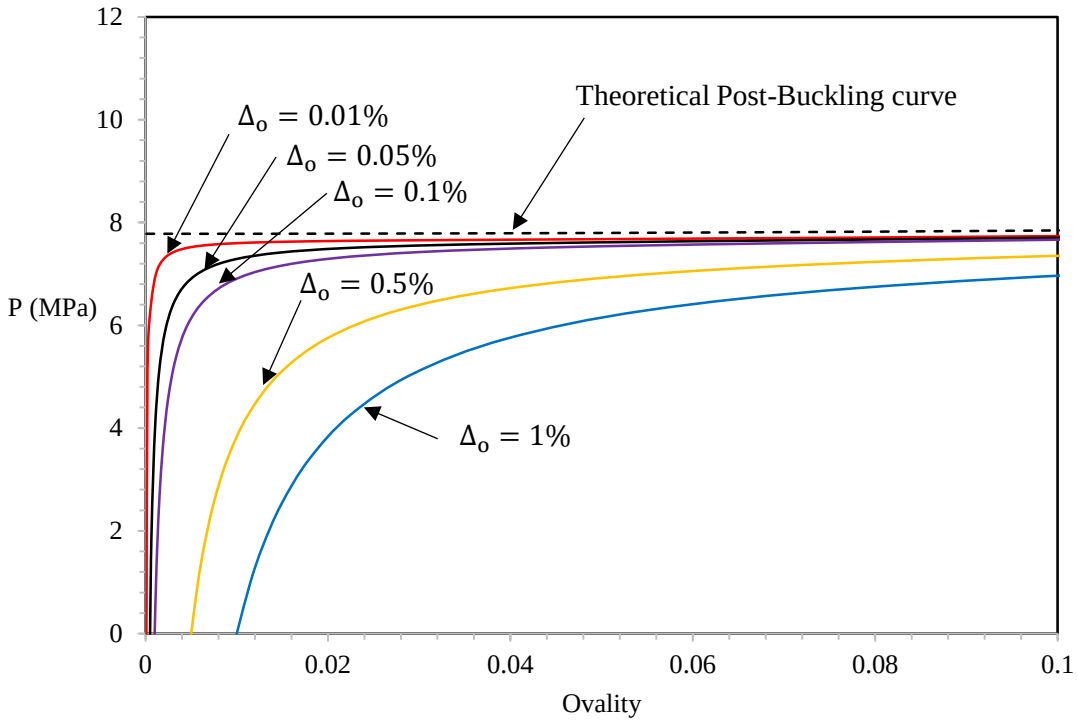

Fig. 2.53 Pressure-Ovality responses for elastic rings of various imperfection values and D/t=40.

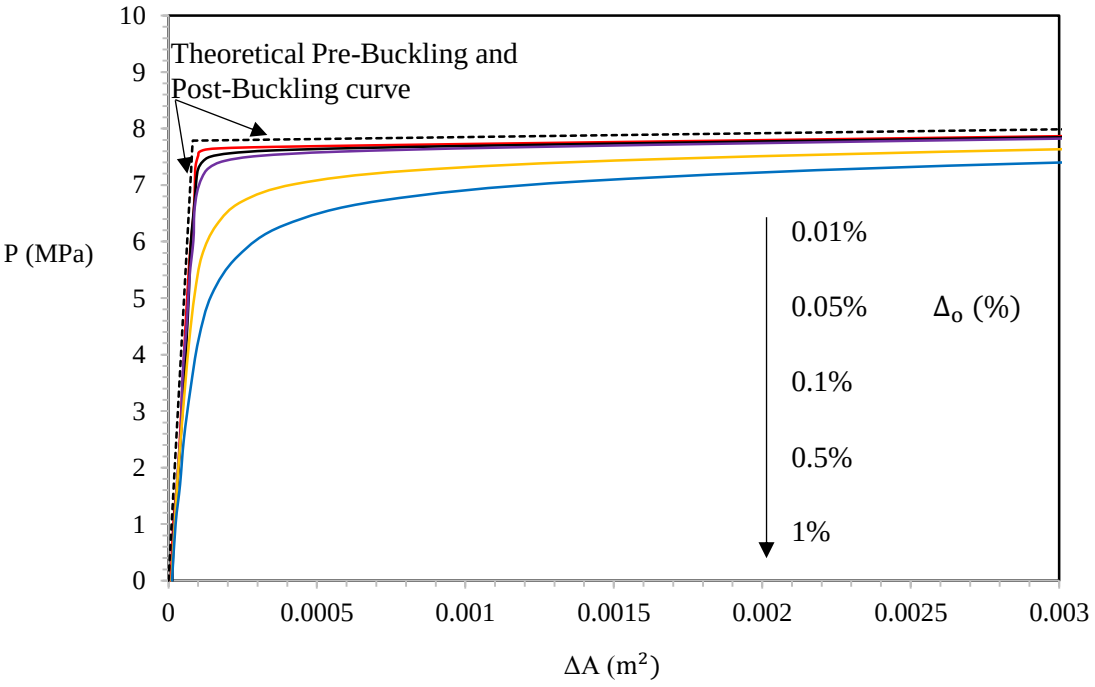

Fig. 2.54 Pressure versus the area change curves for elastic rings of various imperfection values and D/t=40.

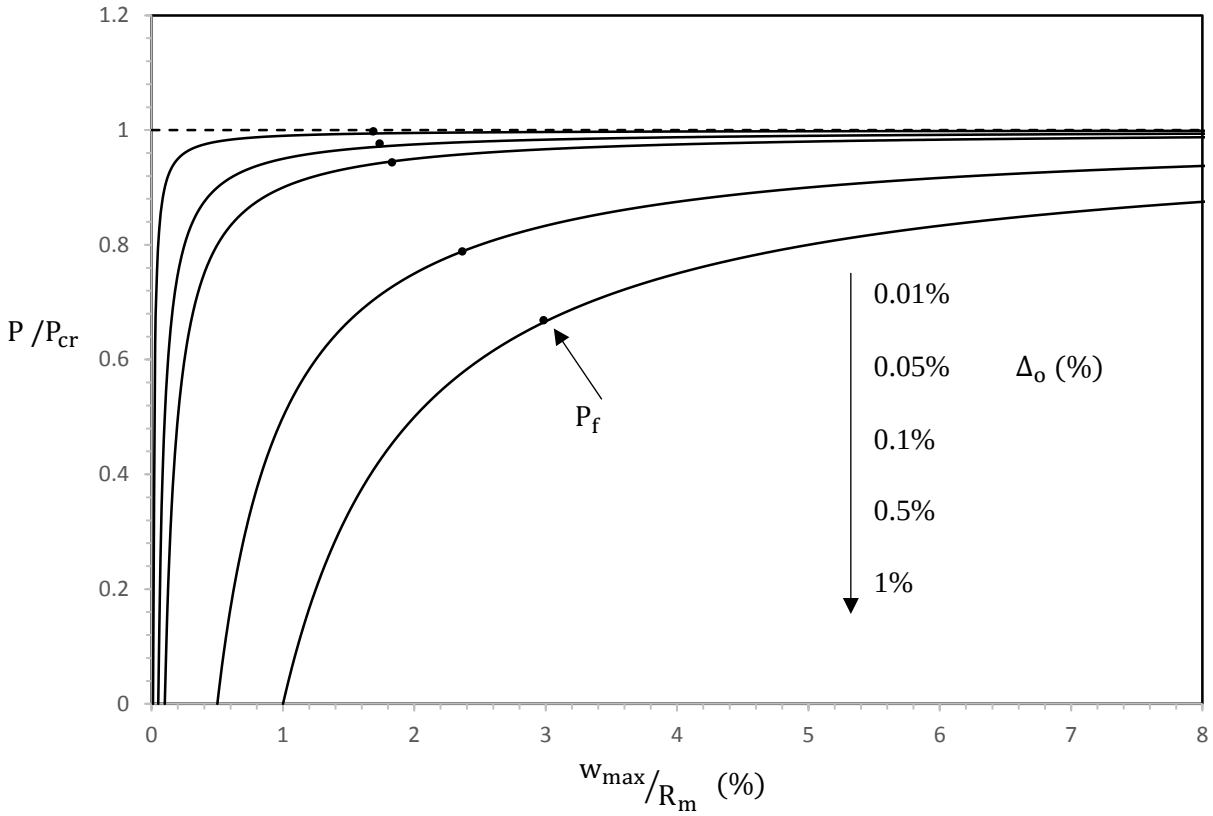

Fig. 2.55 Pressure-maximum displacement responses for various values of initial ovality (D/t=40). The solid dots correspond to the pressure of first yielding, calculated from (1.29).

The elastic pressure-ovality responses, presented above for the ring of D/t=40, will be plotted in a common chart with the corresponding responses of the inelastic cases of section 2.5.1. **Fig. 2.56** shows the elastic and inelastic responses for the examined thin wall ring (D/t=40). This figure summarizes the differences between the elastic and inelastic cases. The elastic material responses bifurcates when a critical pressure value is reached, and the post-buckling response follow a positive slope pattern. On the contrary, the inelastic cases develop a limit point pressure, which is the maximum collapse capacity of the ring. As it was discussed in section 2.5.1, the collapse pressure is imperfection sensitive. Meanwhile, the equilibrium path of the plastic collapse mechanism (2.16) is included in the figure. The results are in agreement with theory and numerical results of previous projects [1], [4], [15]. The pressure versus change in area responses of elastic-inelastic rings are presented in **Fig. 2.57**. The behavior is similar with those of pressure versus ovality responses, and the post-buckling analytical expression (2.18) is plotted on the same figure for comparison.

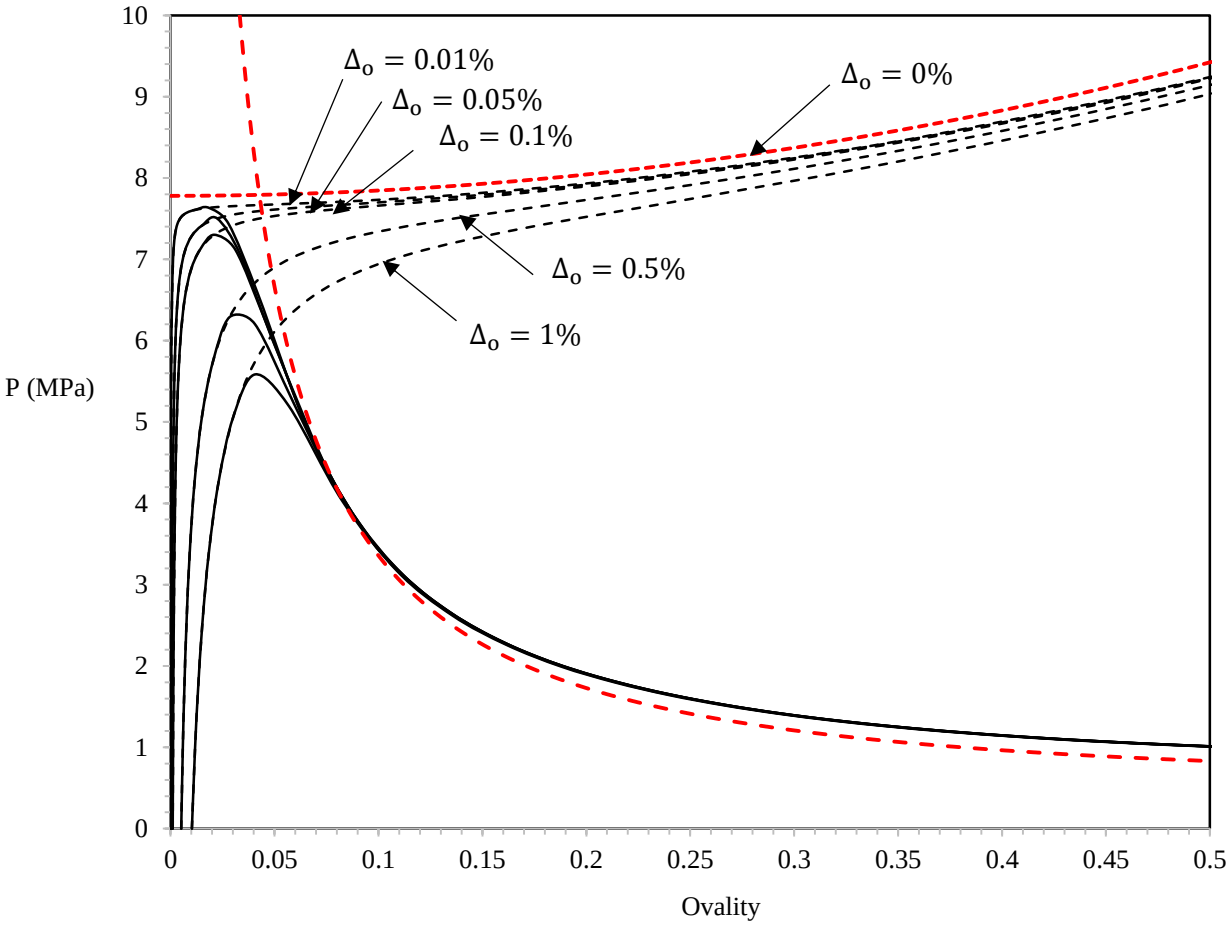

Fig. 2.56 Pressure-ovality responses in elastic and inelastic case of rings of various imperfection values (D/t=40).

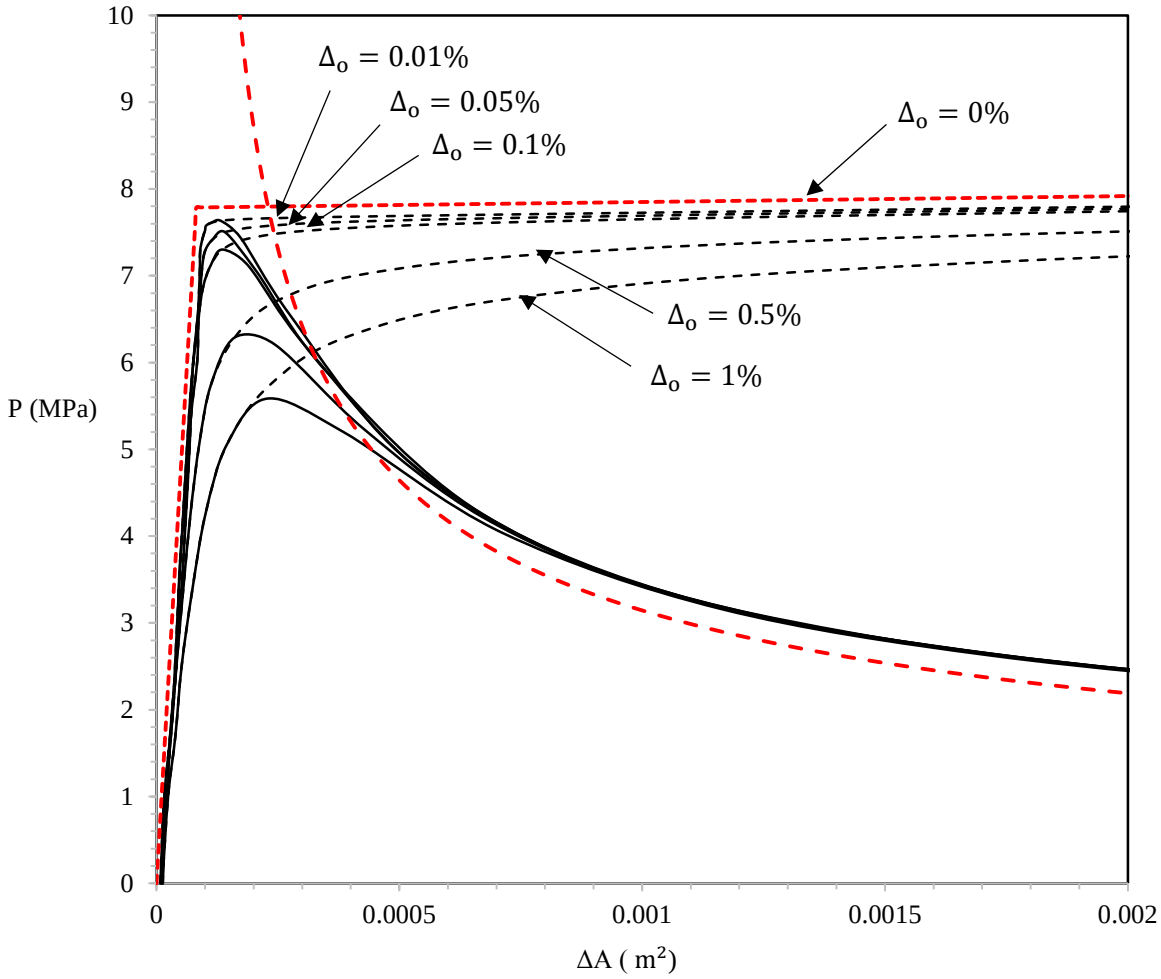

Fig. 2.57 Pressure-change in area responses in elastic and inelastic case of rings of various imperfection values (D/t=40).

2.6.1 Effect of finite element discretization on the mechanical behavior of elastic thin-walled 2D rings

The elastic ring of D/t=40 is considered with the initial ovality value of 0.01%. The model is discretized with four-node, full-integration plane-strain finite elements, which are defined as CPE4 in ABAQUS. The mesh density is the same as that used in the models of section 2.3.1. The pressure-ovality response, obtained by mesh discretization with CPE4 element type, is shown in **Fig. 2.58**. The post-buckling part of the response is initiated at a critical pressure, which is higher than that of the theoretical curve (1.37). Since the theoretical curve corresponds to the perfect ring case, and the critical pressure is imperfection sensitive, the post-buckling part of the examined response should have been similar to that observed in **Fig. 2.53** for CPE4R finite element type and $\Delta_o = 0.01\%$. Under the

same mesh density, the model is discretized using eight-node biquadratic plane strain finite elements of reduced and full integration, which are denoted in ABAQUS as CPE8R and CPE8 respectively. The corresponding pressure-ovality responses of CPE8R and CPE8 finite element discretization are shown in **Fig. 2.59** and **Fig. 2.60** respectively. The pressure-ovality response of both element types maintain a positive slope for pressures higher than the critical pressure which is lower than that of the analytical solution (1.37).

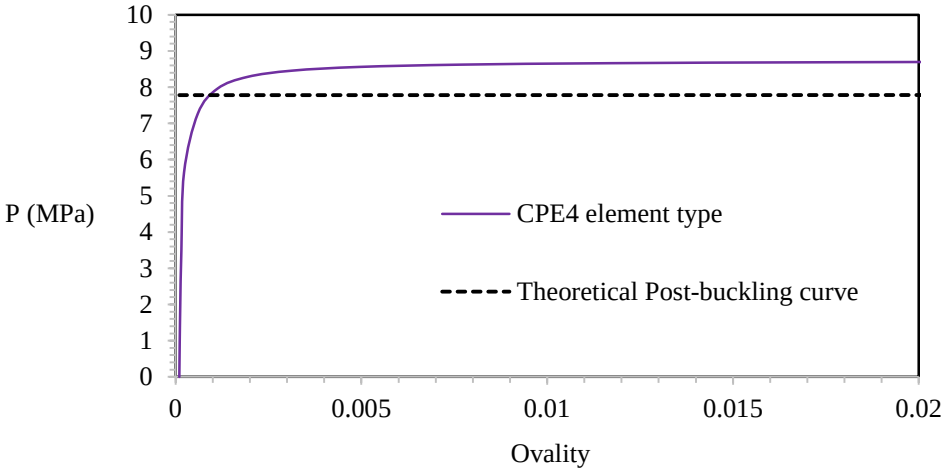

Fig. 2.58 Pressure-ovality response of CPE4 finite element type for the elastic ring of D/t=40 with initial ovality of $\Delta_o = 0.01\%$.

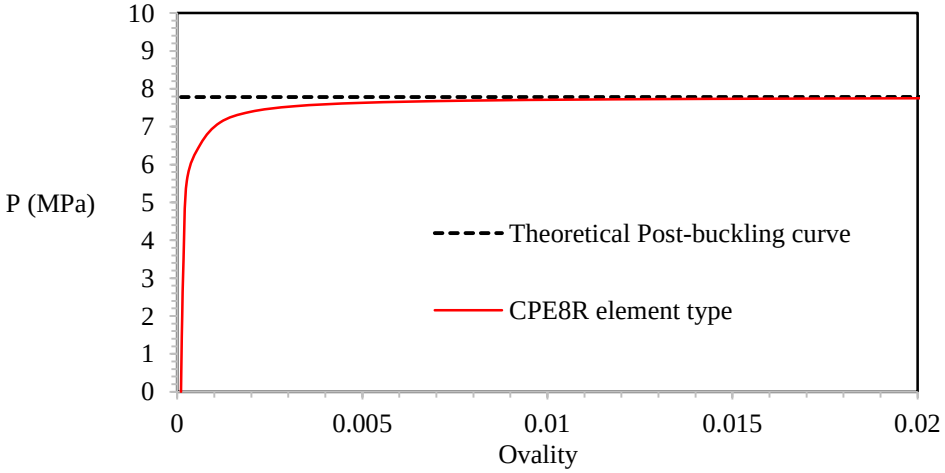

Fig. 2.59 Pressure-ovality response of CPE8R finite element type for the elastic ring of D/t=40 with initial ovality of $\Delta_o = 0.01\%$.

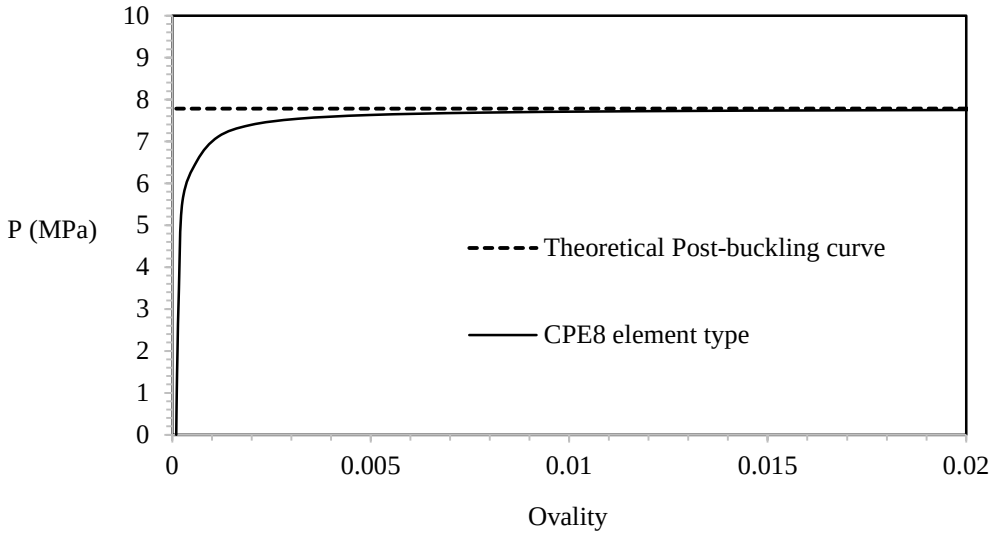

Fig. 2.60 Pressure-ovality response of CPE8 finite element type for the elastic ring of D/t=40 with initial ovality of $\Delta_o = 0.01\%$.

2.6.2 Effect of finite element discretization on the mechanical behavior of elastic thin-walled 3D rings

The ring of D/t=40, will be presented as a three-dimensional one with the cross-sectional geometry parameters of **Table 2.7** (the D/t=40 geometric parameters are shown in **Table 2.3** as well) and longitudinal length of L=10mm. The numerical modeling procedure including the application of boundary conditions on the model, the mesh density, and the number of incremental steps, is the same as that presented in section 2.5.4.1. Differences with respect to the finite element model of section 2.5.4.1 exist in the material, the finite element type, and the initial imperfection amplitude. The D/t ring is assigned an initial ovality of 0.01%, in a way similar to that described in section 2.5.4.1. The material of the ring is considered elastic, with modulus E=210 GPa and poisson ratio ν=0.3. The effect of finite element discretization on the mechanical response of ring upon application of external pressure, is studied by creating finite element models of constant mesh density and variable element type. More specifically the finite elements of **SC8R** (8-node quadrilateral in-plane general-purpose continuum shell elements of reduced integration), **S4R** (4-node doubly curved shell elements of reduced integration), **S4** (4-node doubly curved shell elements of full integration), **S8R** (8-node doubly curved thick shell elements of reduced integration), **C3D8R** (8-node linear brick elements of reduced integration), **C3D8** (8-node linear brick elements of full integration), **C3D20R** (20-node quadratic brick elements of reduced integration) and **C3D20** (20-node quadratic brick elements of full

integration), are considered in the finite element analyses. Therefore, eight finite element models of elastic material and D/t=40 are created in ABAQUS standard.

The equilibrium path of pressure versus the ovalization of the ring cross-section is created for every finite element type, and the responses are presented in **Fig. 2.61**- **Fig. 2.68**. The post-buckling analytical curve (1.37) is included in figures for comparison with the curves of the numerical results. Except from the response of C3D8 finite elements, the pressure-ovality responses of the rest element types buckle elastically at a critical pressure which is lower than that of the analytical solution. Thus, the post-buckling part of the pressure-ovality response, obtained from C3D8 finite elements, follows a positive slope which is higher than the analytical post-buckling curve. This post-buckling behavior is mentioned in section 2.6.1 for the same ring (2D ring of D/t=40) with initial ovality of 0.01%, when a mesh of CPE4 type of finite elements is used. Furthermore, the slopes of the post-buckling region for the responses of SC8R, C3D20R and C3D20 converge with the analytical curve as the cross-sectional ovalization rises. For the same range of ovalization values, the post-buckling responses obtained from the element types of S4R, S4, S8R and C3D8R develop a positive slope but they do not coincide with the analytical curve.

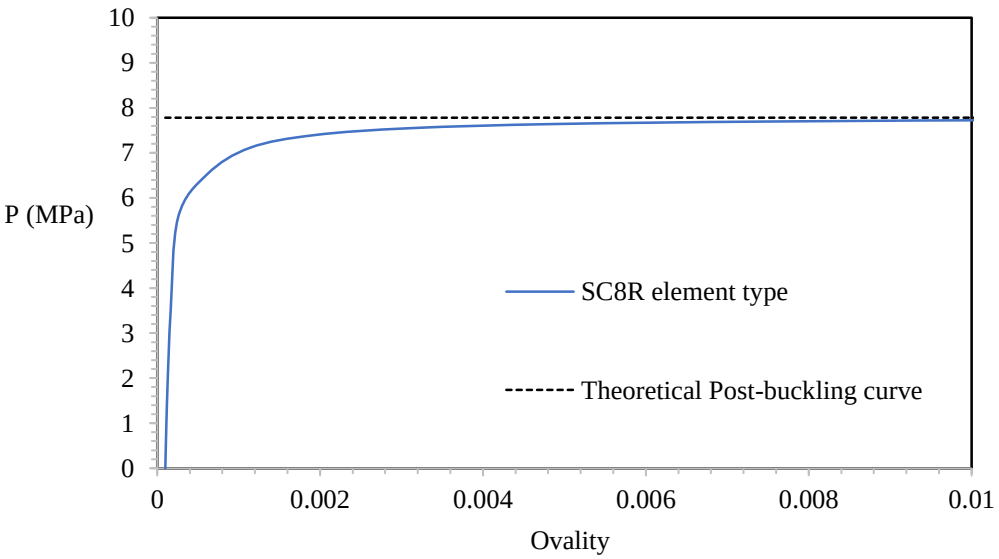

Fig. 2.61 Pressure-ovality response for mesh discretization with SC8R finite element type (3D elastic ring of D/t=40, L=10mm and $\Delta_o = 0.01\%$).

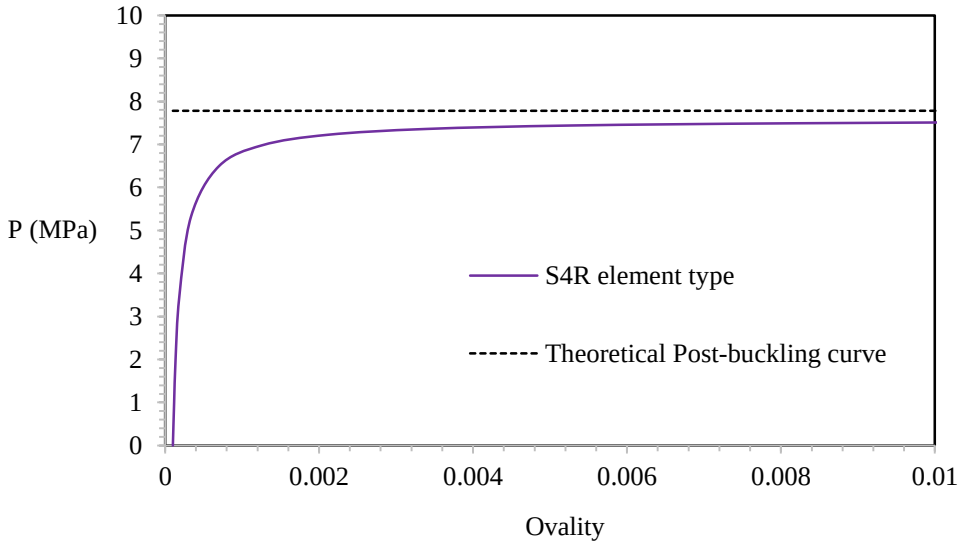

Fig. 2.62 Pressure-ovality response for mesh discretization with S4R finite element type (3D elastic ring of D/t=40, L=10mm and $\Delta_o = 0.01\%$).

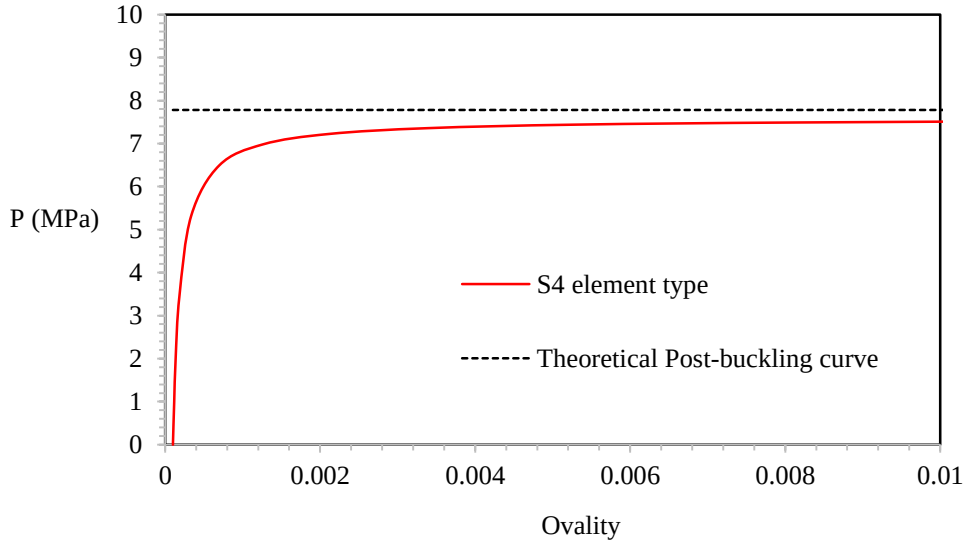

Fig. 2.63 Pressure-ovality response for mesh discretization with S4 finite element type (3D elastic ring of D/t=40, L=10mm and $\Delta_o = 0.01\%$).

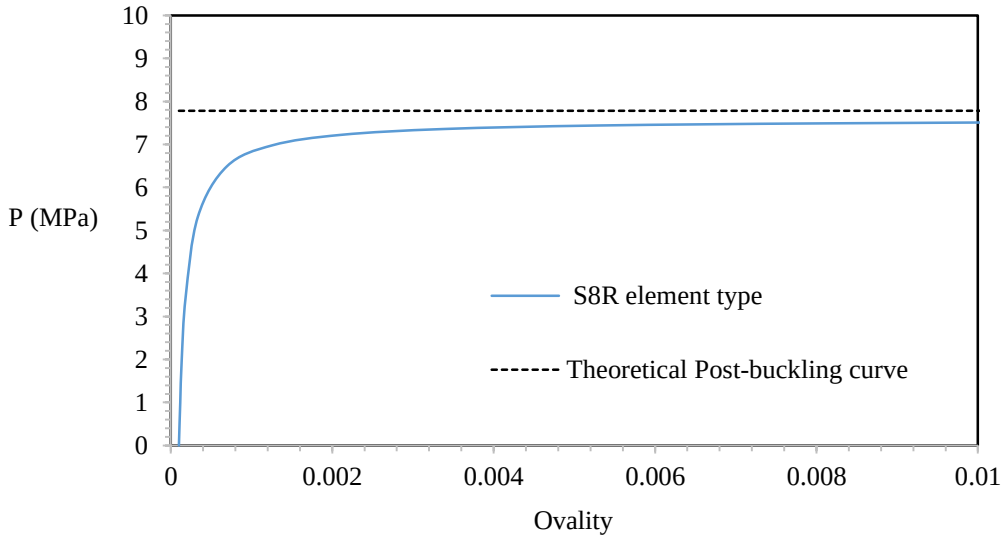

Fig. 2.64 Pressure-ovality response for mesh discretization with S8R finite element type (3D elastic ring of D/t=40, L=10mm and $\Delta_o = 0.01\%$).

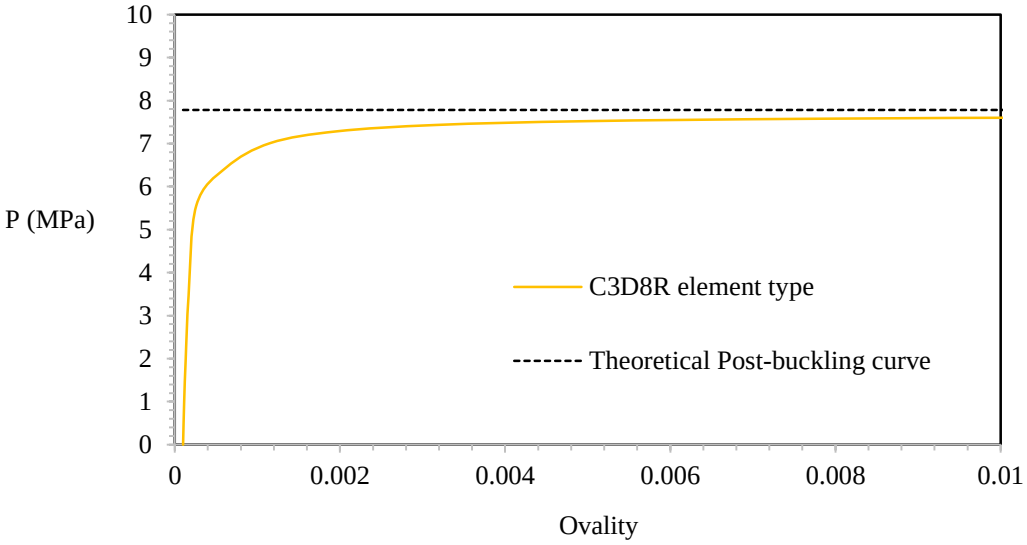

Fig. 2.65 Pressure-ovality response for mesh discretization with C3D8R finite element type (3D elastic ring of D/t=40, L=10mm and $\Delta_o = 0.01\%$).

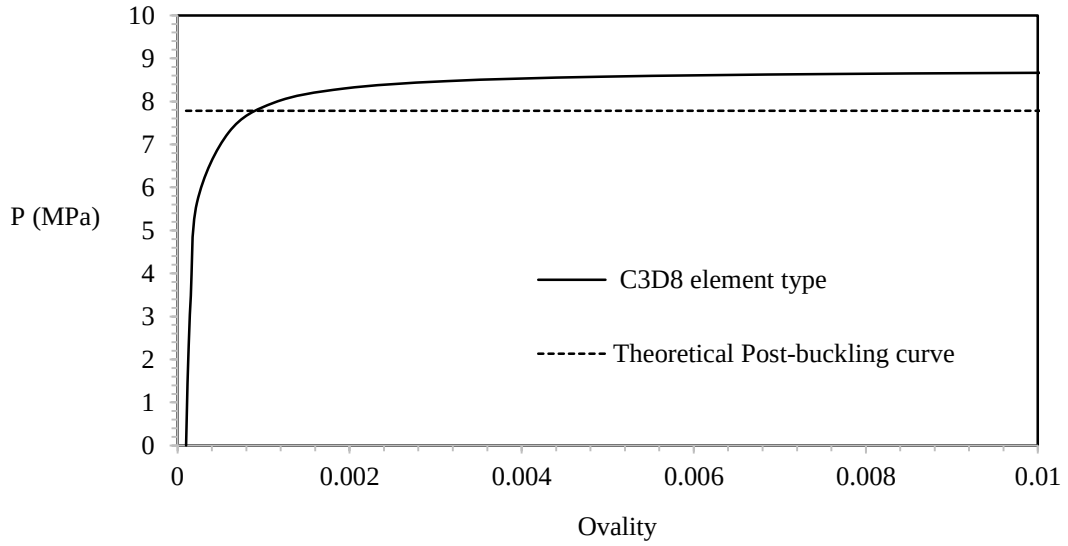

Fig. 2.66 Pressure-ovality response for mesh discretization with C3D8 finite element type (3D elastic ring of D/t=40, L=10mm and $\Delta_o = 0.01\%$).

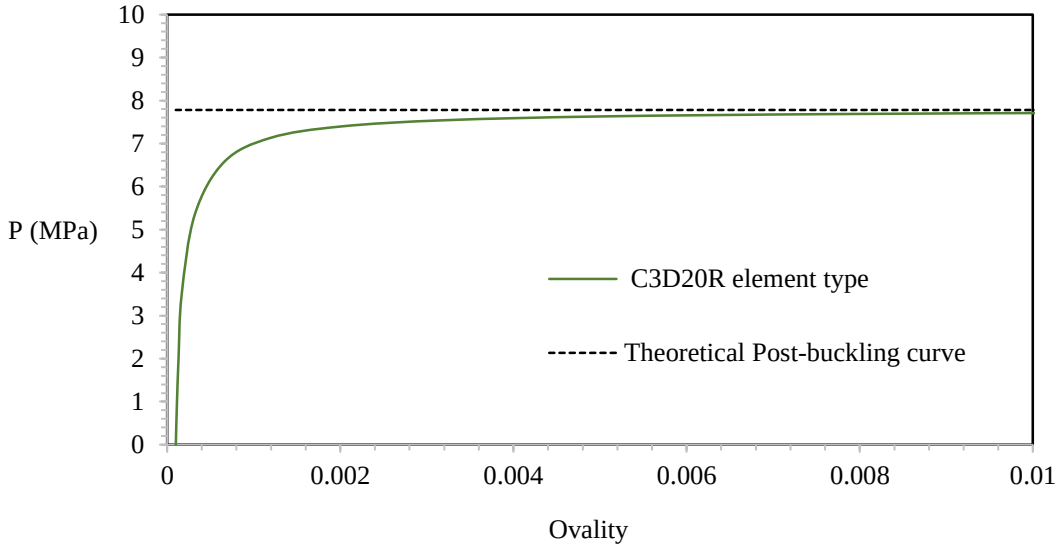

Fig. 2.67 Pressure-ovality response for mesh discretization with C3D20R finite element type (3D elastic ring of D/t=40, L=10mm and $\Delta_o = 0.01\%$).

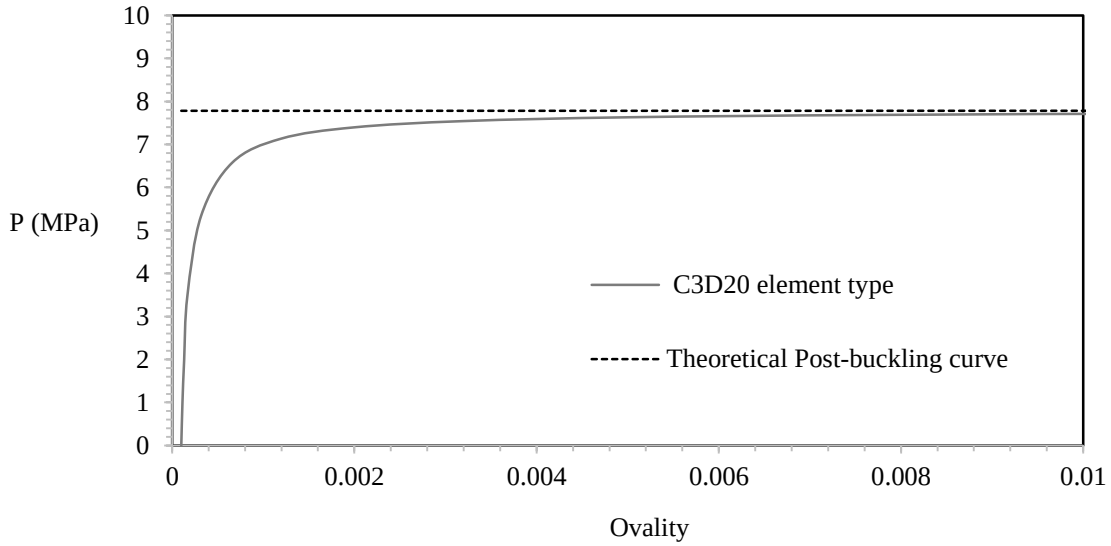

Fig. 2.68 Pressure-ovality response for mesh discretization with C3D20 finite element type (3D elastic ring of D/t=40, L=10mm and $\Delta_o = 0.01\%$).

2.7 Two-dimensional Analysis and Prediction of the Propagation Pressure

The buckling and post-buckling behavior of a ring under external pressure was examined in the previous sections. As it was discussed, the deformation of a ring under plain strain conditions corresponds to the cross-sectional deformation of an infinite long tube. Soon after collapse, a significant downturn in pressure follows and the cross-sectional ovalization increases, due to the formation of four hinges at the quarter points of the ring's circumference. The post-buckling response continues until the two opposite quarter points of the ring's inner circumference come into contact. In the case of a long tube, the collapse of a local section follows a short transient region of propagation until steady-state conditions are reached for the establishment of buckle propagation phenomenon. At the occurrence of steady-state conditions the buckle is assumed to propagate quasi-statically under a constant pressure P_p, which is called propagation pressure.

In the limit of steady state propagation under quasi-static conditions, Chater and Hutchinson [26] proposed a two-dimensional method for the evaluation of the buckling propagation pressure. This evaluation method is based on the ring mode of deformation under plain strain conditions and the assumption of an idealized material. More specifically, while the buckle propagates quasi-statically, it is assumed that the material points of the tube are subjected to monotonic plastic loading. This assumption neglects the presence of non-proportional stresses during deformation and thus, it is implied that the material's deformation is path independent [27]. **Fig. 2.69** shows schematically the

pressure-change in area response for a ring's cross-section. The stages ΔA_i and ΔA_f correspond to the initial and final change in area respectively. The initial and final stages of the cross-sectional area are referred to the undeformed and fully deformed cross-section respectively. The intermittent line stands for the constant pressure, P_P ,which equalizes the two areas ($A_1 = A_2$). This graphical condition is referred to as Maxwell construction [26], [27] or Maxwell line. The product of the change in area between the two stages times the buckle propagation pressure equals the work done by the pressure, ΔW, as follows

$$P_P\,(\Delta A_i - \Delta A_f) = \Delta W \tag{2.20}$$

This work is subsequently absorbed by the ring for the transition from the initial undeformed stage to the final stage of deformation. Because of the path independent deformation history assumption, the work can be calculated form the following equation

$$\Delta W = \int_{\Delta A_i}^{\Delta A_f} P\, d\Delta A \tag{2.21}$$

The condition of Maxwell's line is satisfied by equating (2.20) and (2.21) and thus, the propagation pressure can be evaluated by the following equation

$$P_P = \frac{1}{(\Delta A_f - \Delta A_i)} \int_{\Delta A_i}^{\Delta A_f} P\, d\Delta A \tag{2.22}$$

The propagation pressure can also be estimated from the plastic hinge model of **Fig. 1.9**, proposed by Palmer and Martin [13]. The internal work produced by the four plastic hinges of momentum M_p is expressed as follows

$$W_{int} = 4\, M_p\, \frac{\pi}{2} \tag{2.23}$$

The external work produced by the pressure is

$$W_{ext} = P\,(R\sqrt{2})^2 \tag{2.24}$$

By equating the expressions of (2.23) and, (2.24) the propagation pressure can be evaluated from the following expression

$$P_p = \pi \sigma_y \left(\frac{t}{D}\right)^2 \tag{2.25}$$

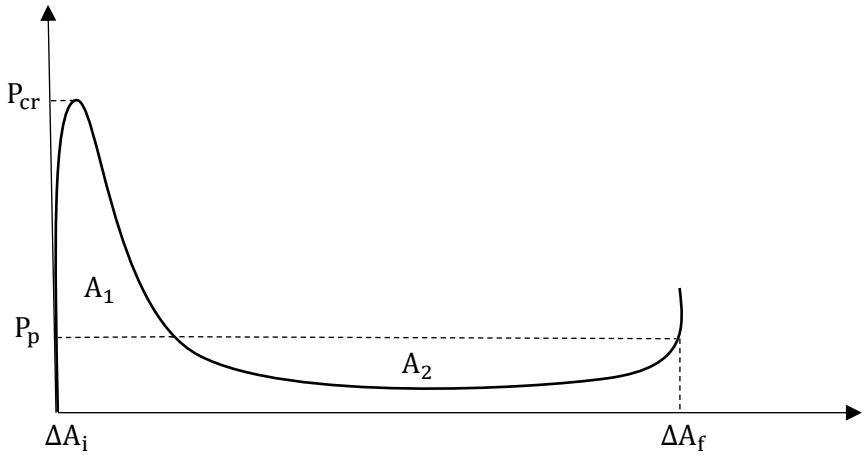

Fig. 2.69 Pressure-change in deformed cross-sectional area of a ring response. The intermittent line separates two equal areas ($A_1 = A_2$).

2.7.1 Prediction of the propagation pressure through Case Studies

The rings of D/t=20 and D/t=30 (**Table 2.3**) are considered as case studies for the prediction of the propagation pressure by the establishment of Maxwell's line condition. An initial ovality of 1% and 0.05% is induced in the rings of D/t=20 and D/t=30 respectively. **Fig. 2.70** and **Fig. 2.71** depict the variation of pressure with the deformed cross-sectional area for the rings of D/t=20 and 30 respectively. The Maxwell lines are also included in the responses for the estimation of the propagation pressure. The propagation pressure is estimated as 5.3 MPa and 2.2 MPa for the rings of D/t=20 and 30 respectively.

The propagation pressure of the above rings will be estimated by equation (2.25) as well. By substituting the geometric parameters for each ring and the material properties, the calculated propagation pressures are 3.36 and 1.52 MPa for the rings of D/t=20 and 30 respectively. In the upcoming chapter, the problem of propagation pressure will be addressed again by performing three-

dimensional numerical analyses of tubes with the same geometric cross-sectional parameters. Therefore, the present estimations of propagation pressures will be compared with those of the full-scale analysis.

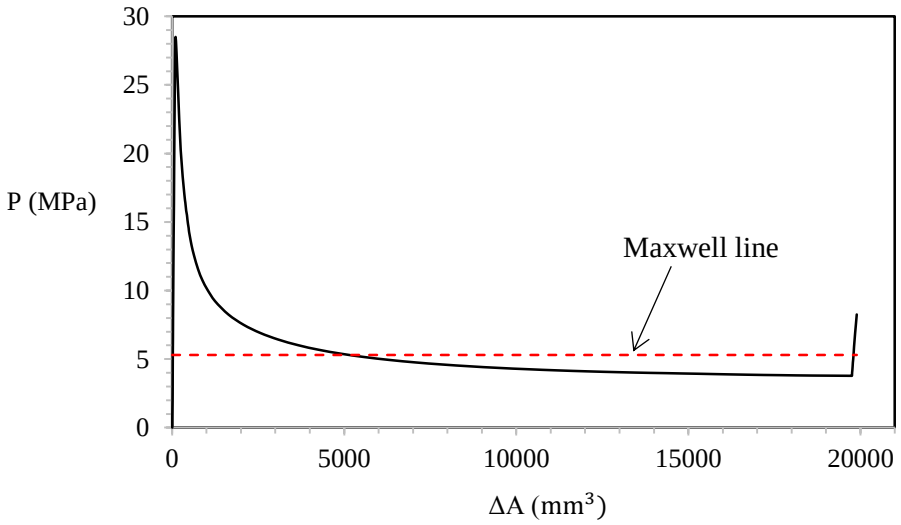

Fig. 2.70 Pressure versus change in area response of a ring with D/t=20. The propagation pressure is estimated by the Maxwell line condition.

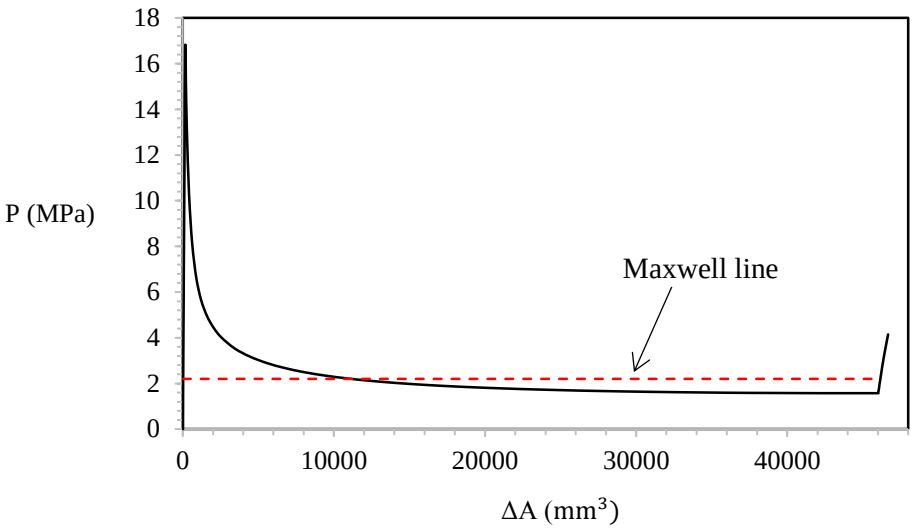

Fig. 2.71 Pressure versus change in area response of a ring with D/t=30. The propagation pressure is estimated by the Maxwell line condition.

Chapter 3 - Analysis of Initiation and Steady-State Buckle Propagation in Tubes

3.1 Introduction

The problem of propagating buckles along the length of long tubular members is of great importance, since it is strongly connected with the collapse of subsea pipelines. Once the buckle initiates, due to local dents or imperfections in the pipe wall region, it propagates under a critical pressure, which is the propagation pressure. The significance of this pressure was pointed out in the previous chapters, and it was presented as the pressure value requirement for a buckle to propagate under steady-state quasi-static conditions. In this chapter the problem of buckle propagation will be addressed again by the finite element analysis of three-dimensional (3D) models, which undergo external pressure loading. The geometric parameters of **Table 2.3** will be considered for the models with adequate length L for reaching steady-state conditions of buckle propagation. The models will be developed in the general-purpose Finite Element program ABAQUS/ standard. The estimations of the propagation pressure from the three-dimensional analyses will be compared with those of the previous chapter. Furthermore, the propagation pressure sensitivity to finite element type and pipe length is examined through parametric analyses.

3.2 Numerical Modeling

Three-dimensional models of length L=15D and two different D/t ‘s (D/t=20 and 30) are developed in the ABAQUS numerical framework. The material properties are chosen to be the same with those of the two-dimensional models, and thus the material properties of steel grade X65 are considered (**Table 2.2**). For the numerical modeling, the one-fourth of a half pipe is considered for analysis with a length of L=15D. The mesh consists of 25 elements in the circumferential direction, 4 elements in the through-thickness direction and 150 elements in the longitudinal direction. Therefore, the models are discretized by a total number of 15000 elements. The finite element models are discretized by 8-node quadrilateral in-plane general-purpose continuum shell elements of reduced integration (SC8R). The choice of the type of finite elements is important for obtaining reliable results, and this issue will be discussed later in this document. Therefore, three-dimensional models of two different values of D/t are created. **Fig. 3.1** shows the one-fourth of a half pipe model and the mesh used to discretize the domain with SC8R finite elements. The boundary nodes at the cross-section of plane Z=0, are constrained to have zero displacements in Z direction and zero rotations about the X and Y axes. These restrictions are applied to the model by selecting the «ZSYMM» boundary

condition option in ABAQUS numerical framework. On the other hand, the boundary nodes at the cross section of plane Z=15D are constrained with the «ENCASTRE» boundary condition option, which aborts the displacements and rotations of nodes in X, Y and Z directions. Furthermore, the nodes of the tube generator sector at X=0 and $\theta = \pi/2$, are constrained to have zero displacements in X direction and zero rotations about the Y and Z axes. This type of restriction is denoted in ABAQUS numerical framework as «XSYMM» boundary condition. Finally, the «YSYMM» boundary condition is assigned to the boundary nodes of the domain's edge at Y=0 and θ=0, so that the nodes have zero displacements in Y direction as well as zero rotations about the X and Z axes.

A necessary condition for the propagation of a buckle is that the pipe should bear a local damage or imperfection, so that the buckle be initiated from this region of concentrated damage (Chapter 1). Therefore, a local imperfection in the form of ovality is introduced in the finite element models. The imperfection is assigned by permitting the existence of an initial displacement of magnitude U in the unloaded condition of the structure. **Fig. 3.1** shows the point «A», where an initial displacement in Y direction is applied. When the displacement is removed, the point does not return to its original position due to elastic-plastic material properties. Thus, the cross-section, where the point A is located, does not return to its original circular shape and it takes an oval shape. The initial displacement is different between the two D/t models, and thus the models have different values of initial ovality. More specifically, the models of D/t=20 and 30 are assigned the initial ovality values of 1%, 0.05% respectively.

The initial ovality affects the collapse pressure but not the value of the propagation pressure under steady state conditions. Based on the arguments of the previous chapters, the cross-sectional's collapse sequence will follow the ring collapse mode under plain strain conditions. Thus, to restrict the translation of the top side through negative Y axis, a three-dimensional analytical rigid surface is developed, and a contact pair is created between the upper surface of the analytical rigid body and the inner surface of the model by using the surface-to-surface method. The translation of the model's inner side through the analytical rigid body is aborted by using the penalty method of nonlinear contact stiffness behavior as an interaction property of the pair.

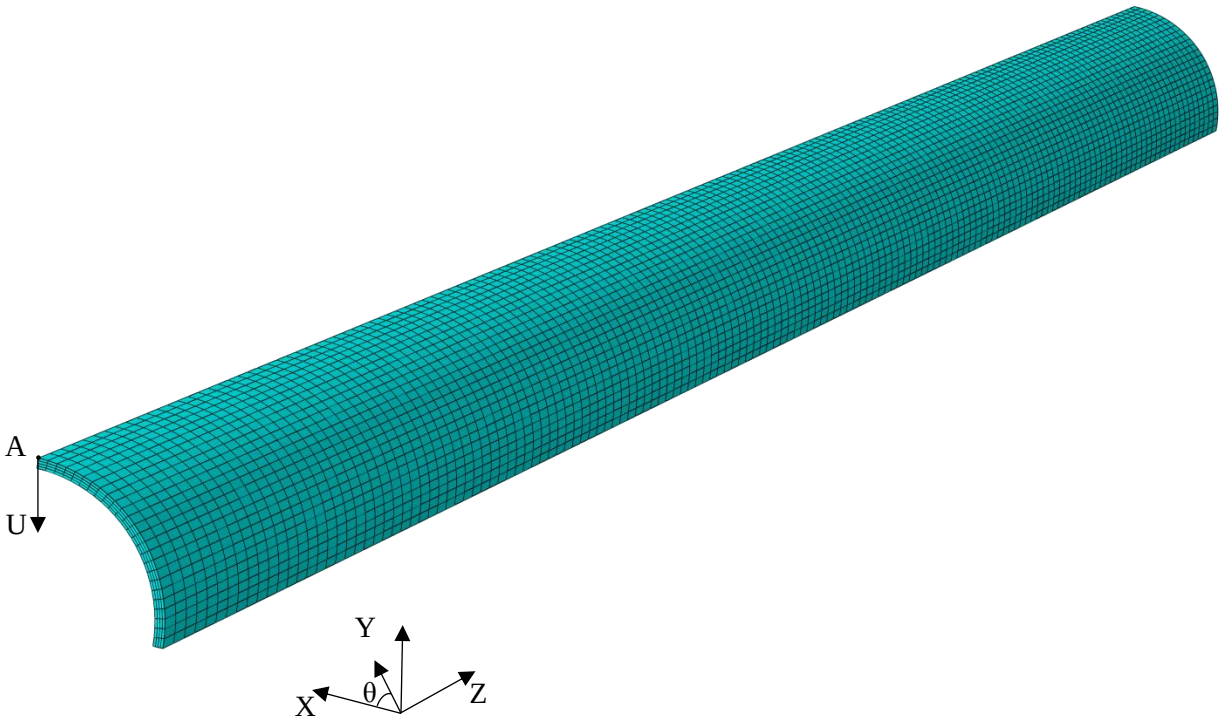

Fig. 3.1 The three-dimensional model of length L=15D used in the finite element analyses of pipes with D/t=20 and 30.

The analysis is developed through four incremental steps. In the first step, which is denoted as the initial step in ABAQUS, the boundary conditions are applied on the model in the way described above. Also, the displacements and rotations of the analytical rigid body are aborted. That is achieved by using the «ENCASTRE» boundary condition on a Reference Point (RP) of the rigid body. The next step is a static general step, which consists of the application of the initial displacement in the unloaded stress-free structure. In the third step, the imposed displacement is removed, and the boundary conditions are applied on the imperfect model. This step is also general static. In the last step of the analysis (fourth step), the uniform external pressure load is applied on the outer surface of the model. In this step a nonlinear analysis is conducted using Riks' continuation method and thus the pre-buckling response, the collapse pressure, and the unstable post-buckling response are obtained.

3.3 Numerical Results

In this section the numerical results of buckle propagation pressure will be presented for the 3D models of D/t=20 and 30. The numerical results of propagation pressure will be compared with those of section 2.7.1 and with those of accurate analytical expressions for the calculation of propagation pressure.

3.3.1 Numerical results of buckle propagation pressure

The equilibrium path of pressure-change in volume responses will be created for the estimation of the propagation pressure. The initial volume of the model was taken as $V_o = \left(\pi {R_{in}}^2 / 4\right) L$. The numerical results of pressure are normalized by the yield pressure P_y (1.18), and the integrated change in the volume of the model upon deformation is normalized by the initial volume V_o. Therefore, the equilibrium path of pressure against the change in volume response is created, and the result is shown in **Fig. 3.2a.** For the pipe model of D/t=30. The numbers on the response correspond to the deformed configurations of **Fig. 3.3.** At stage (1) of **Fig. 3.2a**, collapse occurs at the region of the pipe where the local damage exists. The pipe collapses at a pressure maximum of $P_{co} = 18.04$ MPa . The local initial ovality of the model is 0.05%. As it was mentioned in the previous section, the magnitude of initial imperfection affects only the collapse pressure of the pipe, and it does not influence the value of the propagation pressure. After the collapse stage, the pressure carrying capacity drops significantly (2) until a minimum pressure value is reached at stage (3). The stage of minimum pressure corresponds to the first contact between the quarter points of the most deformed cross section. In the meanwhile, a small increase in pressure is observed on the transition from stage (3) to stage (4). The contact between the two surfaces locally "strengthens" the most deformed cross-section, and thus an immediate and short-length stiffening of the pipeline is observed, due to the pressure increase [26], [27]. After stage (4), the collapsed or "buckled configuration" starts to propagate quasi statically along the pipe length under steady-state conditions. Therefore, the propagation pressure is estimated as $P_p \approx 3.08$ MPa for the D/t=30 pipe model under consideration. A volume like parameter is also used to examine the relation of pressure to volume reduction for the two pipe models of different D/t ratios. This parameter is expressed by the following formula

$$\widehat{\Delta V} = \frac{L\, R_{in}}{N} \sqrt{\sum_{i}^{N} (U_{i,y})^2} \qquad (3.1)$$

where L and R_{in} are the length and the internal radius of the pipe (L=15D) respectively, $U_{i,y}$ is the displacement in Y direction of a node i, which is located at the inner edge of the tube upper generator and N is the number of nodes i at the inner edge of the tube upper generator. The variation of pressure with the volume like parameter for the tube of D/t=30 is presented in **Fig. 3.2b.** The pressure versus change in volume responses for the case of D/t=20 are presented in **Fig. 3.4**. The deformed configurations of that case are of the same nature as those presented for the case of D/t=30, and thus

are not included here. The propagation pressure is estimated as $P_p \approx 8.42$ MPa for the tube of D/t=20.

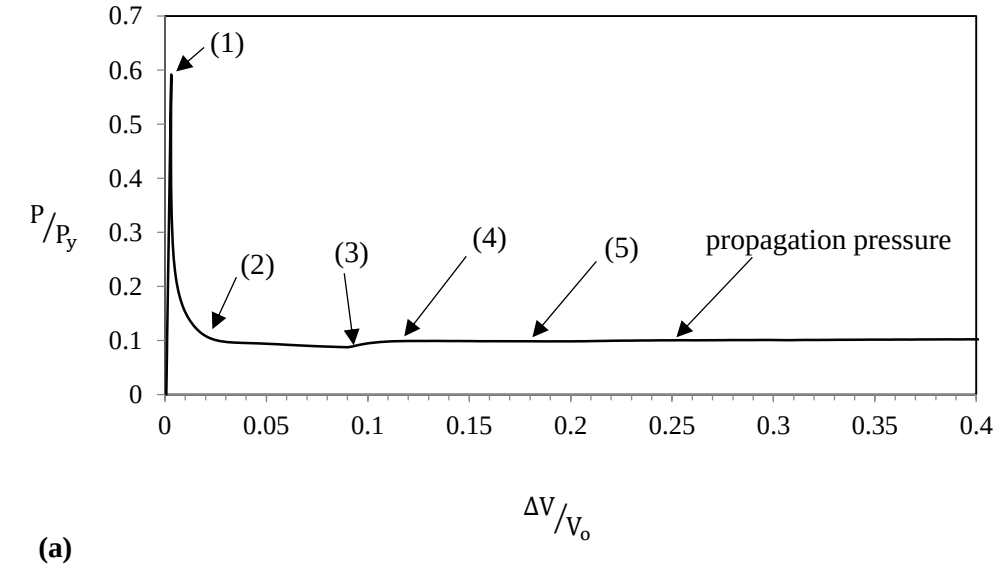

(a)

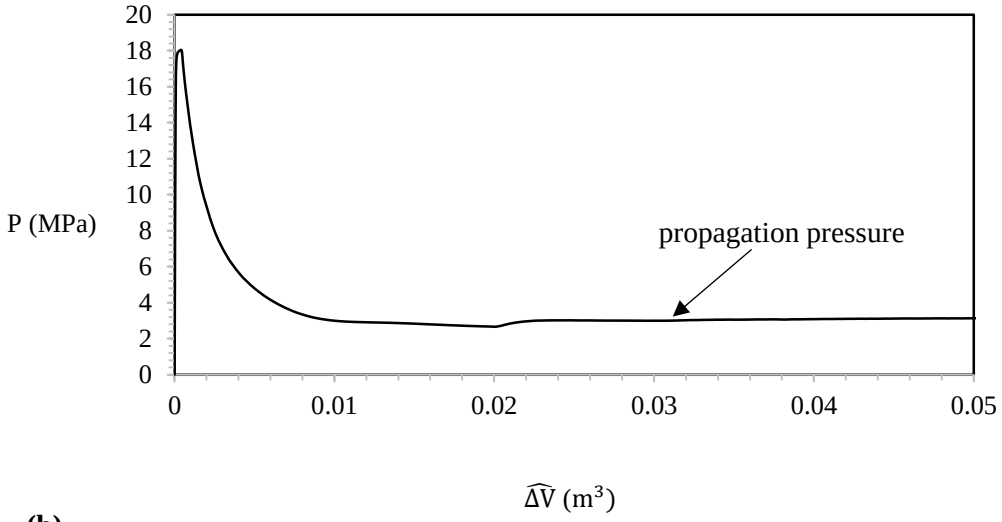

(b)

Fig. 3.2 Pressure-change in volume responses for the tube of D/t=30. (a) The variation of pressure with the integrated volume reduction and (b) the variation of pressure with volume like parameter.

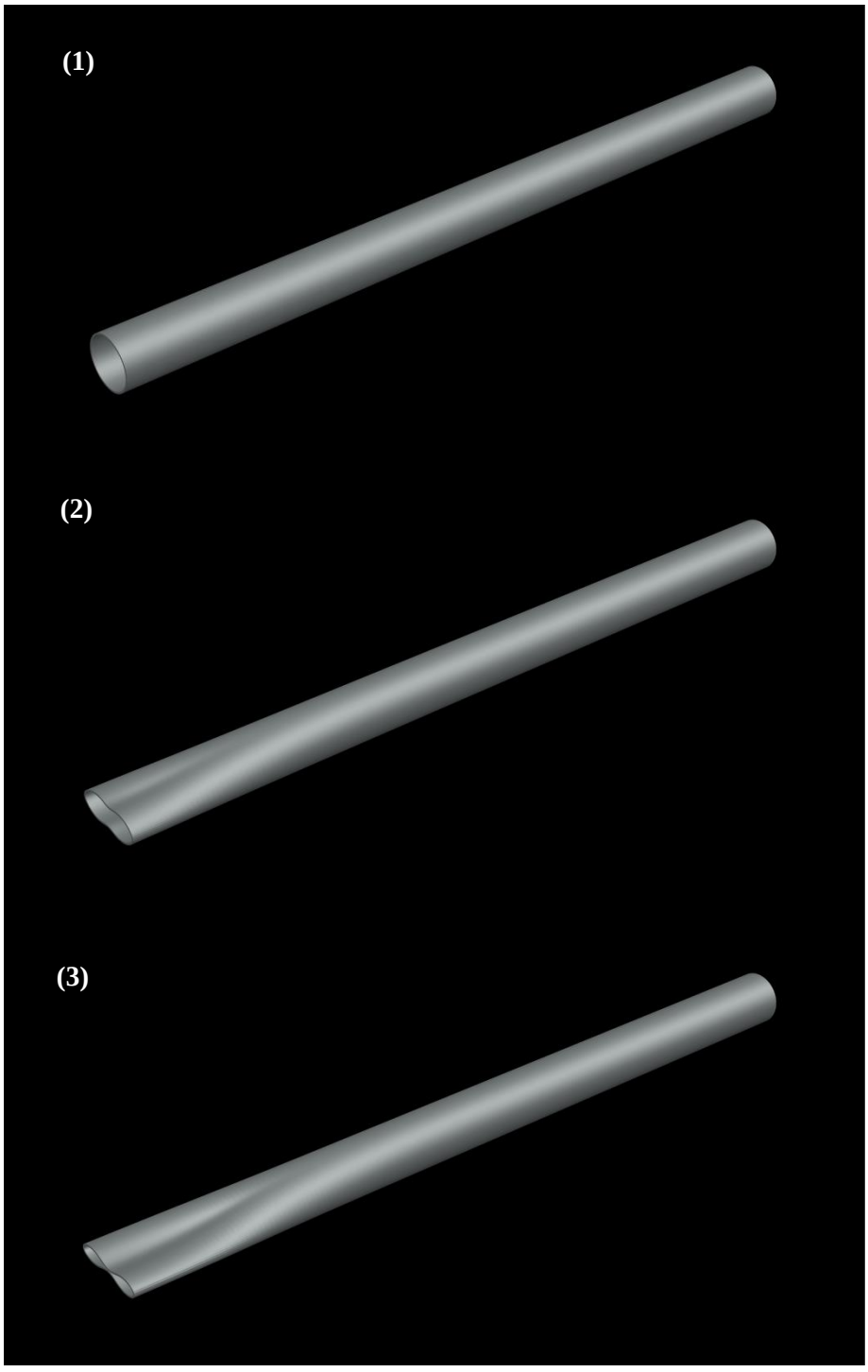

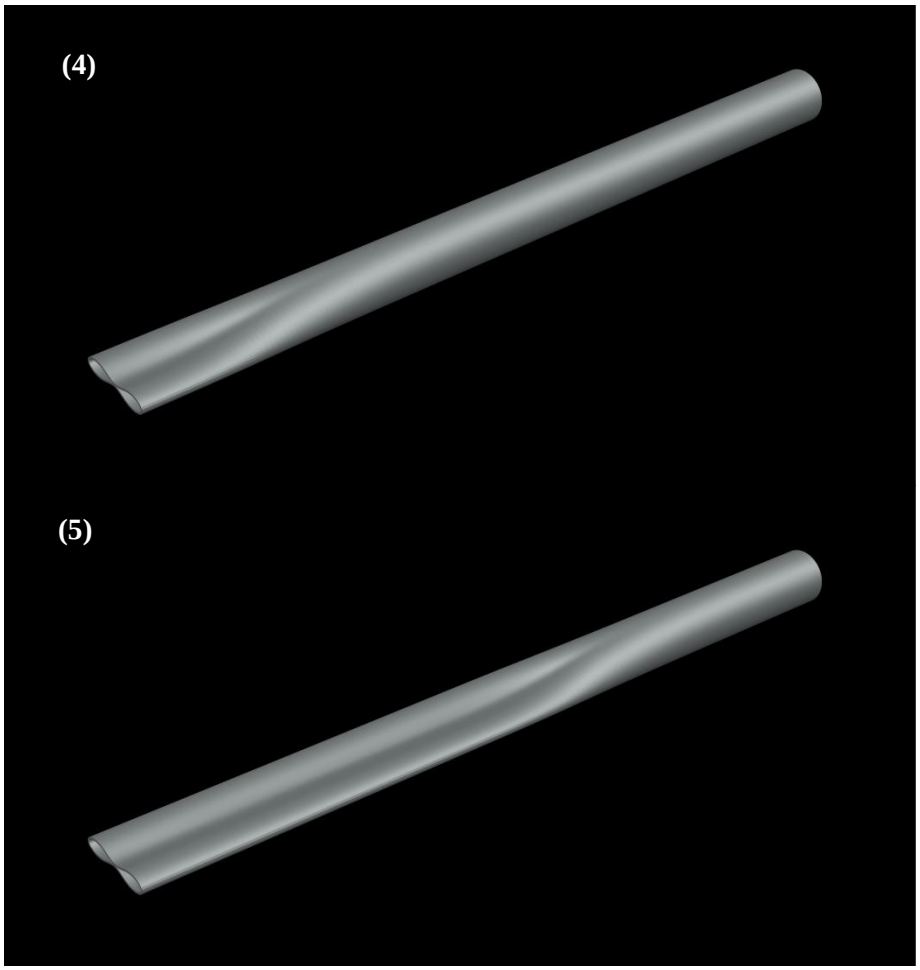

Fig. 3.3 The numerical simulations of the sequence of buckle propagation phenomenon for the corresponding (1)-(5) stages of pressure-change in volume response (D/t=30).

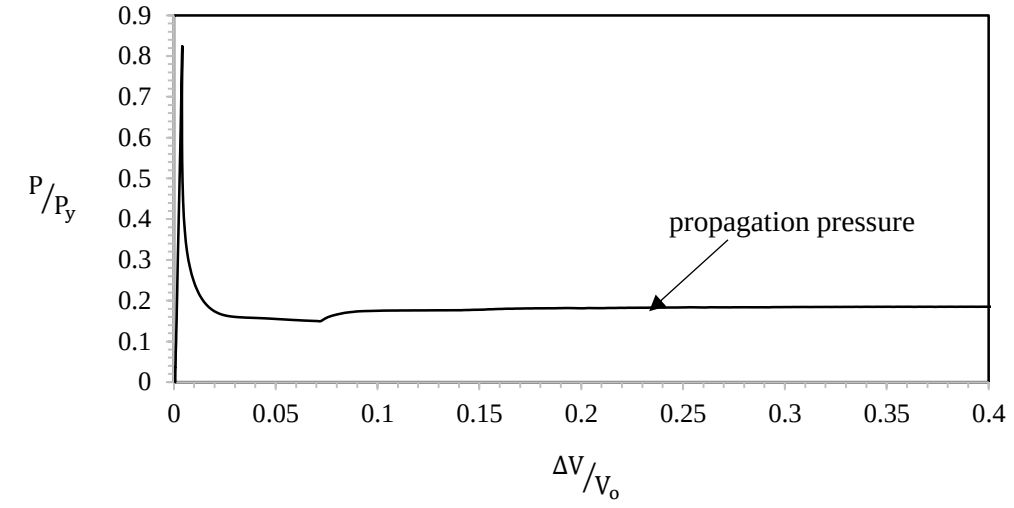

(a)

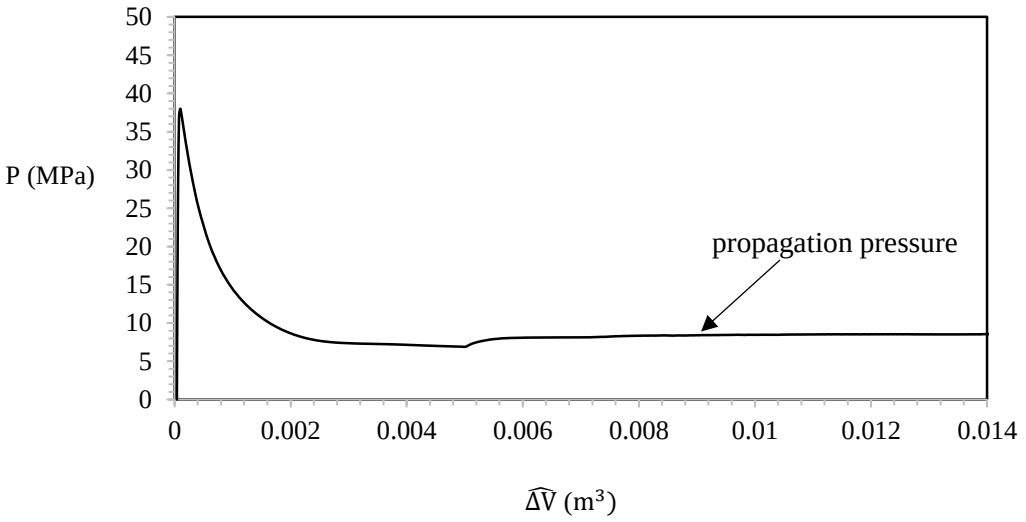

(b)

Fig. 3.4 Pressure-change in volume responses for the tube of D/t=20. (a) The variation of pressure with the integrated volume reduction and (b) the variation of pressure with volume like parameter.

As mentioned in the previous chapter, the deformation of a ring under plain strain conditions is identical to the states of cross-sectional deformation of an infinite long tube. Based on the arguments proposed by Chater and Hutchinson [26] for steady state buckle propagation under quasi-static conditions , it is assumed that the deformed configurations of the pipe at locations before and after the propagating buckle correspond to the deformed configurations of the ring under plain strain conditions

[28]. **Fig. 3.5** shows the sequence of collapse configurations for the D/t=30 pipe cross-section, where the initial imperfection in the form of ovality is assigned (**Fig. 3.1**). The states of deformation for the 2D ring of D/t=30, were presented in **Fig. 2.16**. The two-dimensional and three-dimensional collapse configurations at the stage of contact are presented in a common figure, as shown in **Fig. 3.6**. The results show that the cross-sectional deformation of pipe at contact is higher than that of ring.

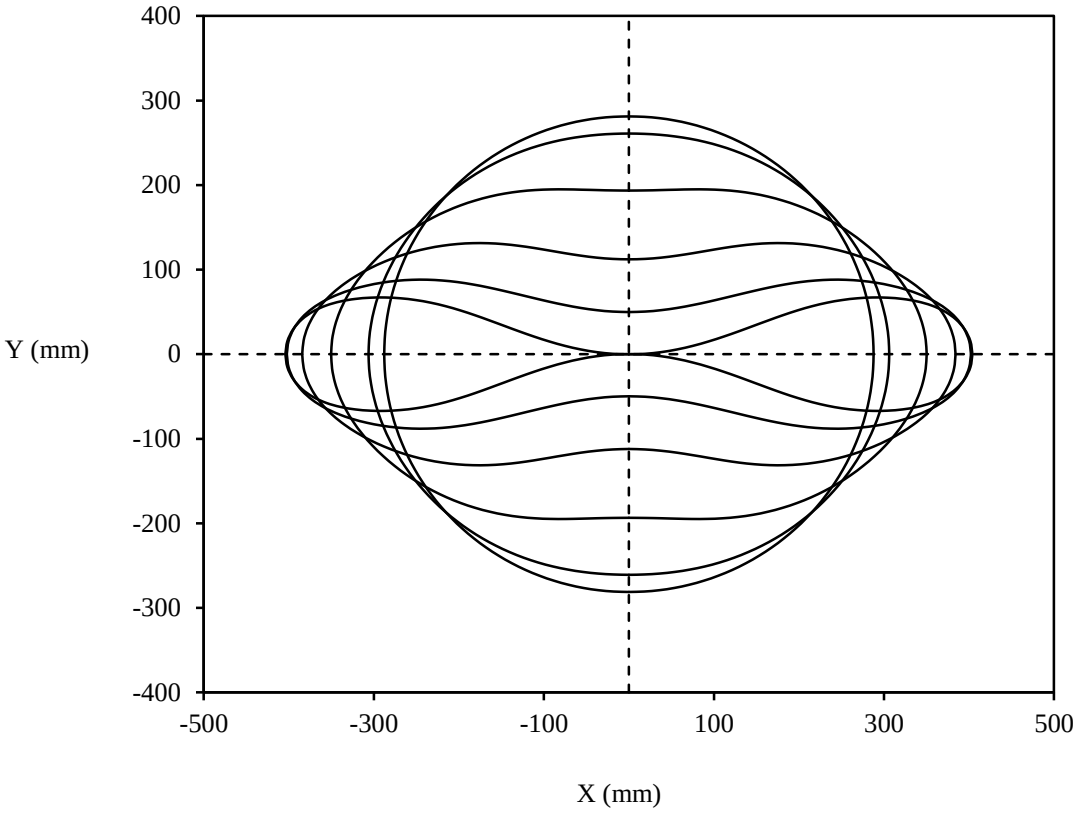

Fig. 3.5 Sequence of collapse configurations for the pipe cross-section where the initial imperfection is assigned (pipe of D/t=30 and L=15D).

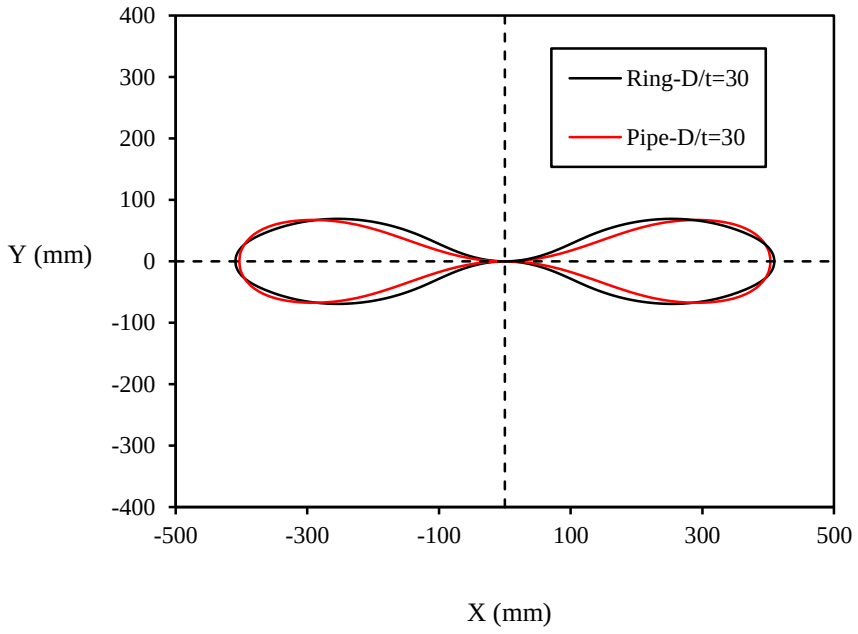

Fig. 3.6 Deformed configurations of ring and pipe cross-sections at the stage of contact.

For the pipe of D/t=30, the first contact between the quarter points of the cross-section, where the imperfection is assigned (**Fig. 3.1**) and the buckle is initiated, is presented by stage (3) in the numerical simulations of **Fig. 3.3**. At this stage, the states of deformation of the pipe that correspond to the states of the cross-sectional deformation at the origin of the model (**Fig. 3.5)**, are selected in the finite element model as shown in **Fig. 3.7**. The sequence of collapse configurations for the six states of deformation of the pipe along the longitudinal direction (**Fig. 3.7**) is shown in **Fig. 3.8**. The collapse configurations of **Fig. 2.16** and **Fig. 3.8** show that the pipe cross-sectional deformation along the longitudinal direction, is higher than the cross-sectional deformation of the ring under plain strains conditions. This observation has already been made at the stage of contact (**Fig. 3.6**), between the two-dimension and three-dimension analysis of the cross-sectional deformation. These differences between two-dimensional and three-dimensional configurations are reasonable because the three-dimensional pipe model is more flexible to deform in three dimensions than the ring model in two dimensions.

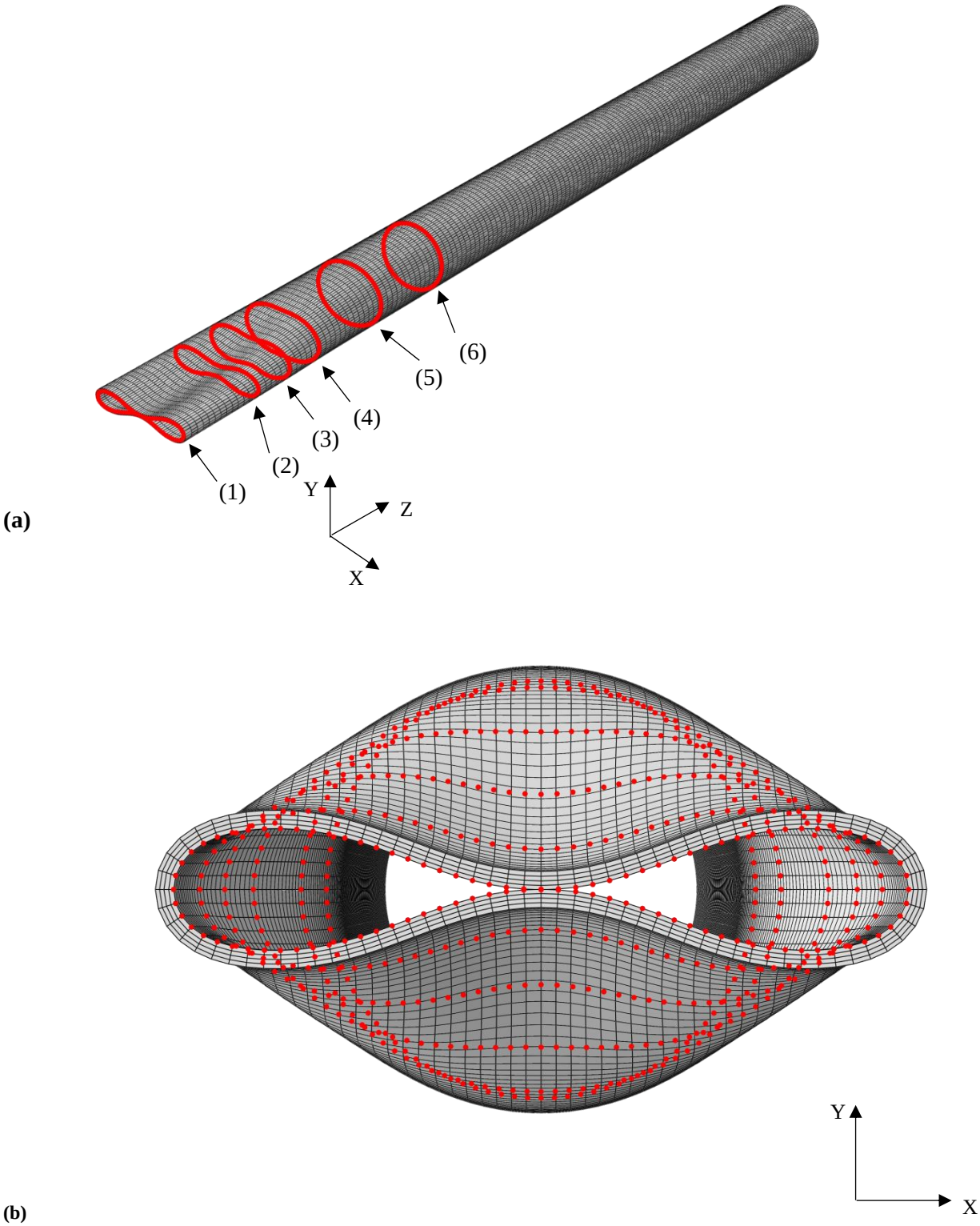

Fig. 3.7 Six different states of cross-sectional deformation along the pipe length at different angles and planes of view.

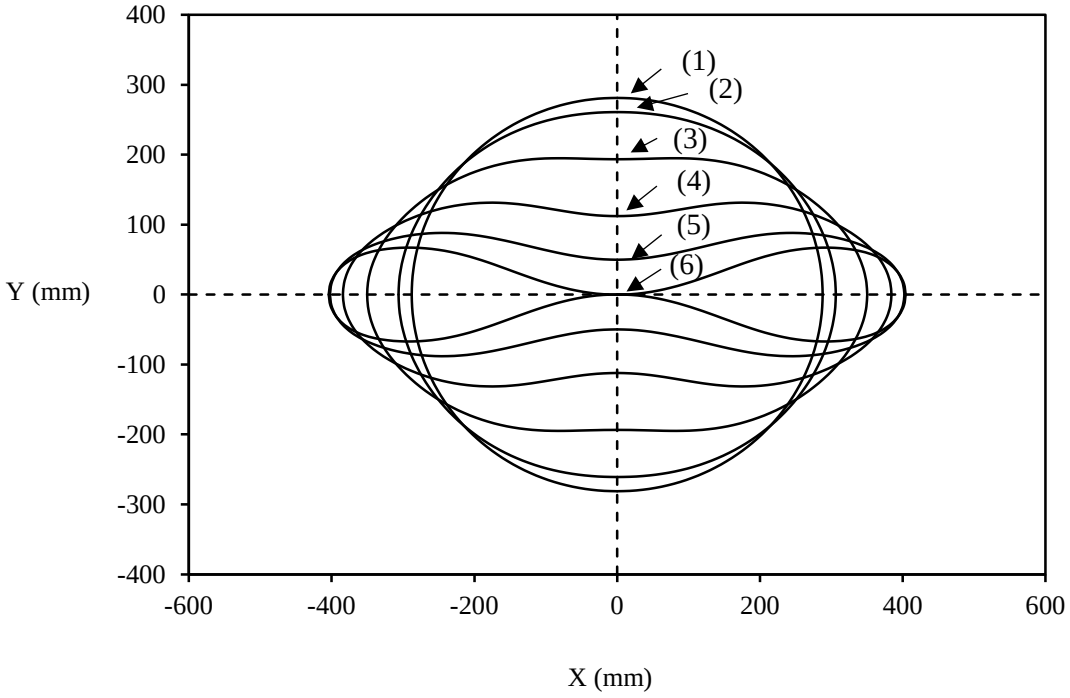

Fig. 3.8 Sequence of collapse configurations for the pipe of D/t=30 along the longitudinal direction. The numbers above the configurations correspond to the states of cross-sectional deformation of Fig. 3.7.

3.3.2 Comparison of analytical and numerical calculations of buckle propagation pressure

In this chapter, accurate analytical expressions from publications and standards will be used to calculate the propagation pressure for the cases of tubes presented above. These analytical results will be compared with the numerical results of the previous section, as well as with the estimations of propagation pressure of section 2.7.1. From the experiments of Kyriakides and Babcock [29], the following analytical expression is postulated for the calculation of propagation pressure

$$P_p = A\,\sigma_y\,(\frac{t}{D})^{\beta} \tag{3.2}$$

where A, β are parameters dependent on the alloys. For the tubes of X65 steel examined here, A=14.5 and β=2.254.

The following expression for calculating the propagation pressure is proposed by API RP 1111 [2] standard

$$P_p = 24\,\sigma_y\,(\frac{t}{D})^{2.4} \tag{3.3}$$

where D is the outside diameter of the pipe, t is the wall thickness and σ_y is the yield pressure of the material.

The proposed formula for the calculation of the propagation pressure is given by DNVGL-ST-F101 [3] standard as follows

$$P_p = 35\,\sigma_y\,a_{fab}\,(\frac{t}{D})^{2.5} \tag{3.4}$$

where D is the outside diameter of the pipe, t is the wall thickness and σ_y is the yield pressure of the material and a_{fab} is a fabrication factor, which is equal to unity for the cases examined here.

The propagation pressure is calculated for both tubes from the expressions (3.2)-(3.4), and the results are listed in **Table 3.1**. The numerical results of section 3.3.1, as well as the results of sections 2.7.1 for the propagation pressure, are listed in the same table. It seems that the two-dimensional analysis underestimates the calculated propagation pressure. The discrepancies between the results can be attributed to the three-dimensional characteristics of buckle propagation phenomenon. While the buckle propagates in the longitudinal direction, the tube's generators deform in the direction of propagation. Therefore, the existence of longitudinal deformation in the model is the reason for the underestimating results of two-dimensional analysis. However, the results from the expressions (3.2)-(3.4) are closer to those of the numerical analysis.

Table 3.1 Propagation pressure estimations (MPa) from the FE models of L=15D and from analytical methods and expressions.

D/t	Numerical calculation	2D Maxwell line	Palmer& Martin	Kyriakides& Babcock	API RP 1111	DNV GL-ST-F101
20	8.42	5.3	3.36	7.20	7.67	8.27
30	3.08	2.2	1.52	2.94	2.95	3.06

3.4 Parameter Study

The parametric dependence of the propagation pressure will be examined in this section. From the analytical expressions presented above, the propagation pressure is dependent on the pipe geometric characteristics and the material properties. Furthermore, it has been concluded from experimental and numerical analyses of the literature [27] that a long enough pipe is needed for the establishment of steady-state propagation conditions. Thus, the variation of propagation pressure with the pipe length will be examined through parameter analyses. Also, the sensitivity of the propagation pressure on the finite element (FE) type of mesh discretization, will be examined by parametric studies.

3.4.1 Effect of finite element discretization

The pipe of D/t=30 will be modeled for different element types. The mesh density will remain the same as that used in section 3.2. Firstly, the 4-node doubly curved shell elements of reduced (S4R) and full integration (S4) are considered for the model. Furthermore, the pipe was discretized by different types of brick elements. More specifically, the model was discretized by 8-node linear brick elements of reduced (C3D8R) and full integration (C3D8). Also, the pipe was discretized by 20-node quadratic brick elements of full integration (C3D20). Therefore, five different analyses have been conducted in ABAQUS standard for the D/t=30 pipe. The variation of pressure with the integrated reduction in volume of the pipe model, is presented by the $P/P_y - \Delta V/V_o$ responses for the S4R, S4, C3D8R and C3D8 finite element types, as shown in **Fig. 3.9**- **Fig. 3.10**. For the finite element type of C3D20, the variation of pressure with the volume like parameter is presented by the $P - \widehat{\Delta V}$ response as shown in **Fig. 3.11**. The observable differences that exist in the collapse pressure, is due to the differences in the initial imperfection values between the analyses. Since the initial imperfection does not influence the propagation pressure estimation, a greater that 0.05 % ovality is used for some element types for the initiation of collapse. From **Fig. 3.9**- **Fig. 3.10** it can be observed that the volume of the corresponding pressure minimum (stage (3) in **Fig. 3.3**), differs between the elements. This discrepancy can be attributed to contact sensitivity between the elements of internal surface and the analytical rigid body.

The propagation pressure for each case can be estimated from the responses, and the results are summarized in **Table 3.2**. In the same table the estimated propagation by using SC8R elements is included as well. It seems that the propagation pressure estimation varies significantly with the element type. The comparison of the estimated propagation pressures of **Table 3.2**, with the calculated propagation pressure from the proposed equation of API RP 1111 standard [2] (**Table 3.1**), shows that the difference is the minimum (2.03% lower with respect to that calculated from (3.3)) when C3D20

elements are used, and the maximum for C3D8 elements (19.32% higher with respect to that calculated from (3.3)). However, the difference is even lower if the numerical estimations are compared with the calculated propagation pressure from the proposed formula of DNV GL-ST-F101 standard [3]. The minimum difference in this case exists for SC8R finite element discretization (0.65% higher with respect to that calculated from (3.4)), and the maximum difference is observed upon C3D8R finite element discretization (16.99% higher with respect to that calculated from (3.4)). Also, the comparison of the numerical estimations of **Table 3.2** with the calculated propagation pressure from the proposed formula of Kyriakides & Babcock [29] gives minimum and maximum differences for C3D20 finite elements (1.70% lower with respect to that calculated from(3.2)) and C3D8 (19.73% higher with respect to that calculated from(3.2)) finite elements respectively.

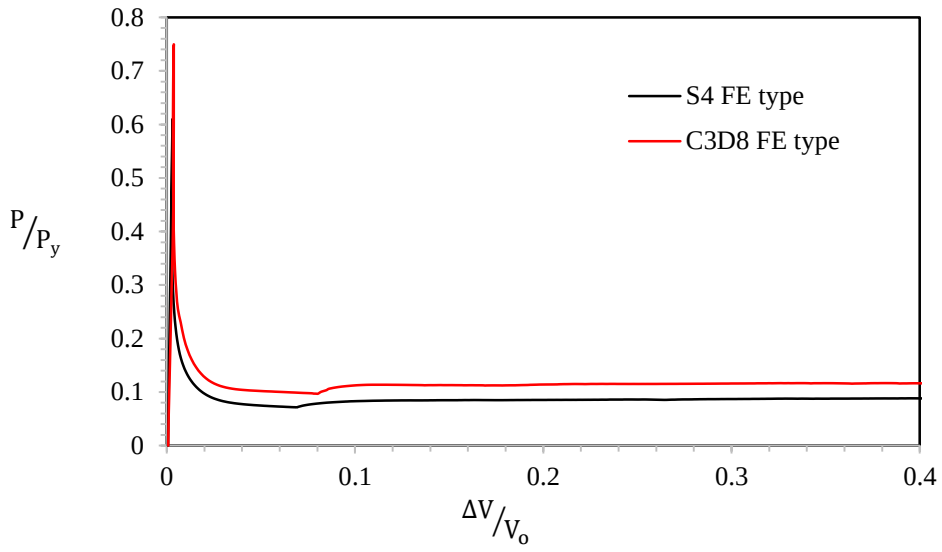

Fig. 3.9 Pressure-change in volume responses for different element types of full integration (D/t=30 pipe model of L=15D).

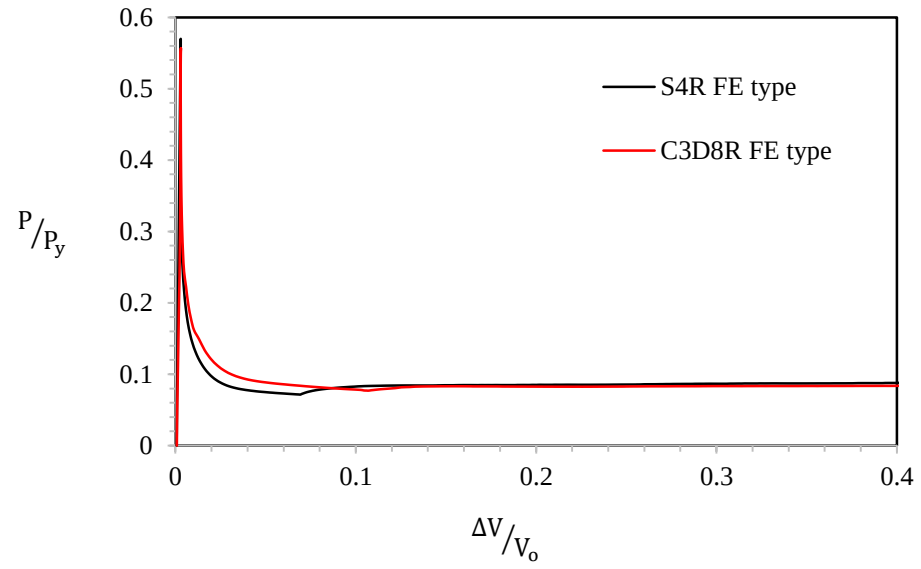

Fig. 3.10 Pressure-change in volume responses for different element types of reduced integration (D/t=30 pipe model of L=15D).

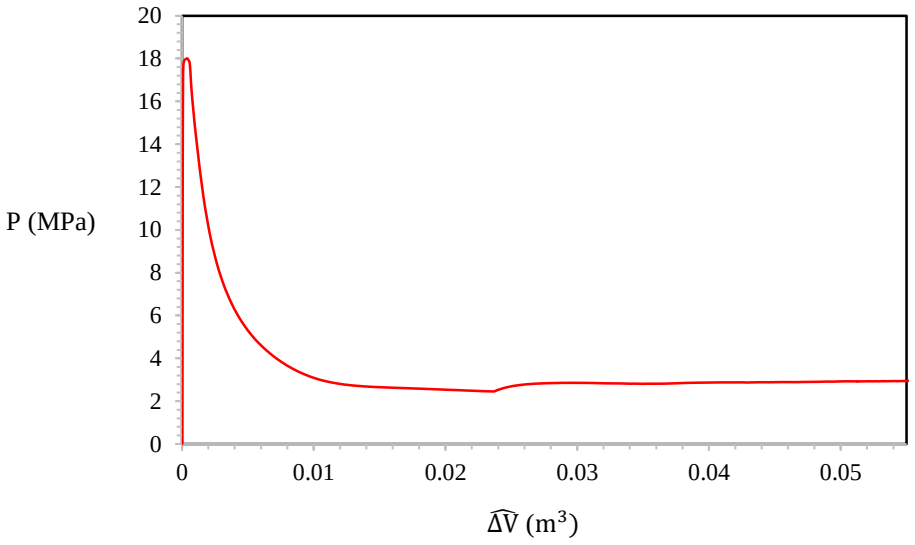

Fig. 3.11 The variation of pressure with volume like parameter for quadratic elements C3D20 (D/t=30 pipe model of L=15D).

Table 3.2 Numerical estimations of the propagation pressure for different element types of reduced and full integration (model of D/t=30 and L=15D).

Element type	P_p (MPa)
SC8R	3.08
S4R	2.62
S4	2.64
C3D8R	2.54
C3D8	3.52
C3D20	2.89

3.4.2 Effect of tube's geometric parameters

The model of **Fig. 3.1** with D/t=30 will be considered here with a length of L=5D to verify the need for a large pipe length, so that the buckle will be propagating under steady-state conditions. The model is discretized with SC8R finite elements, and the mesh consists of 25 elements in the circumferential direction, 4 elements in the through-thickness direction and 100 elements in the longitudinal direction. The variation of pressure with the integrated change in volume is presented in terms of $P/P_y - \Delta V/V_o$ response as shown in **Fig. 3.12**. Clearly, the response is not able to develop a pressure plateau, due to the insufficient length of the pipe model. Thus, the propagation pressure is not possible to be estimated by the analysis of that finite element model. The important factor of sufficient pipe length is presented in **Fig. 3.13** by comparing the response of **Fig. 3.12** with that of **Fig. 3.2**a in a common figure. The differences between the two responses are outstanding, and they highlight the need for an adequate pipe length for the establishment of steady-state buckle propagation conditions.

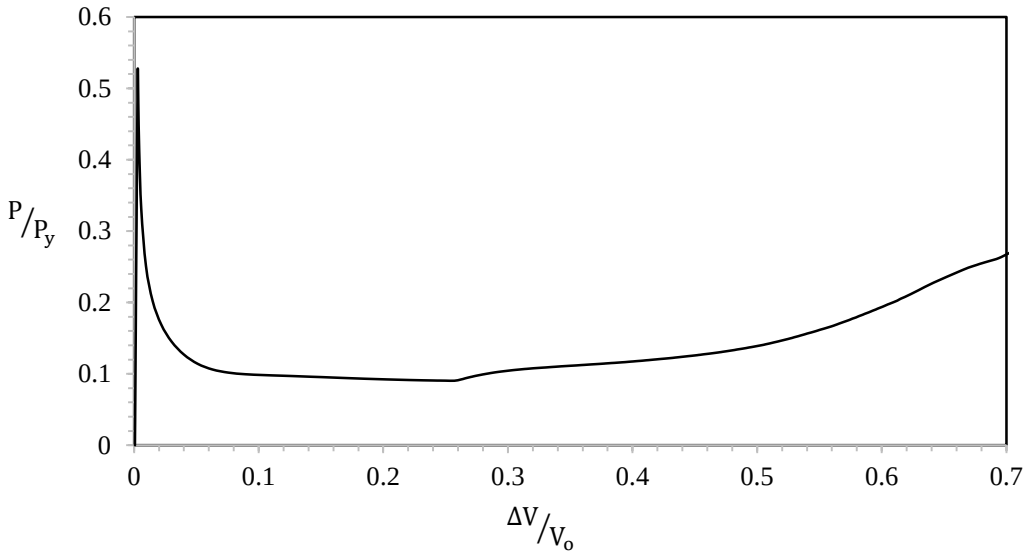

Fig. 3.12 Pressure-change in volume response for a short pipe of D/t=30 and half-length of L=5D.

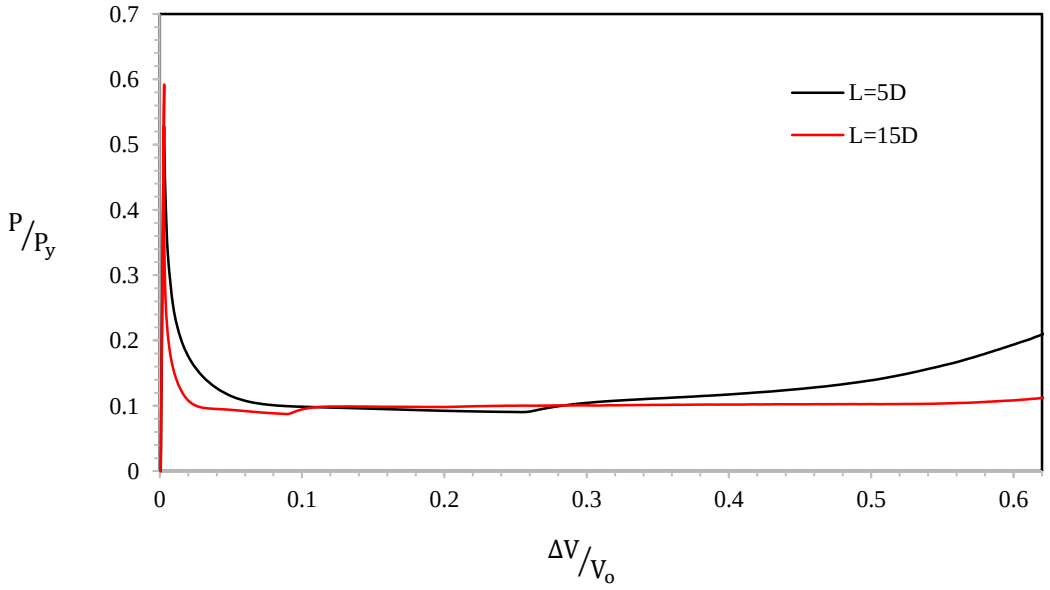

Fig. 3.13 Comparison of pressure-change in integrated volume responses for the finite element models of L=5D and L=15D and cross-sectional geometry D/t=30.

Chapter 4 – Finite Element Analysis of Integral Buckle Arrestors

4.1 Introduction

The problem of collapse and its catastrophic propagation under a constant pressure, the «propagation pressure», along a pipeline length, was studied numerically in the previous chapter. Once the buckle is initiated locally at a pipeline section, it will propagate in a quasi-static manner along a pipeline length, unless an obstacle is reached to abort its further propagation. One way to «arrest» the propagation of a buckle would be achieved by increasing the pipe wall thickness. This approach ensures that the constant pressure of the sea floor environment is always lower than the propagation pressure, and thus local buckles will not propagate along the pipeline length. Practically, this method increases the costs of pipeline material and installation methods (Chapter 1) and thus it would not be considered for a pipeline project [30]. Following the concept of thicker wall thickness, special devices have been developed for the efficient arrest of a propagating buckle. These devices are referred to as «buckle arrestors» and they are installed to connect periodically pipe sections along the line. A buckle arrestor has an average wall thickness value, which is higher than that of the pipeline, and thus it acts as an obstacle for the further propagation of a buckle. There are different types of buckle arrestor devices which are dependent on the water depth. For relatively shallow water depths the **slip-on** arrestor device is generally used, whereas for pipeline projects established in deep water, the **integral** arrestor device is generally used [30]. The buckle arrestor devices safeguard the structural integrity of the pipeline and make the structure stiffer. Once the buckle approaches the arrestor, it will not continue further its path of propagation, and the pressure will increase until a maximum pressure, due to the local substantial stiffening of the structure. The maximum pressure is referred to as «crossover pressure», and it is dependent on the arrestor geometric characteristics. The magnitude of the crossover pressure indicates the ability of the arrestor device to efficiently abort the further propagation of a buckle.

The integral arrestor device will be considered in this thesis. This device consists of an internal diameter, which is of the same scale as that of the pipeline, and a thicker wall thickness compared to that of the pipeline. This device is welded between two pipe segments to arrest the transition of buckle from the upstream pipe section to the downstream pipe section. The geometric characteristics of an integral arrestor are presented schematically in **Fig. 4.1**. It should be mentioned that the geometry of buckle arrestor and its way of connection with the pipe sections, correspond to the finite element model that is considered for analysis as it will be presented in the following section. A more general schematic representation of an integral buckle arrestor is presented in [27], [30], [31]. As shown in **Fig. 4.1**, the buckle arrestor is characterized by a length « L_A» and a wall thickness «h», which is

higher than the pipe wall thickness «t» that is connected to. In the same figure, the short regions of variable thickness used to connect the device and the pipe segments are shown as well.

This chapter focuses on the numerical study of an integral buckle arrestor, which connects two pipeline sections. For that purpose, a three-dimensional (3D) model is developed in the general-purpose Finite Element program ABAQUS/ standard. The crossover pressure will be estimated for an integral arrestor of given geometric characteristics. Also, the crossover pressure sensitivity to finite element type is examined through parametric analyses.

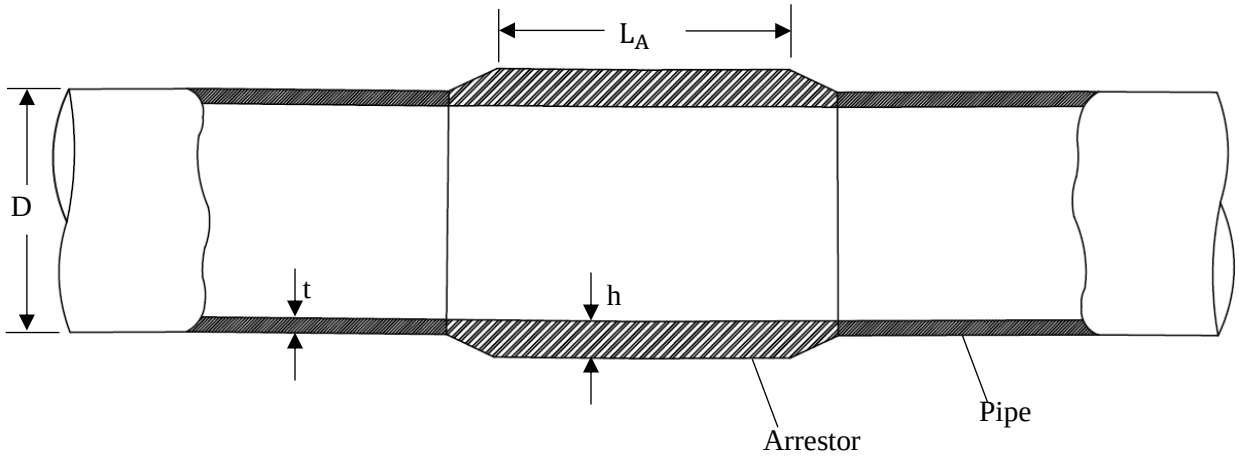

Fig. 4.1 Schematic representation of the geometric characteristics of an integral buckle arrestor, which connects two pipe sections.

4.2 Numerical Modeling

A three-dimensional finite element model was developed in the ABAQUS numerical framework, to simulate the initiation and quasi-static propagation of a buckle along the pipe length, and its arrest by an integral arrestor, which connects two pipeline segments. The pipe of D/t=30 is considered with the cross-sectional geometric parameters of **Table 2.3** and the material properties of steel grade X65 (**Table 2.2**). The integral arrestor is considered with the same material properties as the pipeline, and its geometric parameters are the same as those used in [21]. Therefore, the integral arrestor of length $L_A = 1.198D$ and thickness h=2.5t is used in the finite element model analysis. The finite element model is an assembly of an upstream pipe segment of length L_1, a transition segment of length L_T, an arrestor of length L_A, a transition segment of length L_T and a downstream pipe segment

of length L_2. The length of the upstream pipe section is $L_1 = 10D$, so that the buckle can propagate under steady state conditions, and the transition sections have a length of $L_T = 50$ mm. The values of L_1, L_T, L_2 are similar to those used in [21]. Therefore, a finite element model with a total length of L=20D is created in the ABAQUS numerical framework. For the numerical modeling, the one-fourth of a pipeline section, which consists of two pipe sections connected by an integral arrestor, is considered for analysis as shown in **Fig. 4.2**. The whole model domain is discretized by 20-node quadratic brick elements of full integration (C3D20). The circumferential directions of pipe sections and arrestor consist of 25 elements, whereas in every through-thickness direction of the model 4 elements are used. In the longitudinal direction, 60 elements are used in the downstream pipe section of L_2 and 25 elements are used in L_A. The upstream pipe section of $L_1$is partitioned at a distance of 9D from the axes origin, and thus the section is divided into two parts. In the first part of length 9D, 40 elements were used in the longitudinal direction, whereas in the second part of length D 20 elements are used. The transition sections are discretized with 4 elements in the longitudinal direction. The boundary nodes at the cross sections of planes Z=0 and Z=20D are constrained with the «ZSYMM» boundary condition option as described in section 3.2. Furthermore, the nodes of the model sector at X=0 and $\theta = {}^{\pi}/_{2}$, are constrained with the «XSYMM» boundary condition, whereas the nodes of the model edge at Y=0 and θ=0 are constrained with the «YSYMM» boundary condition.

An initial imperfection in the form of ovality is introduced in the model for the formation and initiation of a local buckle. Following the procedure of section 3.2, the imperfection is assigned at a point «A» in the origin (**Fig. 4.2**), by means of displacement U. The magnitude of the given displacement at point A is U=8. In that imperfect region, the structure locally buckles due to uniform pressure loading at the external surface of the pipe. Therefore, the cross section, where the point A is located takes an oval shape. From the collapse configurations of the previous chapters, it is expected that the imperfect cross-section at the origin (**Fig. 4.2**) will follow a sequence of collapse configurations similar to those presented in **Fig. 3.5**. Therefore, to restrict the translation of top side through negative Y axis, a three-dimensional analytical rigid surface is created. A master-slave contact pair is created between the analytical rigid surface and the part of the inner surface that will come into contact. The contact is modelled using the penalty method algorithm, which takes into account nonlinear contact stiffness behavior.

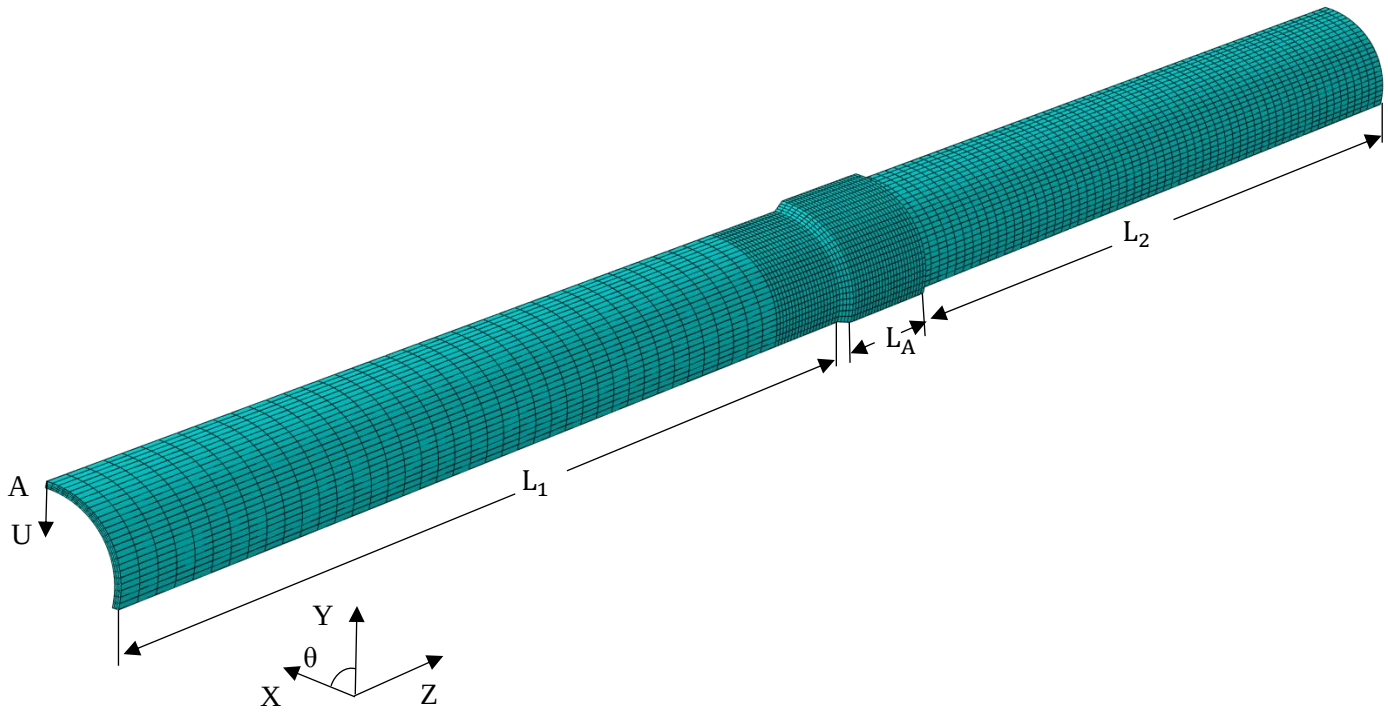

Fig. 4.2 The three-dimensional finite element model which consists of an integral arrestor of length L_A that connects an upstream pipe segment of length L_1 and a downstream pipe segment of length L_2.

The analysis is developed through four steps, and in the same manner as described in section 3.2. The first three general static steps exist for the assignment of initial imperfection in the model and in the last step the uniform external pressure is applied on the model. The response of the system during application of external pressure, is analyzed using Riks' continuation algorithm, which is implemented in ABAQUS software.

4.3 Numerical Results

In this section, the results from the numerical simulation of the finite element model of **Fig. 4.2** (D/t =30) will be presented by means of the deformed configurations and the corresponding pressure-change in volume responses. **Fig. 4.3**a depicts the variation of pressure with the numerically integrated volume reduction during the initiation and propagation of buckle, and its final arrest by an integral buckle arrestor. The numbers in circles on the response of **Fig. 4.3**a correspond to the deformed configurations of **Fig. 4.4**. Collapse occurs at stage (1) in the upstream pipe section (**Fig. 4.2**) where the initial imperfection exists and thus, a first peak in pressure is observed in the response.

The pressure-change in volume response give a collapse pressure of 17.11 MPa. Soon after the occurrence of collapse, the pressure carrying capacity of the pipe drops as it is presented by the (1)-(2)-(3) sequence. At stage (3) the pressure reaches a minimum pressure due to the first contact between the inner pipe walls. The local contact immediately stiffens the pipe and thus an increasement in pressure is observed until a constant pressure value is reached. The upstream pipe length has an appropriate magnitude so that the buckle can propagate unaffected until the arrestor is engaged. Thus, the formation of pressure plateau is observed in the response and the deformed configuration (4). The buckle propagates «freely» under a minimum propagation pressure of 2.86 MPa, until the stiffening effects of the arrestor are introduced in its path. The second increasement in pressure after the constant pressure plateau, correspond to the local stiffening of the structure due to the presence of the arrestor. Therefore, the buckle is «arrested» as it can be seen from the deformed configuration (5). The increasement in pressure continues until a maximum pressure value is reached, as shown at stage (6) of the response. That second pick of pressure-change in area response, corresponds to the crossover pressure of the arrestor. Therefore, the crossover pressure is 14.05 MPa for the finite element model of **Fig. 4.2** (D/t =30) that was discretized with quadratic elements C3D20. After stage (6) the pressure drops, and the deformed configuration of the downstream pipe section (7) seems to follow an ovalization mode, which is perpendicular to that observed in the upstream pipe section (**Fig. 4.4**). The rotation of the ovalization mode by 90° is referred to as the «flipping mode of crossover» and is strongly associated with the geometric characteristics of the arrestor (Chapter 1). The normalized pressure-change in integrated volume response is presented in **Fig. 4.3**b. In that figure the pressure is normalized by the collapse pressure of the upstream pipe and the incremental change in volume is normalized by the initial internal volume of the model V_o. The initial enclosed volume of the model is expressed in terms of internal radius R_{in} as $V_o = \left(\pi {R_{in}}^2 / 4\right)$.

The experimental and numerical results of literature [27], [30]-[32], [21] have shown that thinner arrestors «flatten» after the crossover stage («flattening» mode of crossover), whereas thicker arrestors exhibit the flipping mode of crossover as presented here by the numerical results. The flipping mode of crossover is associated with the efficiency of the device to arrest the propagating buckle. Since an increase in thickness of the pipe wall can affect the propagation of collapse (Section 4.1), it follows that a thicker arrestor is more difficult to be ovalized with respect to a thinner arrestor. Therefore, thicker arrestors result in high crossover pressures, and they are associated with reverse ovalization phenomena of the downstream pipe section.

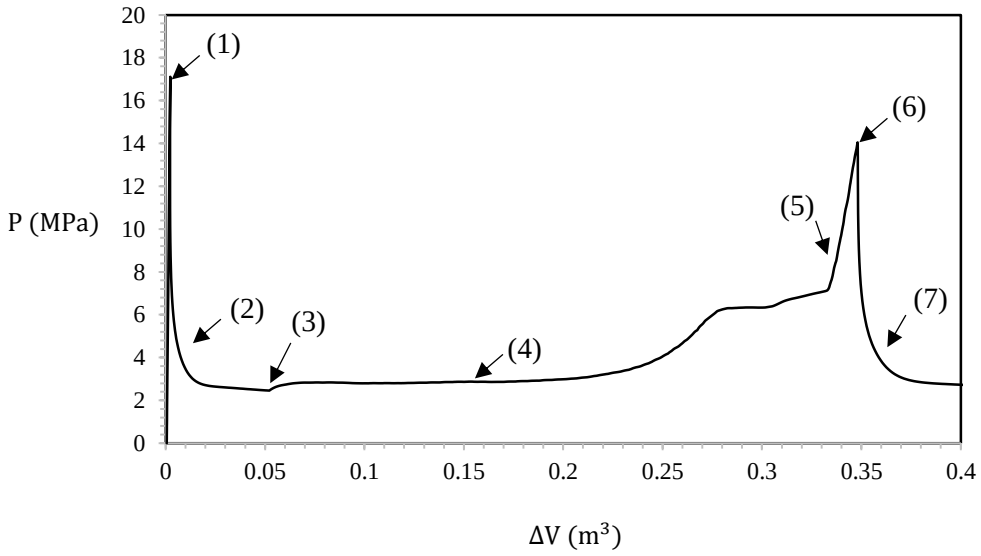

(a)

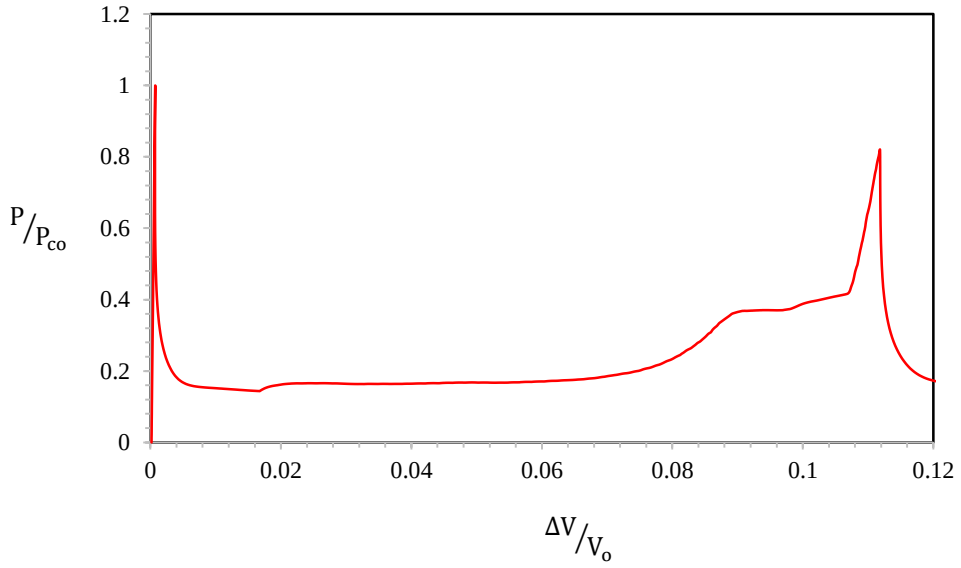

(b)

Fig. 4.3 Pressure-change in volume responses for the finite element model analysis that consists of quadratic elements C3D20. In the second figure (b) the pressure is normalized by the collapse pressure of the upstream pipe section and the volume change is normalized by the internal volume of the model at undeformed conditions.

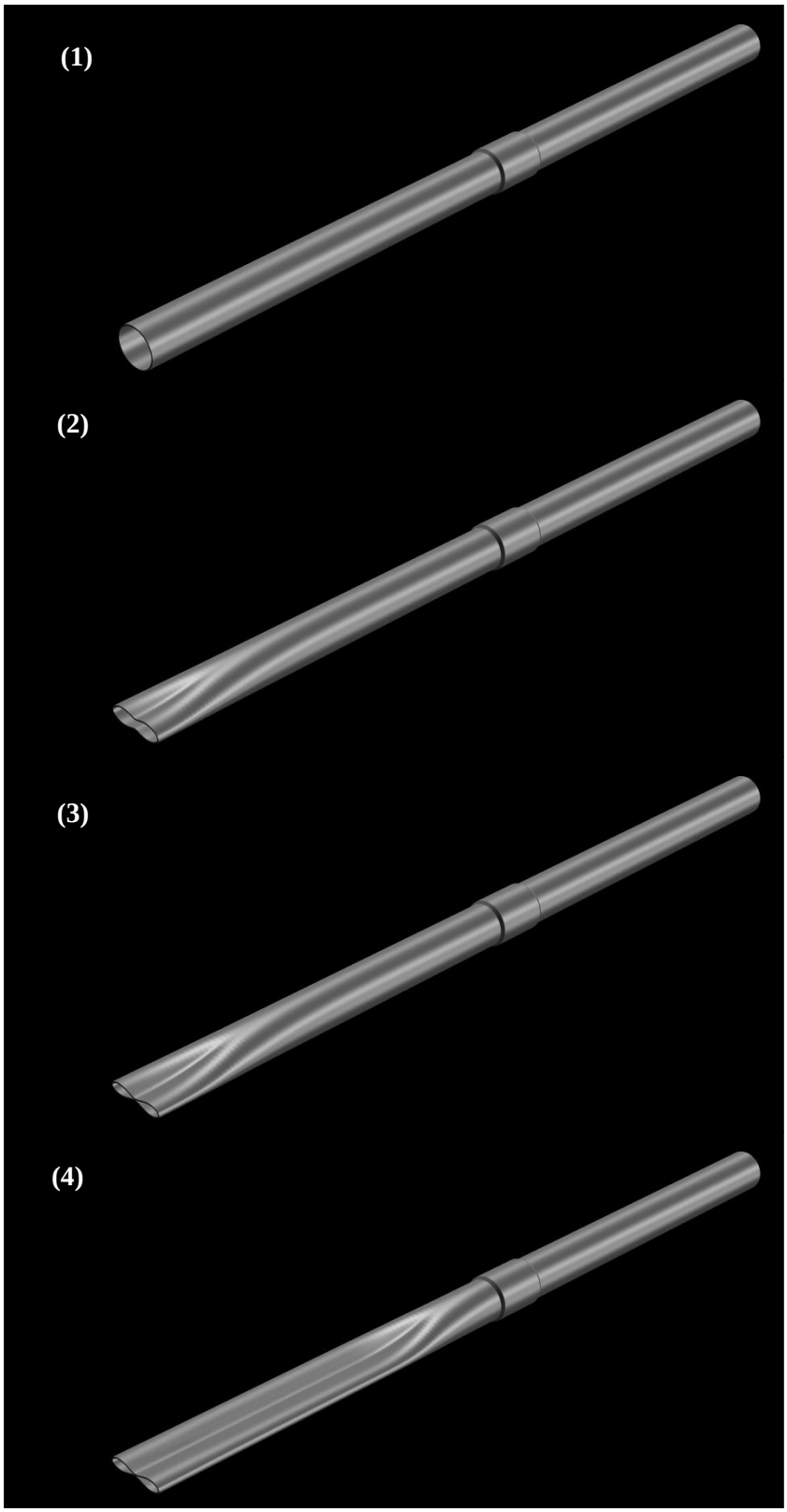

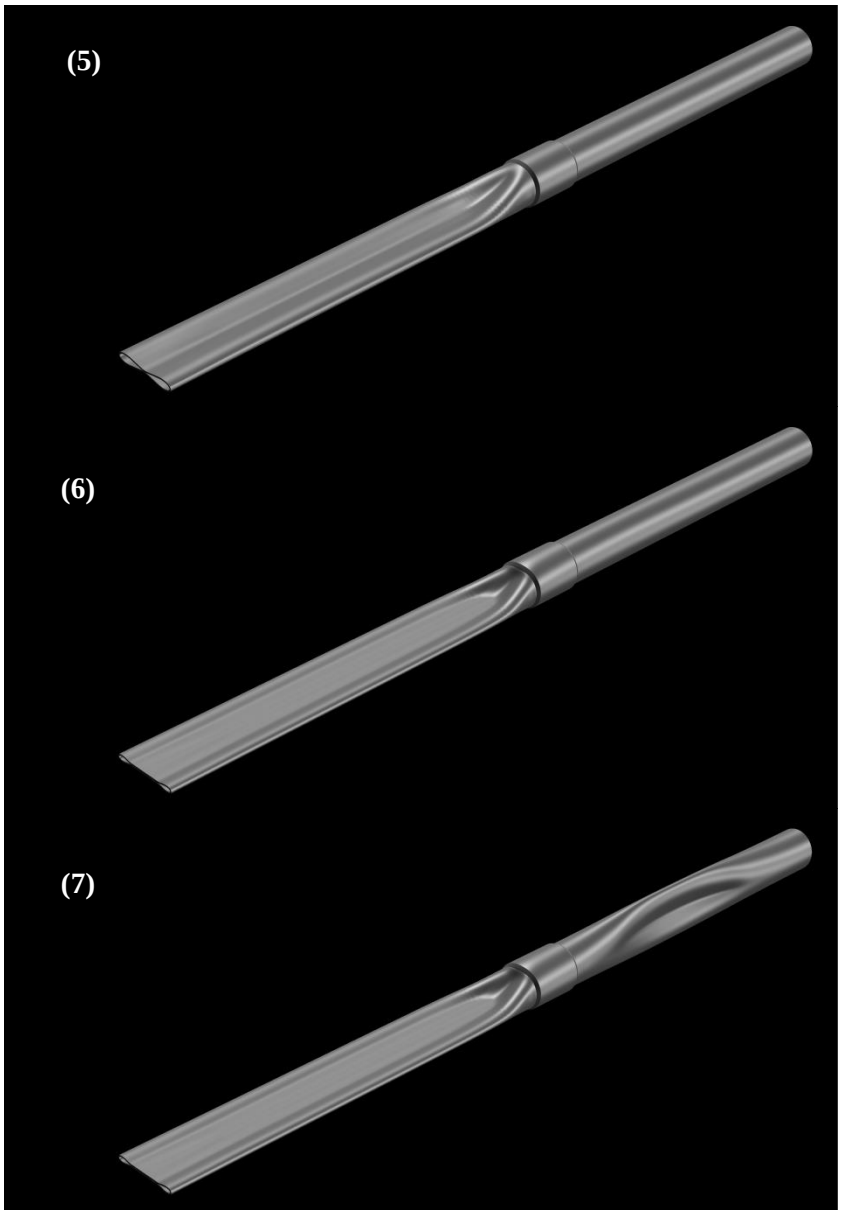

Fig. 4.4 Sequence of deformed configurations from the stage of collapse (1) to the stage of the flipping crossover mode (7). The numbered stages correspond to the numbers in bullets of the pressure-change in volume response for the finite element model that is discretized with quadratic elements C3D20.

4.4 Parameter study of the crossover pressure estimation

The parametric dependance of the crossover pressure estimation on the finite element type of mesh discretization will be examined in this section. Following the numerical modeling procedure of section 4.2, the finite element model (**Fig. 4.2**) was discretized with 8-node linear brick elements of reduced (C3D8R) and full integration (C3D8). These changes are made by keeping the same magnitude of initial imperfection at the origin as well as model geometry and mesh density. Therefore, two different analyses are conducted in ABAQUS standard. **Fig. 4.5** and **Fig. 4.6** show the variation of pressure with the numerically integrated volume reduction of the finite element model, which was discretized with C3D8R and C3D8 finite elements respectively. By changing the finite element type, the arrestor continues to exhibit the flipping mode of crossover and the deformed configurations of the model are of the same type as those presented in **Fig. 4.4**. Therefore, the deformed configurations for the finite element models of C3D8R and C3D8 are not presented here. The pressure-change in volume response of C3D8R finite element discretization (**Fig. 4.5**) result in a crossover pressure of 12.25 MPa (12.81% reduction compared to the crossover pressure obtained with C3D20 finite element discretization). Changing the finite element type to C3D8 (**Fig. 4.6**), the analysis results in a crossover pressure of 16.91 MPa, a value that is 20.36 % higher with respect to that calculated by using C3D20 finite elements. Clearly, the finite element type affects the value of the crossover pressure. The highest crossover pressure value is obtained by using C3D8 finite elements, whereas the lowest is obtained by using C3D8R finite elements. The results show that discrepancies exist not only for analyses of different finite element type but also for analyses of the same finite element type and different integration scheme.

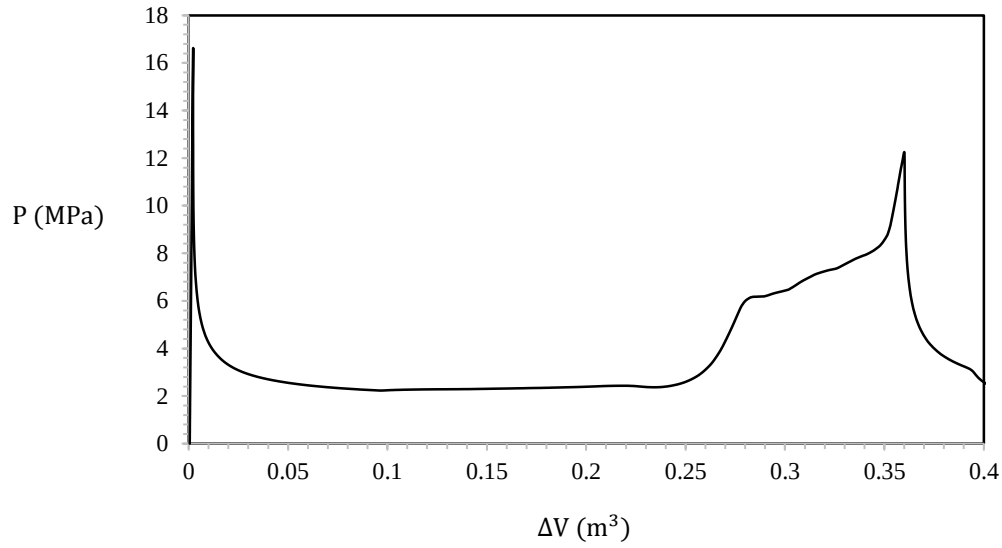

Fig. 4.5 Pressure-change in volume response for the finite element model analysis that consists of linear elements C3D8R.

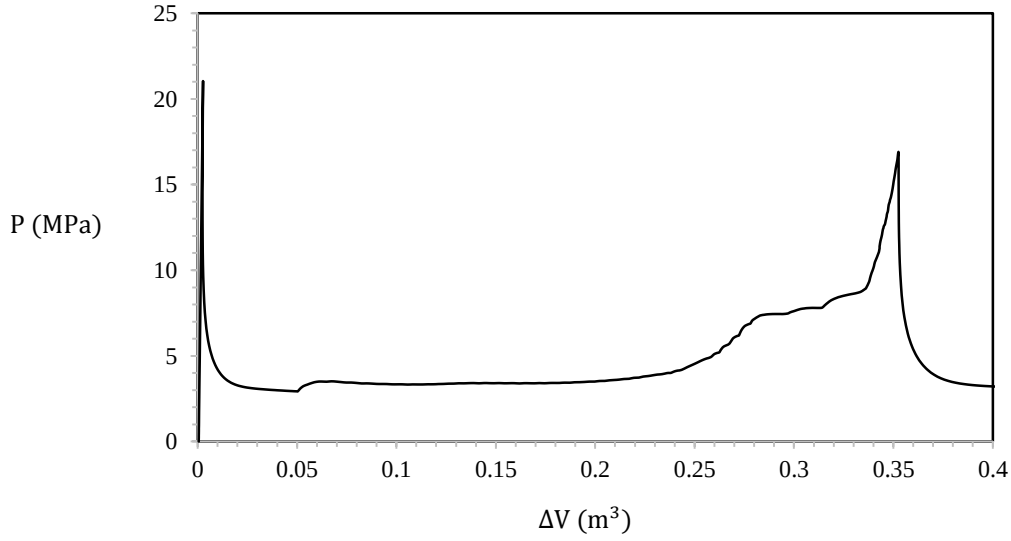

Fig. 4.6 Pressure-change in volume response for the finite element model analysis that consists of linear elements C3D8.

Chapter 5 - Conclusions

The present thesis is concerned with the subjects of collapse and buckle propagation in offshore pipelines. These matters have been studied numerically using the general-purpose finite element program ABAQUS/ standard. The numerical study focuses on the development of two-dimensional and three-dimensional models that help clarify the mechanical behavior of pipelines upon application of external pressure. The terms of elastic and plastic buckling are defined in chapter 1 by a short introduction to ring buckling theory. Therefore, the formulas of critical elastic pressure and collapse pressure are defined for perfect rings. Furthermore, the pre-buckling and post-buckling behavior of elastic and inelastic rings are presented through analytical equations.

A detailed numerical study of the performance of rings upon application of external pressure is presented in chapter 2. Two-dimensional ring models of different diameter-to-thickness ratios (D/t's) are created with imperfections in the form of ovality and wall thickness variation. The collapse responses of initially ovalized models without wall thickness variation shows that initial ovality has a detrimental effect on the collapse capacity of rings. Furthermore, the effects of thickness eccentricity on the collapse pressure are presented through parameter analyses. Meanwhile, the numerical results show that initial imperfections not only affect the collapse capacity of rings but also the corresponding collapse mode. Also, the influence of ring geometries on the collapse pressure has been studied through parametric studies and it has been concluded that the detrimental effects of initial ovality and thickness eccentricity are weaker for higher diameter-to-thickness ratios. Also, the factor of material anisotropy, which exists due to fabrication process of pipes, is studied by the numerical analysis of three-dimensional ring models of various D/t's. The results show that the anisotropic effects on the collapse performance of pipe are weaker for higher D/t's, whereas they are stronger as the D/t is getting lower. In addition, the remaining residual stress fields in the finished pipe product are studied in a three-dimensional ring model of specific D/t geometry. The numerical results clearly show the reduction of the collapse pressure as the residual stress fields are getting stronger.

The effects of initial ovality on the collapse pressure, has also been studied for thin-walled rings of elastic material. Firstly, elastic two dimensional rings of a given geometry and variable imperfection amplitudes are created, and the pre-buckling and post-buckling responses are obtained from the finite element analyses. It is concluded that the higher the imperfection value the lower the collapse pressure. Moreover, a ring of specific imperfection amplitude is selected to study the influence of finite element type on the elastic post-buckling part of pressure-ovality responses. The changes in the finite element type are made by keeping constant the mesh density. The post-buckling responses obtained from the different finite element types are compared with the theoretical post-

buckling curve. The results show that major differences between the numerical and analytical results exist in the post-buckling region upon application of CPE4 finite elements. Furthermore, three-dimensional ring models are created to study the mechanical behavior of elastic rings upon different finite element type discretization. Letting the geometric cross-sectional parameters and initial imperfection amplitude be the same as those used in the two-dimension ring analysis, finite element models of various element types and constant mesh density are created and analyzed. The obtained elastic post-buckling part of pressure-ovality response of different finite element types, is compared with the theoretical post-buckling curve. Outstanding differences observed between the numerical and theoretical curves upon C3D8 finite element discretization. The last section of chapter 2 presents two analytical methods for the calculation of propagation pressure in two dimensions.

A detailed analysis of propagation pressure is presented in chapter 3, by the development of three-dimensional finite elements models. The variation of pressure with the integrated reduction in pipe model volume upon deformation, is created from the numerical results, and is illustrated by pressure-change in volume responses. The propagation pressure is estimated by the responses for two D/t pipe models. The numerical estimations of propagation pressure are compared with those calculated from analytical methods of chapter 2, as well as with the results from accurate analytical expressions from publications and standards. It is found that the two-dimensional results underestimate the propagation pressure. Furthermore, the influences of finite element type discretization and pipe length on the propagation pressure estimations, are studied through parametric analyses for a given pipe model geometry. The results show that the propagation pressure varies significantly with the element type. More specifically, the difference between the numerical estimations and the results from the proposed formulas of API RP 1111 standard [2] and Kyriakides & Babcock [29], is minimized for C3D20 finite element discretization and maximized for C3D8 finite element discretization. However, if a comparison is made with the calculated propagation pressure from the proposed formula of DNV GL-ST-F101 standard [3], the differences between the analytical and numerical results are minimized again for SC8R finite element discretization, but they are maximized for C3D8R finite element discretization. Furthermore, a three-dimensional model of short length is created to study the influence of pipe geometry on the propagation pressure conditions. The results clearly show that the pipe length is so short that the buckle is not able to propagate under steady state conditions.

A device to limit the extent of damage produced by a propagating buckle is presented in chapter 4, by the creation of a three-dimensional finite element model of a buckle arrestor which connects two pipe sections of a line. The integral arrestor device, of a given set of geometric parameters is considered for the finite element analysis. This chapter is mainly focusing on the numerical calculation of the crossover pressure. This is achieved by creating the pressure-change in the

integrated volume response. As it was mentioned in chapter 4, the magnitude of crossover pressure is strongly related with the ability of the device to limit or «arrest» the propagation of an instability (e.g. propagating buckle). Therefore, the influence of finite element type of mesh discretization on the crossover pressure is examined by parametric studies. Under the same finite element model geometry and mesh density, numerical analyses of a different finite element type of reduced and full integration are conducted. The comparison of the results with those obtained by the primary finite element type, show that not only the finite element type but also the scheme of integration influence the accuracy of the numerical results.

References

[1] Kyriakides, S., & Corona, E. (2007). Mechanics of Offshore Pipelines: Vol. 1 Buckling and Collapse. Oxford: Elsevier. https://doi.org/10.1016/b978-0-08-046732-0.x5000-4 .

[2] API Recommended Practice 1111 (1999), "Design, Construction, Operation and Maintenance of Offshore Hydrocarbon Pipelines (Limit State Design)", Washington, DC, USA.

[3] DNVGL-ST-F101 STANDARD (2017) "Submarine Pipeline Systems", DNVGL, Oslo, Norway.

[4] Καραμάνος, Σ.Α. (2003). Σημειώσεις Μαθήματος Μη-Γραμμική Ανάλυση Κατασκευών Ευστάθεια.

[5] Brush, D.O. & Almroth, B.O. (1975). Buckling of Bars, Plates, and Shells, McGraw-Hill, New York.

[6] Timoshenko, S. & Gere, J.M. (1961). Theory of Elastic Stability, 2nd Edition, McGraw-Hill, New York.

[7] Kyriakides, S. & Shaw, P.K. (1982), "Response and stability of elastoplastic circular pipes under combined bending and external pressure", *International Journal of Solids and Structures*, 18(11), 957-973. https://doi.org/10.1016/0020-7683(82)90086-5.

[8] Chatzopoulou, G. (2014). Finite Element Simulation of UOE Pipe Manufacturing Process and its Effect on Offshore Pipeline Mechanical Behavior. Msc. Thesis, University of Thessaly, Greece, http://hdl.handle.net/11615/42600 .

[9] Yeh, M.K. & Kyriakides, S. (1986), "Collapse of deepwater pipelines", *Proceedings of Offshore Technology Conference*, Houston, TX, USA. https://doi.org/10.4043/5215-MS.

[10] Murphey, C.E. & Langner, C.G. (1985), "Ultimate Pipe Strength Under Bending, Collapse and Fatigue", *Proceedings of the 4th International Conference on Offshore Mechanics and Arctic Engineering*, 1, 467–477, Dallas, USA.

[11] Timoshenko, S. (1933), "Working Stresses for Columns and Thin-Walled Structures", *Journal of Appied* Mechanics, 4, 173-177. https://doi.org/10.1115/1.4012225.

[12] Budiansky, B. (1974), "Theory of Buckling and Post-Buckling Behavior of Elastic Structures", *Advances in Applied Mechanics*, 14, 1–65. https://doi.org/10.1016/S0065-2156(08)70030-9.

[13] Palmer, A.C., & Martin, J.H. (1975), "Buckle propagation in submarine pipelines", *Nature*, 254, 46–48. https://doi.org/10.1038/254046a0.

[14] Karamanos, S.A. & Eleftheriadis, C. (2004), "Collapse of pressurized elastoplastic tubular members under lateral loads", *International Journal of Mechanical Sciences*, 46 (1), 35–56. https://doi.org/10.1016/j.ijmecsci.2004.02.015.

[15] Kyriakides, S., & Babcock, C.D. (1981), "Large deflection collapse analysis of an inelastic inextensional ring under external pressure", *International Journal of Solids and Structures*, 17 (10), 981–993. https://doi.org/10.1016/0020-7683(81)90036-6.

[16] Chatzopoulou, G., Karamanos, S.A. and Varelis, G.E. (2016), "Finite Element Analysis of UOE Manufacturing Process and its Effect on Mechanical Behavior of Offshore Pipes", *International Journal Solids and Structures*, 83, 13–27. https://doi.org/10.1016/j.ijsolstr.2015.12.020.

[17] Antoniou, K., Chatzopoulou, G., Karamanos, S.A., Tazedakis, A., Palagas, C. and Dourdounis, E. (2019), "Numerical Simulation of JCO-E Pipe Manufacturing Process and Its Effect on the External Pressure Capacity of the Pipe", *ASME Journal of Offshore Mechanics and Arctic Engineering*, 141 (1). https://doi.org/10.1115/1.4040801.

[18] Zhang, X. & Pan, G. (2020), "Collapse of thick-walled subsea pipelines with imperfections subjected to external pressure", *Ocean Engineering*, 213. https://doi.org/10.1016/j.oceaneng.2020.107705.

[19] Herynk, M.D., Kyriakides, S., Onoufriou, A. and Yun, H.D. (2007), "Effects of the UOE/UOC manufacturing process on pipe collapse pressure", *International Journal of Mechanical Sciences*, 49, 533–553. https://doi.org/10.1016/j.ijmecsci.2006.10.001.

[20] Ντοάς, Δ. (2021), **"**Αριθμητική προσομοίωση της αντοχής χαλύβδινων υποθαλάσσιων αγωγών σε εξωτερική πίεση με πεπερασμένα στοιχεία", Διπλωματική Εργασία, Πανεπιστήμιο Θεσσαλίας. http://hdl.handle.net/11615/55134.

[21] Τσάλας, Ι.Κ. (2021), "Προσομοίωση Πεπερασμένων Στοιχείων της Διαδιδώμενης Ύβωσης και της Αναστολής της σε Υποθαλάσσιους Αγωγούς", Διπλωματική Εργασία, Πανεπιστήμιο Θεσσαλίας. http://hdl.handle.net/11615/56717 .

[22] Yeh, M.K., Kyriakides, S. (1986), "On the Collapse of Inelastic Thick-Walled Tubes Under External Pressure", *Journal of Energy Resources Technology*, 108(1), 35-47. https://doi.org/10.1115/1.3231239.

[23] Hill, R. (1948), "A theory of the yielding and plastic flow of anisotropic metals", *Proceedings of the Royal Society A*, 193, 281-297. https://doi.org/10.1098/rspa.1948.0045 .

[24] Tong He, Menglan Duan, Chen An (2014), "Prediction of the collapse pressure for thick-walled pipes under external pressure", *Applied Ocean Research*, 47, 199-203. https://doi.org/10.1016/j.apor.2014.05.006 .

[25] Tokimasa, K. & Tanaka, K. (1986), "FEM Analysis of the Collapse Strength of a Tube", *ASME Journal of Pressure Vessel Technology*, 108(2), 158–164. https://doi.org/10.1115/1.3264764 .

[26] Chater, E. & Hutchinson, J. W. (1984), "On the Propagation of Bulges and Buckles", *ASME. Journal of Applied Mechanics*, 51(2), 269–277. https://doi.org/10.1115/1.3167611 .

[27] Kyriakides, S., & Lee, L.H. (2020). Mechanics of Offshore Pipelines: Vol. 2 Buckle Propagation and Arrest. Gulf Professional Publishing. https://doi.org/10.1016/C2017-0-03845-4 .

[28] Tassoulas, J.L., Katsounas, A.T., and H-W. Song. (1990), "Finite Element Analysis of Propagating Buckles in Deepwater Pipelines", *Offshore Technology Conference*, Houston, Texas. https://doi.org/10.4043/6413-MS .

[29] Kyriakides, S., & Babcock, C.D. (1981), "Experimental Determination of the Propagation Pressure of Circular Pipes", *ASME Journal of Pressure Vessel Technology*, 103(4), 328–336. https://doi.org/10.1115/1.3263410 .

[30] Park, T.D., Kyriakides, S. (1997), "On the performance of integral buckle arrestors for offshore pipelines", *International Journal of Mechanical Sciences*, 39(6), 643-669. https://doi.org/10.1016/S0020-7403(96)00074-4 .

[31] Lee, L.H., Kyriakides, S., Netto, T.A. (2008), "Integral buckle arrestors for offshore pipelines: Enhanced design criteria", *International Journal of Mechanical Sciences*, 50(6), 1058-1064. https://doi.org/10.1016/j.ijmecsci.2008.02.008 .

[32] Toscano, R.G., Mantovano, L.O., Amenta, P. M., Charreau, R.F., Johnson, D.H, Assanelli, A.P, Dvorkin, E.N. (2008), "Collapse arrestors for deepwater pipelines. Cross-over mechanisms", *Computers & Structures*,86, (7–8), 728-743. https://doi.org/10.1016/j.compstruc.2007.07.009 .